High Speed Turboprop Aeroacoustic Study (Counterrotation)

Volume I – Model Development

C. E. Whitfield, R. Mani, and P.R. Gliebe
GE Aircraft Engines
Advanced Technology Operations
Cincinnati, Ohio 45215

July 1990

NASA

National Aeronautics and
Space Administration

High Speed Turboprop Aeroacoustic Study (Counterrotation)

Volume I - Model Development

Acknowledgments

Summary

The isolated counterrotating high speed turboprop noise prediction program developed and funded by GE Aircraft Engines has been compared with model data taken in the GE Aircraft Engines Cell 41 anechoic facility, the Boeing Transonic Wind Tunnel, and in NASA Lewis Research Center's 8x6 and 9x15 foot wind tunnels. The predictions show good agreement with measured data under both low and high speed simulated flight conditions.

The installation effects model developed for single–rotation, high speed turboprops has been extended to include counterrotation and the additional effect of a mounting pylon upstream of the forward rotor.

A nontraditional mechanism concerning the acoustic radiation from a propeller at angle of attack has been investigated. Predictions made using this approach show results that are in much closer agreement with measurements over a range of operating conditions than are obtained via traditional fluctuating force methods.

The isolated rotors and installation effects models have been combined into a single prediction program, results of which have been compared with data taken during the flight test of the B727/UDF®* engine demonstrator aircraft.

The satisfactory comparisons between prediction and measured data for the demonstrator airplane, together with the identification of a nontraditional radiation mechanism for propellers at angle of attack, constitute the major achievements of this Contract.

*UDF® is a registered trademark of the General Electric Company, U.S.A.

PRECEDING PAGE BLANK NOT FILMED

Table of Contents

List of Illustrations

List of Illustrations

List of Illustrations

List of Illustrations

List of Illustrations

List of Illustrations

List of Illustrations

List of Illustrations

1.0 Introduction

1.1 Background

Recent studies have shown that the high speed turboprop offers an attractive alternative to turbofan propulsion for certain future commercial aircraft applications because of its substantially higher propulsive efficiency potential. However, one of the major obstacles to the use of high speed turboprops is the high near–field noise level generated by the propeller, which may cause a potentially serious cabin noise problem. In response to this potential problem, there has been substantial activity in both theoretical and experimental investigations of the noise characteristics of high speed propellers by NASA and private industry.

The currently envisioned high speed turboprop systems call for cruise flight speed Mach numbers of 0.7 to 0.8 and propeller tip speed Mach numbers of 0.7 to 0.9, which results in propeller blade operation in the transonic and supersonic regimes. Recent theoretical models of propeller noise have been produced to account for forward flight effects, source noncompactness, and supersonic motion of the blade fixed sources relative to the observer position. These effects are all present to some degree for propellers operating at transonic and supersonic relative Mach numbers. The concept of the propfan, a low aspect ratio, high blade number propeller with swept blades, has features which promise significantly lower noise than conventional propellers. These features include very thin blade sections with large sweep angles near the tip to produce subsonic relative Mach number components normal to the leading edge of the blade, thus reducing losses and flow field discontinuities associated with the formation of shock waves.

Further improvements in propulsive efficiency are achievable if the energy lost in the swirling flow at the exit of a high speed turboprop can be recovered. The counterrotation propeller, in which a second rotor, whose direction of rotation is opposite to that of the original, operates in the slip–stream of the first rotor to restore the outflow to the axial direction is one means by which this may be accomplished.

While promising great potential performance benefits, the counterrotation high speed turboprop concept does present several potential noise problems, both in the low (typical takeoff and approach) and high (typical cruise) flight speed regimes. At high flight speed, the noise sources of concern are those of the single–rotation propfan, namely the steady loading and thickness noise of each rotor, together with such installation effects as are applicable under these conditions. Under low flight speed conditions, however, the response of the aft rotor to the wakes and tip vortices shed from the blades of the forward rotor cannot be ignored, and likewise, the effects of the installation environment on the acoustic output of the two rotors may well be significant.

Over the past several years, much work has been undertaken, both by private industry and under NASA sponsorship, to obtain a better understanding of both the aerodynamics and the aeroacoustics of counterrotating high speed turboprops over the entire flight envelope. This effort culminated in the successful flight of the UDF® engine on the Boeing 727 demonstrator airplane.

1.2 Current Work

The work described in this report extends the single–rotation, high speed turboprop aeroacoustic study of Reference 1 to counterrotation. First, results obtained using the isolated counterrotating high speed turboprop noise prediction program developed under internal funding at GE Aircraft

Engines (GEAE) are compared with model data obtained for four different blade designs in the GEAE Cell 41 low speed free–jet acoustic facility, the Boeing Transonic Wind Tunnel, and the NASA Lewis Research Center 8x6 foot high speed and 9x15 foot low speed wind tunnels. The Cell 41 data were obtained under NASA Contract NAS3–24080 (Reference 2). The NASA data were recorded in the NASA Lewis Research Center wind tunnels by NASA personnel (with GEAE participation) as a part of the said contract; and selected data provided to GEAE by NASA. Second, the single–rotation installation effects model developed under this Contract (Reference 1) has been extended for counterrotation application. This effort has entailed the major portion of the work accomplished under the extension of the original single–rotation, high speed turboprop aeroacoustic study Contract to counterrotation, and includes the development of a counterrotation aerodynamic model (based on the single rotation model of Reference 1) to compute axial and tangential force coefficients given lift/drag relations for each radial section as functions of angle of attack. The installation effects whose flowfields are computed for input to the acoustic model are those of Reference 1, namely angle of attack, the presence of a fuselage, and the presence of a wing lifting line. In addition, the effect of a mounting pylon upstream of the forward rotor has been included. With the exception of the angle–of–attack case, which has been reported separately in Reference 3, no changes were made to the acoustic model developed originally for single rotation high speed turboprops. Each rotor is considered independently, and only BPF tones and harmonics thereof for each rotor are considered.

The two computer programs resulting from the work described above (namely the GEAE internally funded Isolated Counterrotating Propeller Noise Prediction code, and the Installation Effects code developed in the current program) have been integrated into an installed counter–rotating, high speed turboprop noise prediction system. Results from this combined program have been compared with data taken during the flight test of the B–727/UDF® engine demonstrator aircraft (Reference 4).

1.3 Objective

The objective of the current study has been to develop a verified computer model of the noise generated by a counterrotating high speed turboprop, taking into account:

- Steady loading and thickness noise of Rotor 1

- Steady loading and thickness noise of Rotor 2

- Unsteady loading noise of Rotor 2 resulting from interaction with the wakes and vortices shed from Rotor 1

- Unsteady loading noise of Rotor 1 resulting from interaction with nonuniform flow caused by the installation environment

- Unsteady loading noise of Rotor 2 resulting from interaction with nonuniform flow caused by the installation environment.

2

2.0 Analysis and Results

2.1 Isolated Counterrotating High Speed Turboprop Noise

2.1.1 Introduction

The isolated counterrotating, high speed turboprop noise model delivered under this contract was developed under internal GEAE funding. Consequently, only a brief description is presented below.

2.1.2 Model Development

The isolated counterrotating, high speed turboprop noise model computes:

- Steady loading and thickness noise of Rotor 1

- Steady loading and thickness noise of Rotor 2

- Unsteady loading noise of Rotor 2 resulting from interaction with the wakes and vortices shed from Rotor 1

where the formulation employed is similar to that of Hanson (Reference 5).

The steady loading and thickness noise of each rotor is computed by the frequency–domain, noncompact source method described, for single rotation, in Reference 1. Each rotor is treated as an independent source, with the axial distance between the pitch change axes preserved. Calculation of the unsteady loading noise generated by the interaction of the blades of Rotor 2 with the wakes and tip vortices shed from the Rotor 1 blading is accomplished via a chordwise compact acoustic model (in contrast to the acoustic model used for the steady loading and thickness calculation). The unsteady flow field between the rotors is established via the compressor wake model developed under NASA Contract NAS3–23681 (Reference 6) and the tip vortex model developed for UDF® engines as a part of NASA Contract NAS3–24080 (Reference 7). Spanwise phasing effects, resulting from the sweep and lean of the blading and the direction of the mean flow, are preserved in this treatment. The unsteady loading at each spanwise section on the aft blades is obtained via unsteady airfoil theory (with compressibility effects included) following Fourier decomposition of the components of the fluctuating velocity normal to the chord of the aft blade. Only these transverse gusts are included in the calculation.

The methods described above lead to predictions of tone SPLs at frequencies corresponding to:

$$n * \text{BPF1}$$
$$m * \text{BPF2}$$
$$n * \text{BPF1} + m*\text{BPF2}$$

Where BPF1 = Rotor 1 blade passing frequency

BPF2 = Rotor 2 blade passing frequency

and m, n are integers

Typical execution times for computation of 10 steady loading and thickness harmonics of each rotor BPF, together with 150 Rotor1/Rotor2 interaction tones at each of 17 observer angles are of the order of 8 and 15 minutes for "community noise" and "cruise noise" examples respectively using a MicroVax II computer.

2.1.3 Data/Theory Comparisons

The data used in the verification of the isolated counterrotating high speed turboprop noise prediction program delivered under this contract were obtained during scale model testing of several proposed blade designs in four different facilities. Simulated flight Mach numbers attained during these tests range from 0.2 to 0.8, and, for convenience, because the significance of the various noise sources is a function of Mach number, the comparisons which follow have been divided into high speed (representing cruise) and low speed (representing takeoff) conditions. At high speed, nearfield noise as perceived on the fuselage of an airplane is expected to be a prime concern, whereas at low speed it is anticipated that farfield (community) noise represents the major problem.

The test vehicles and scale model blades used for these comparisons were, in the main, designed and manufactured by GE Aircraft Engines under NASA Contract NAS3–24080 (Reference 2).

2.1.3.1 High Speed Comparisons

High simulated flight Mach number testing was conducted in the NASA Lewis Research Center 8x6 foot transonic wind tunnel under Contract NAS3–24080 and also in the Boeing Transonic Wind Tunnel under GE funding. The two facilities employ different philosophies in the acquisition of acoustic data under these conditions. In the NASA tunnel, shown in Figure 1, pressure transducers are flush mounted in a steel plate which is suspended from the ceiling of the (otherwise unmodified) tunnel working section. It is believed (Dittmar, Reference 8) that the location of the plate is such that the effects of reflections from the tunnel walls are avoided, and the only disadvantage entailed with this method is that, due to the presence of the boundary layer on the flat plate, the noise levels measured by the transducers forward of the plane of rotation are lower than would otherwise be the case.

Figure 2 shows the anechoically treated working section of the Boeing Transonic Wing Tunnel. Here the acoustic data are taken by means of traversing microphones, suspended from the ceiling at two different sideline distances. This method of data acquisition also has good and bad points – a wider range of observation angles is available than is the case with the NASA flat plate, but, in order to ensure reasonable data quality, the traverse must move at a slow speed (0.4 in/sec) requiring much tunnel time for each acoustic data point in addition to the major expense entailed in the tunnel modification. The F7A7 blade design combination, shown in plan form in Figure 3, was tested in both facilities at its design condition (tunnel Mach Number = 0.72, 8+8 blades) with blade angles $\beta_{3/4} = 56.9°$ and $54.4°$ for the forward and aft rotors, respectively. In order to compare results from the two facilities, it is necessary to establish a common set of conditions (sideline distance, tunnel static pressure, free field, or flat plate). In Figures 4 through 6, the NASA 8x6 foot wind tunnel conditions have been selected as the reference. The BTWT (Boeing Transonic Wind Tunnel) data have been adjusted as follows:

Free field ⟶ flat plate:	+	6 dB
Sideline distance correction: (2.2 ft ⟶ 1.64 ft)	+	2.5 dB
Static pressure correction: (10.5 psi ⟶ 12.2 psi)	+	1.3 db
Total Adjustment =	+	9.8 dB

4
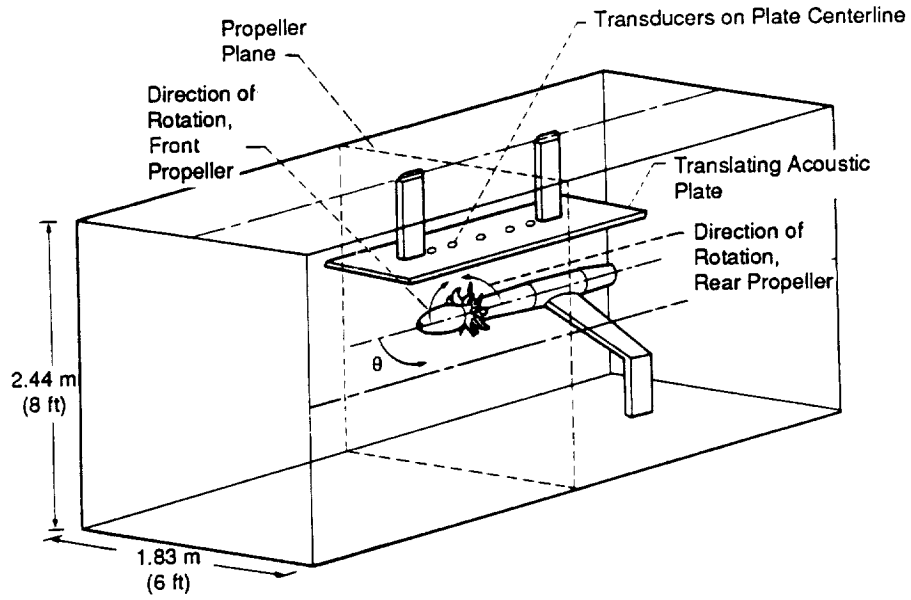
Figure 1. MPS (Model Propulsion Simulator) and Translating Plate in the NASA Lewis Research Center 8x6 foot Transonic Wind Tunnel - (from Reference 9).

Microphone Traverse

Acoustic Treatment

Facing Downstream
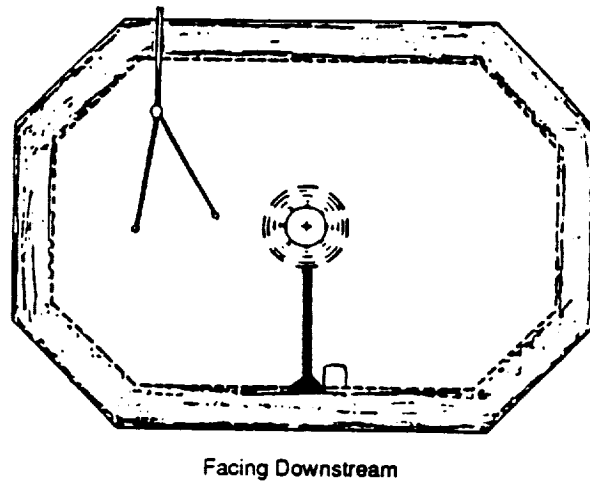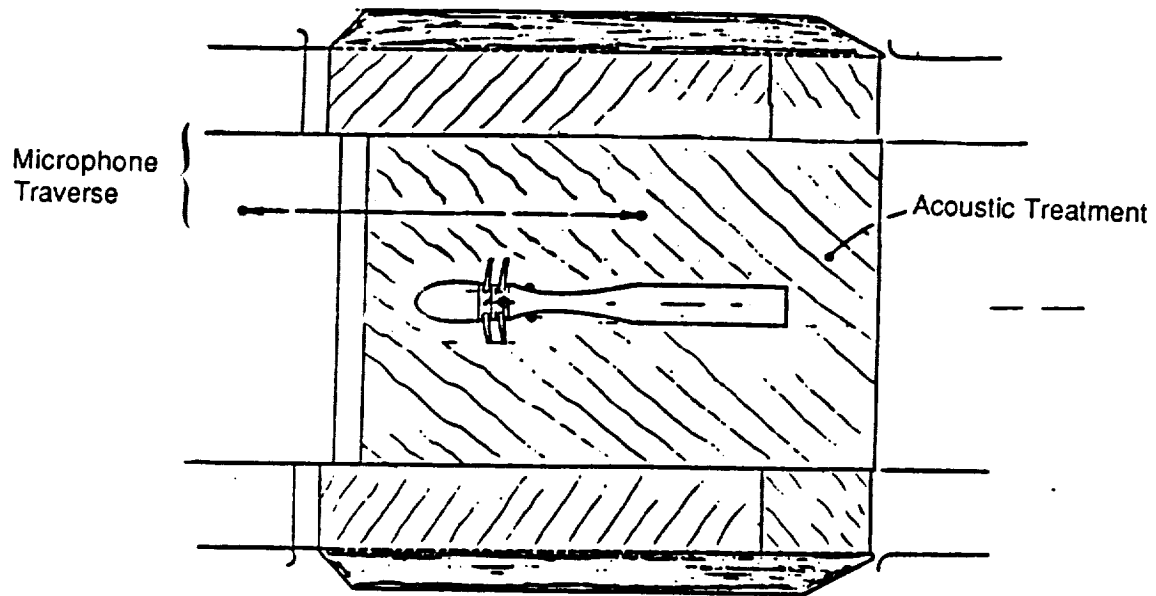
Figure 2. Sketch of MPS (Model Propulsion Simulator) and Traversing Microphones in the Boeing Transonic Wind Tunnel (BTWT).
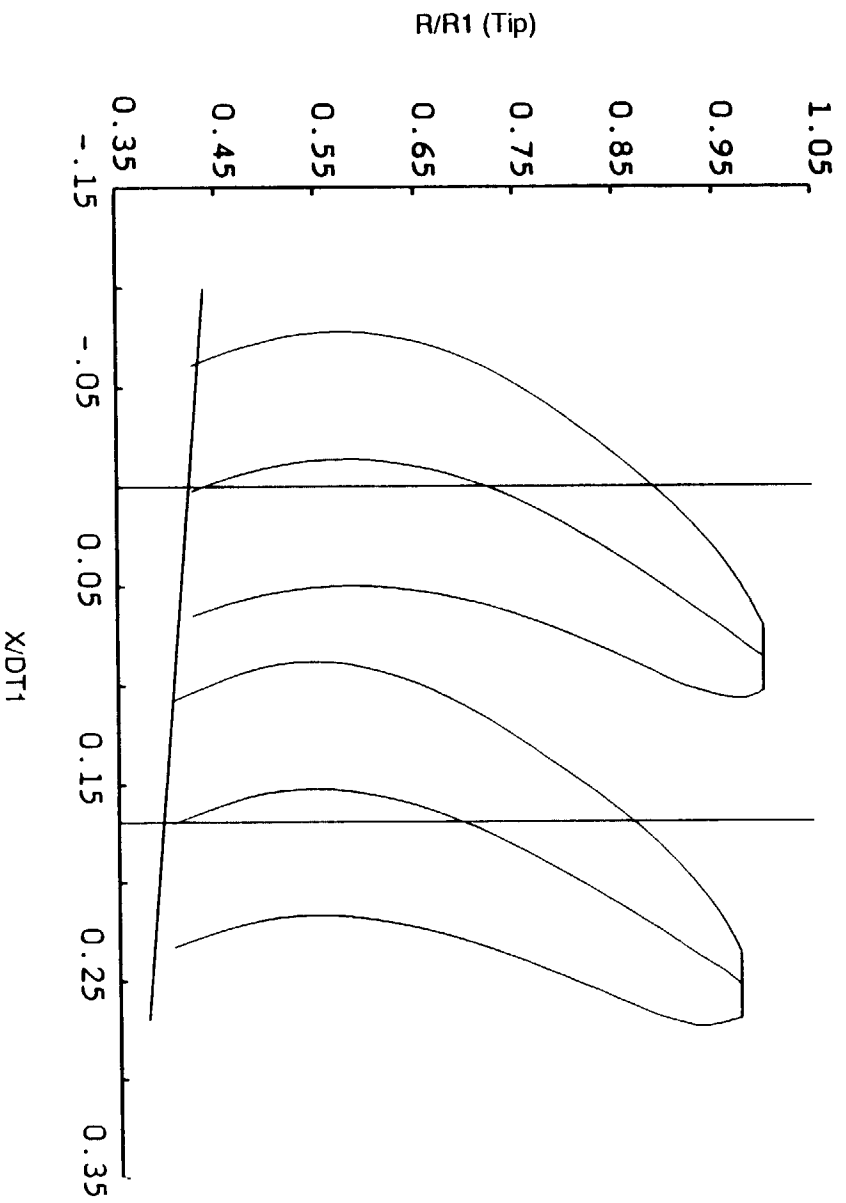
Figure 3. F7A7 Blade Design Planforms.

7
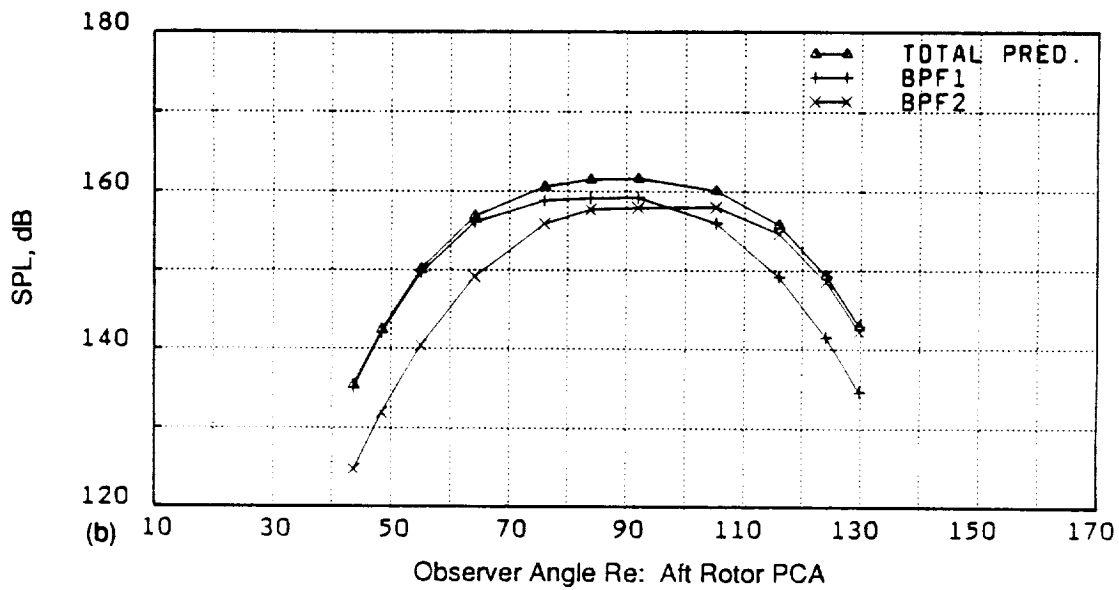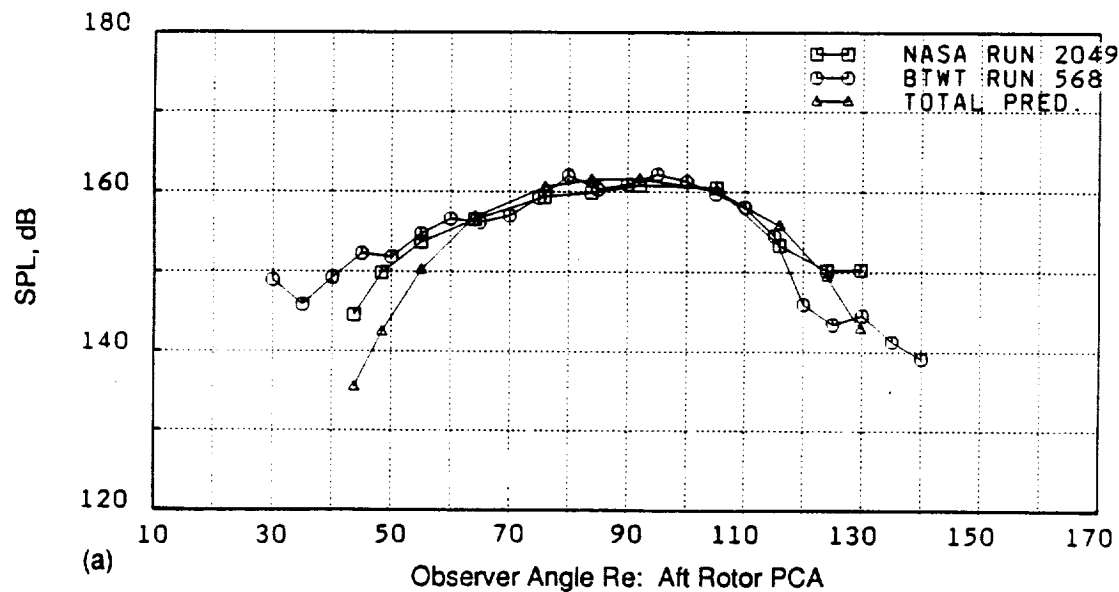
Figure 4. Comparison Between Data Acquired in Two Facilities and Prediction: NASA Acoustic Run 2049, F7A7 Blade Design, Mo = 0.72, 8 + 8 Blades, 100% RPM$_c$ BPF Tone. (a) Data Versus "Total" Predictions; (b) Composition of "Total" Prediction.
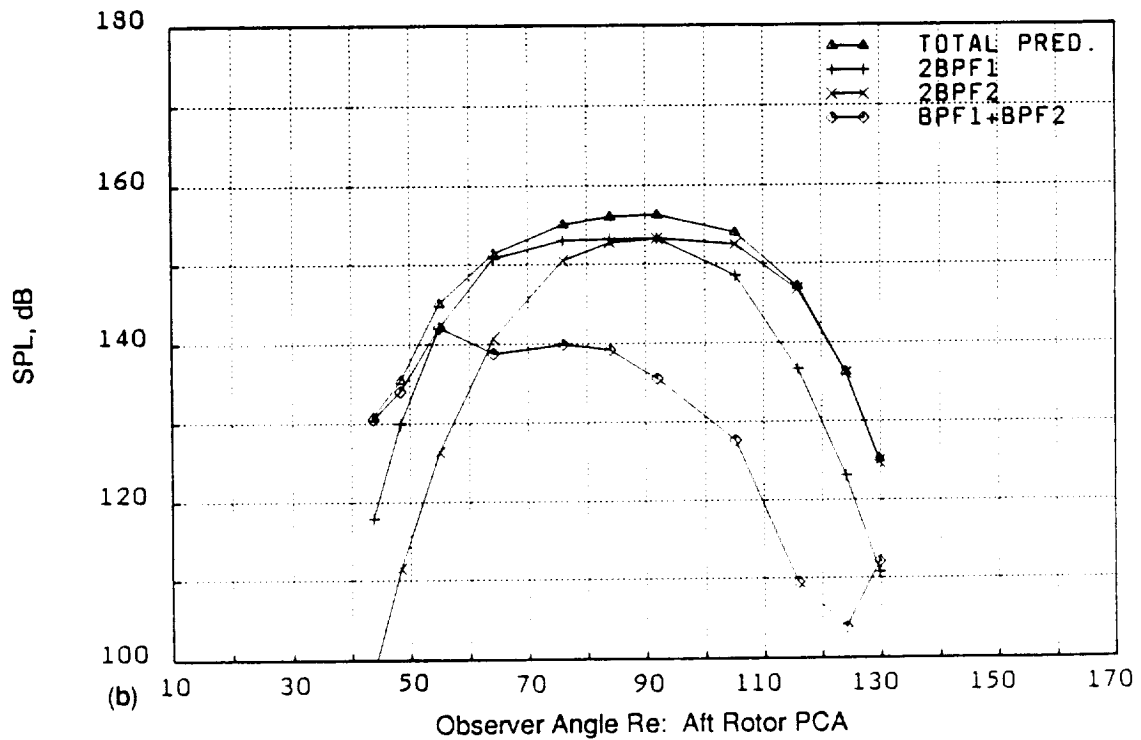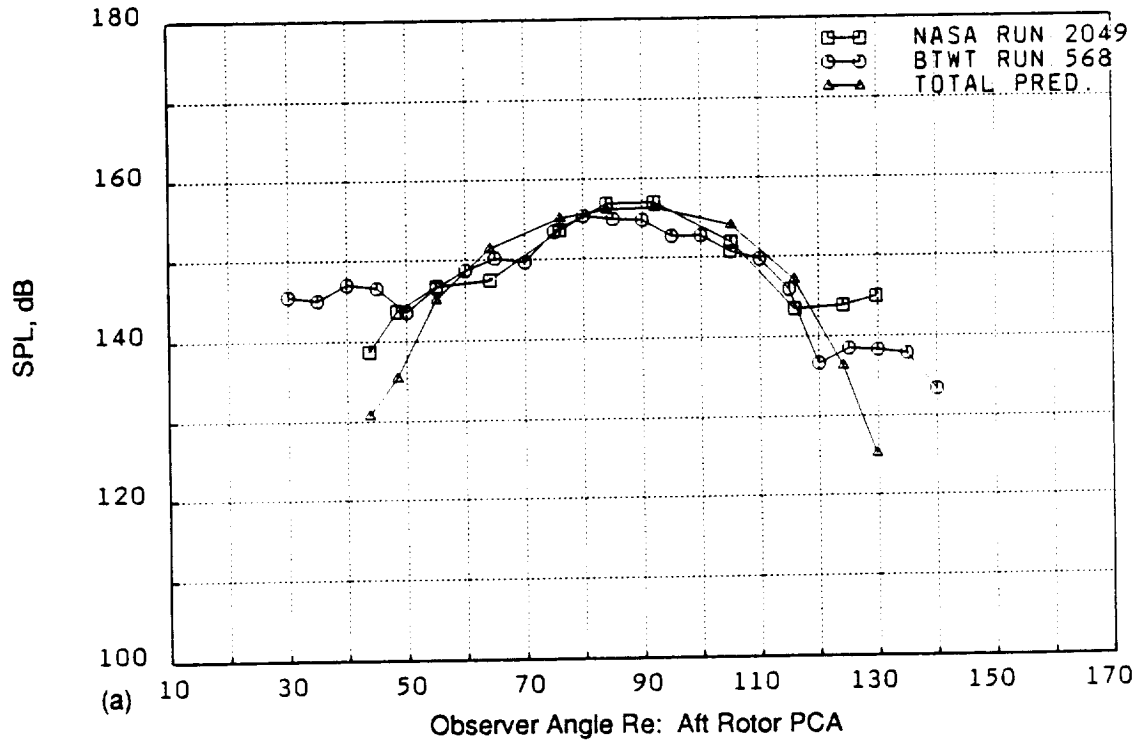
Figure 5. Comparison Between Data Acquired in Two Facilities and Prediction: NASA Acoustic Run 2049, F7A7 Blade Design, Mo = 0.72, 8 + 8 Blades, 100% RPM_c 2*BPF Tone. (a) Data Versus "Total" Predictions; (b) Composition of "Total" Prediction.

9
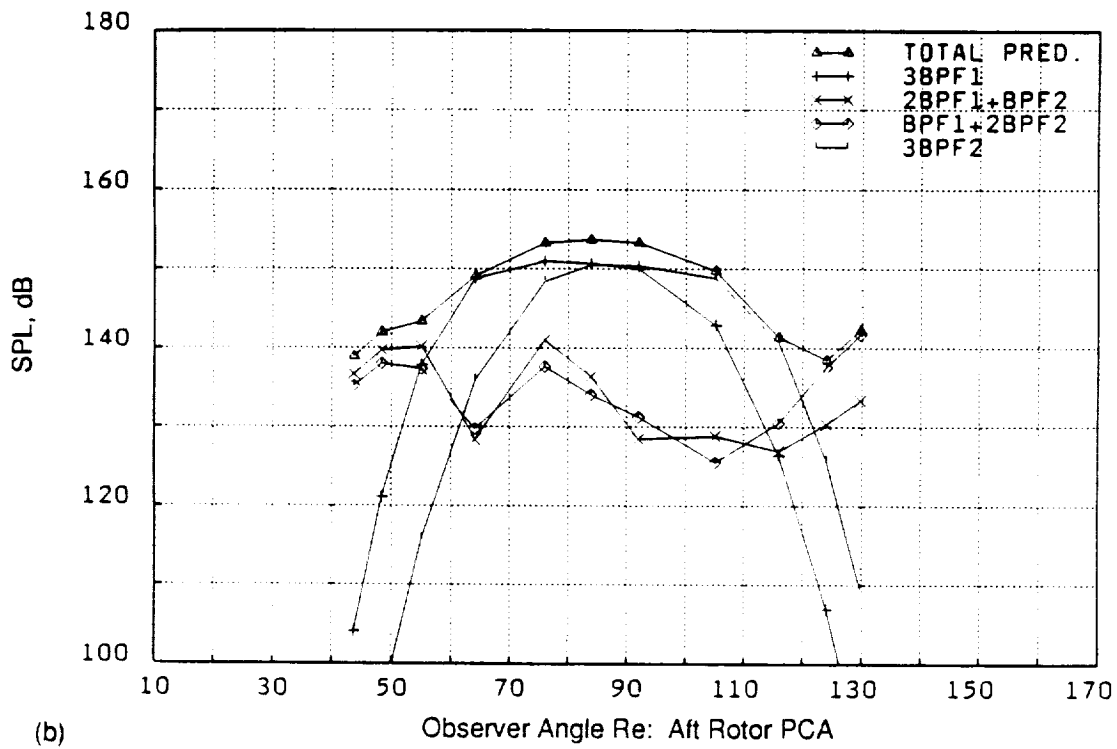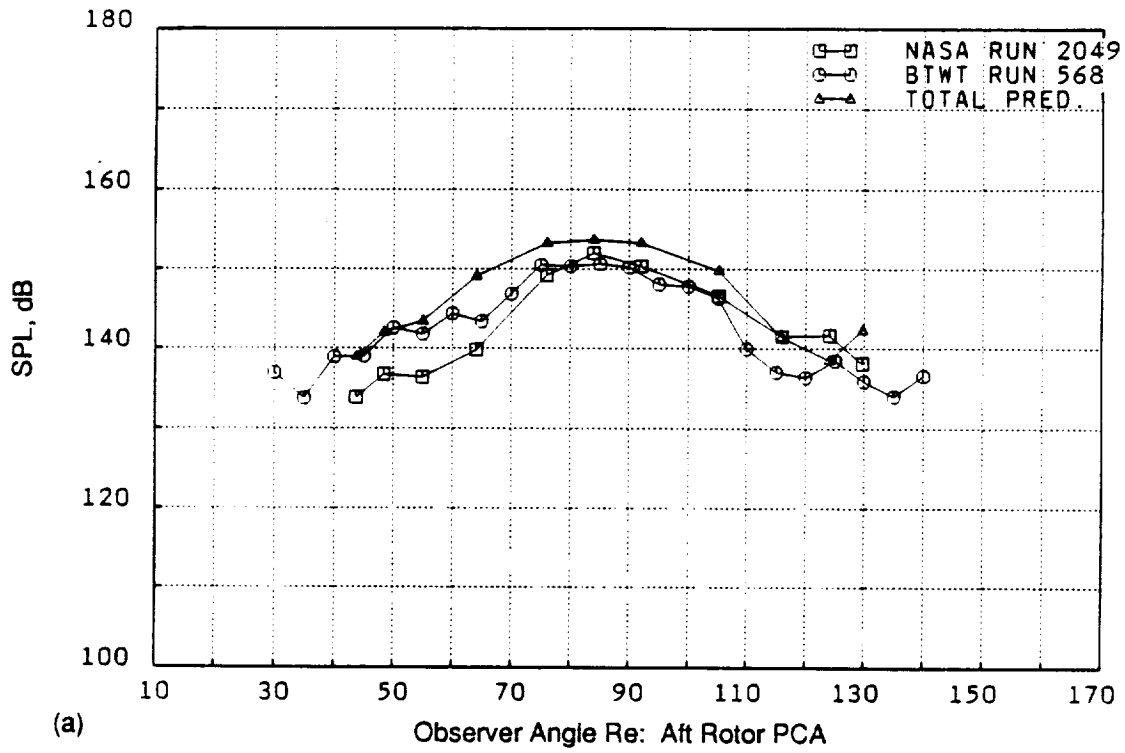
Figure 6. Comparison Between Data Acquired in Two Facilities and Prediction: NASA Acoustic Run 2049, F7A7 Blade Design, Mo = 0.72, 8 + 8 Blades, 100% RPM$_c$ 3*BPF Tone. (a) Data Versus "Total" Predictions; (b) Composition of "Total" Prediction.

(These are the same corrections as those of Dittmar (Reference 8), but applied to the BTWT rather than the NASA data).

Also shown in Figures 4 through 6 are predictions made using the code delivered under this contract. These predictions were made using the NASA test conditions of tunnel static temperature and pressure, together with relevant performance parameters (for example shaft horsepower and rpm for each rotor) measured at the time of the test. Blade geometry and the spanwise loading distribution used (spanwise loading is defined in Reference 1) were those for which the blades were designed. Experience has shown that the chordwise loading distributions generated from 3D (three dimensional) Euler CFD solutions (that were shown in Reference 1) can be replaced by simple analytical expressions, selected according to the flight conditions; consequently, for this high flight Mach number case, a rectangular normalized chordwise loading distribution was used.

The two rotors have the same number of blades, and are running at approximately the same speed (rpm). Consequently, given the bandwidth of the analysis equipment used, the harmonic components generated by the forward and aft blading are inseparable. The theoretical model suffers from no such inhibitions, however, and generates individual tones regardless of whether the frequencies involved are coincidental. Figures 4 through 6 thus show, in addition to the two sets of data, individual tone predictions for all the components perceived at a particular frequency, in addition to the "total" prediction, corresponding to

$$SPL_{Total} = 10 \log_{10} \left(\sum_{Tones} 10^{(SPL_{Tone}/10)} \right)$$

Figures 4 and 5 demonstrate good agreement between the two sets of data, despite the differences in acquisition. Figure 6 appears to show some attenuation of the flat plate data in the forward arc, suggesting refraction of the acoustic signal in the boundary layer on the plate. It would be expected (Reference 1) that such boundary layer refraction effects would become more apparent as the harmonic number increased. The agreement between the two sets of data and the "total" prediction shown in Figures 4 and 5 is very good. Figure 6, for the combined third harmonic of BPF shows a degree of overprediction. Experience has shown that this overprediction is a function of the thickness noise calculation, and it becomes more pronounced with increasing BPF harmonic number.

One concept studied for reducing Rotor 1/Rotor 2 interaction noise in the low flight speed regime is that of the reduced diameter aft rotor. The design intent is to remove the tip of the blade from the influence of the forward rotor tip vortex, while increasing the chord to enable the blade to carry the same load as the equivalent full–diameter blade design. Figure 7 compares the reduced diameter A3 design with the more conventional A1 blade; each of these designs was intended to run behind the F1 forward rotor blading, as shown in this figure. Experimental comparisons between "standard" and "reduced" rear rotor diameter blading have been made by Woodward (Reference 9) under low flight speed conditions, and also by Dittmar (Reference 10) for the high flight Mach numbers under consideration in this section. Dittmar demonstrated that while interaction tones are less significant at the high helical tip Mach numbers encountered in this flight regime, and hence the main motive for use of a reduced diameter rear rotor might appear redundant, the reduction in tip speed resulting from the use of a shorter blade is such as to cause a decrease in the levels of the blade passing frequency harmonics generated by that rotor, especially under off–design conditions.
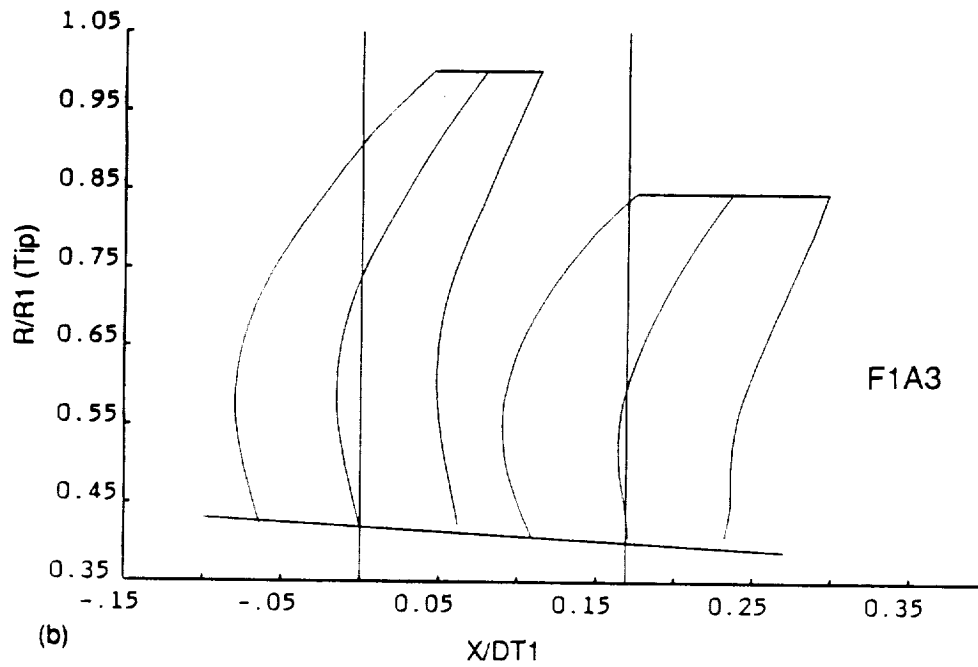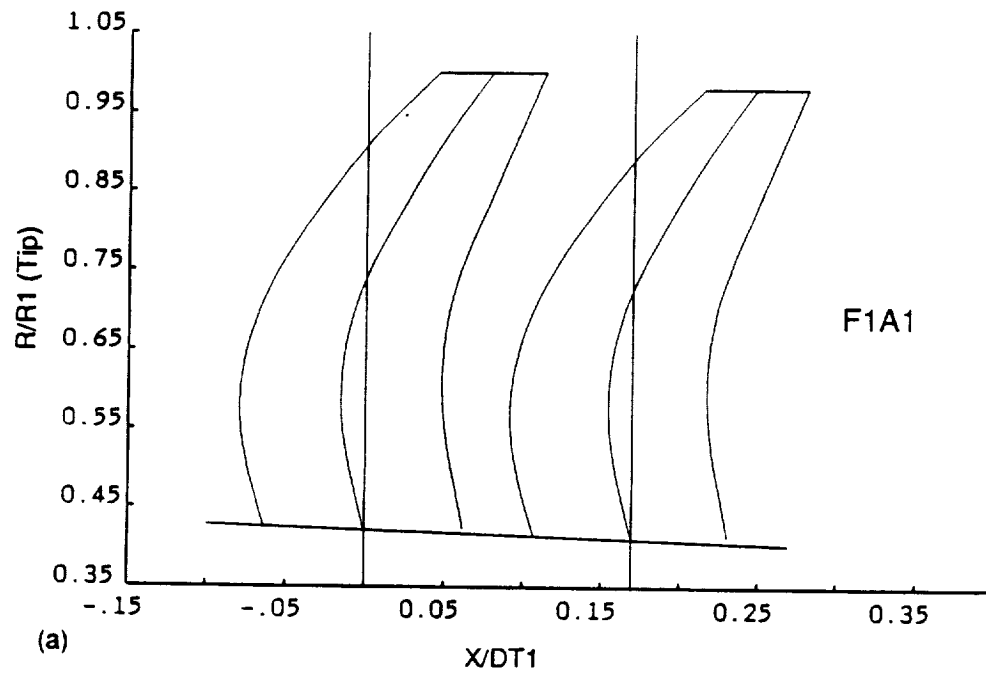
Figure 7.   F1A1 and F1A3 Blade Design Planforms.

12

In order to assess the ability of the computer program to predict the noise characteristics of the reduced diameter A3 design, data/theory comparisons have been made for both F1A1 and F1A3 blade configurations operating at their design point ($M_o = 0.72$, $M_{HT} \approx 1.08$ for the forward rotor) in the NASA Lewis Research Center 8x6 foot transonic tunnel. The results are shown in Figures 8 through 10 and Figures 12 and 13. Figures 8 and 9 show comparisons between data and prediction for acoustic run No. 4722; F1A1 blades in a 9+8 configuration, enabling identification of the individual rotor harmonics. Comparisons between measurement and prediction for the first four harmonics of BPF are shown in Figure 8 for the forward rotor and in Figure 9 for the aft rotor. Two prediction curves are shown; the first, "PREDICTION" employed the local pitch angle to divide the lift into thrust and torque components in the acoustic calculation, while for the second, "PREDICTION (HEL)", the helicoidal surface angle was used. As was the case for the SR-7L predictions of Reference 1, there is close agreement between the two prediction curves for this design point calculation, although, as a general rule, it has been found that use of the local pitch angle gives better agreement with data. These Figures demonstrate good agreement between data and prediction for this high Mach number case, the only notable exception being that the predicted directivity of the fundamental BPF tone of the forward rotor (Figure 8(a)) is broader than that measured. Some differences between data and prediction in the forward arc can, as before, be attributed to the attenuating effect of the boundary layer on the flat plate for the harmonics above BPF.

Acoustic run 4793 is identical in operating conditions to run 4722 shown previously, but with eight A3 blades replacing the A1 blades of the earlier run. Figure 10 can be compared with Figure 8 to obtain a measure of data repeatability, in that both show tones from the F1 blading under the same conditions. Here, only three harmonics of BPF were available for comparison, as a result of higher static temperature in the tunnel during this run than was the case for run 4722. Higher static temperature requires higher physical speeds to maintain equivalent Mach numbers, thus with higher rpm, the fourth harmonic of BPF for the nine-bladed forward rotor was above the frequency range of the analyzer used to obtain these on-line data. Other than this, the comments concerning the agreement between data and prediction shown in Figure 8 apply to Figure 10 also.

The computer code delivered under this contract contains the assumption that the streamline that passes through the tip of the forward rotor will also pass through the tip of the aft rotor. In general, under cruise conditions, this assumption is correct. For the reduced diameter rear rotor under consideration here, however, the forward rotor tip streamline will pass over outboard of the tip of the aft rotor, and this physical situation should be addressed in the computational scheme. The approach adopted requires the generation of imaginary or "pseudo" blade coordinates to represent a full-diameter rear rotor that is identical in all respects with the real blade, (in the region where that blade exists) but extends past the true blade tip to the "standard" diameter. During the computation, the streamlines are distributed on the full-diameter (or "grown") blade, but only those contributors to the noise that lie within the real reduced diameter (or "clipped") blade are included in the acoustic calculation. This concept of the "grown" and the "clipped" blade is illustrated in Figure 11. The effect on the predicted noise of allowing the forward rotor tip streamline to pass outside the tip of the aft rotor is shown in Figure 12 where results labelled "Design" (representing a calculation in which the forward rotor tip streamline does pass through the tip of the aft rotor) and "grow/clip" (representing a calculation using the "grown" and "clipped" technique described above) are compared with data from run 4793.

13
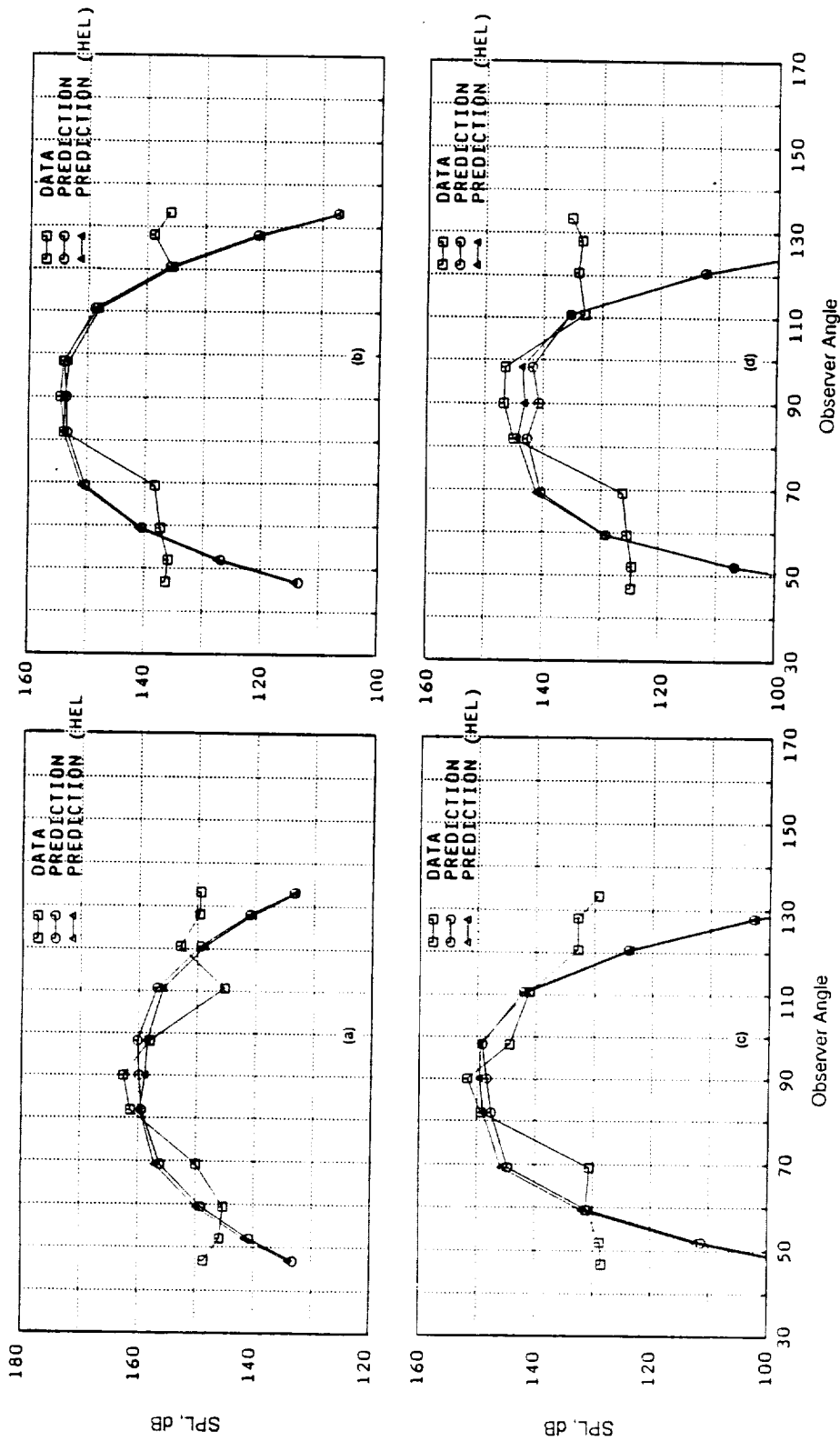
Figure 8. Comparison Between Data Acquired in the NASA Lewis Research Center 8x6 ft Transonic Wind Tunnel and Prediction: Acoustic Run 4722, F1 Blade Design, Mo = 0.72, 100% RPM$_c$. (a) BPF1; (b) 2*BPF1; (c) 3*BPF1; (d) 4*BPF1.
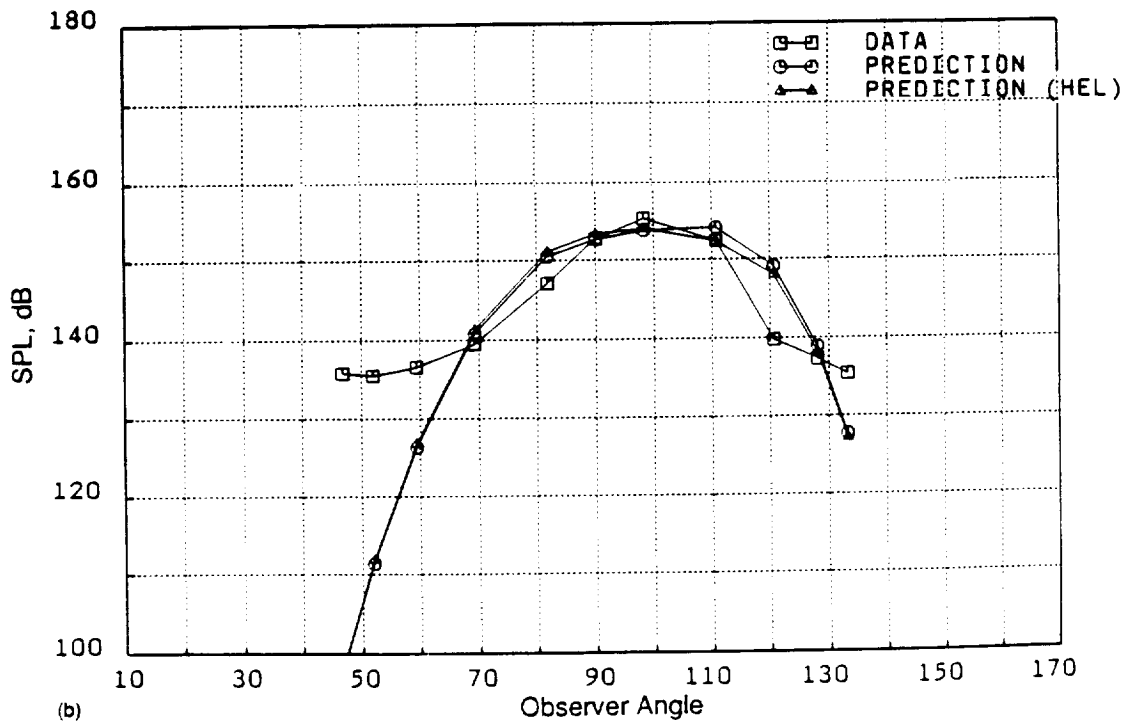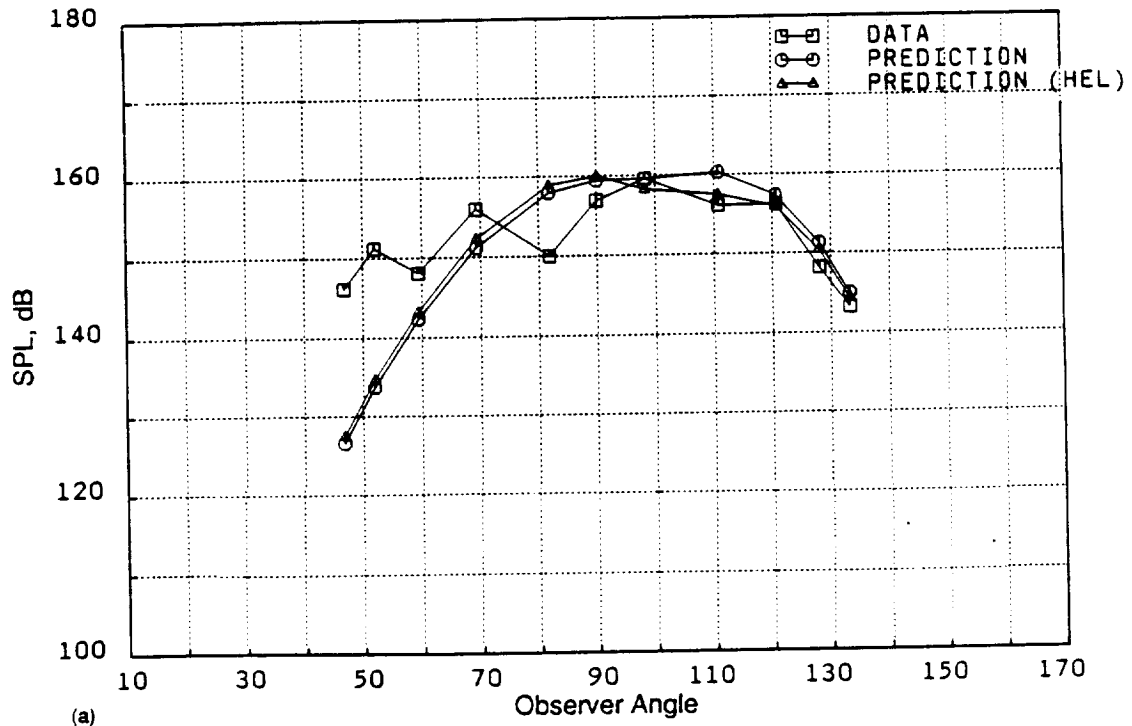
14

Figure 9. Comparison Between Data Acquired in the NASA Lewis Research Center 8x6 ft Transonic Wind Tunnel and Prediction: Acoustic Run 4722, A1 Blade Design. Mo = 0.72, 100% RPM$_C$. (a) BPF2; (b) 2*BPF2; (c) 3*BPF2; (d) 4*BPF2.

15

Figure 9. Comparison Between Data Acquired in the NASA Lewis Research Center 8x6 ft Transonic
Wind Tunnel and Prediction: Acoustic Run 4722, A1 Blade Design, Mo = 0.72, 100% RPM$_c$.
(a) BPF2; (b) 2*BPF2; (c) 3*BPF2; (d) 4*BPF2 (Concluded).

16
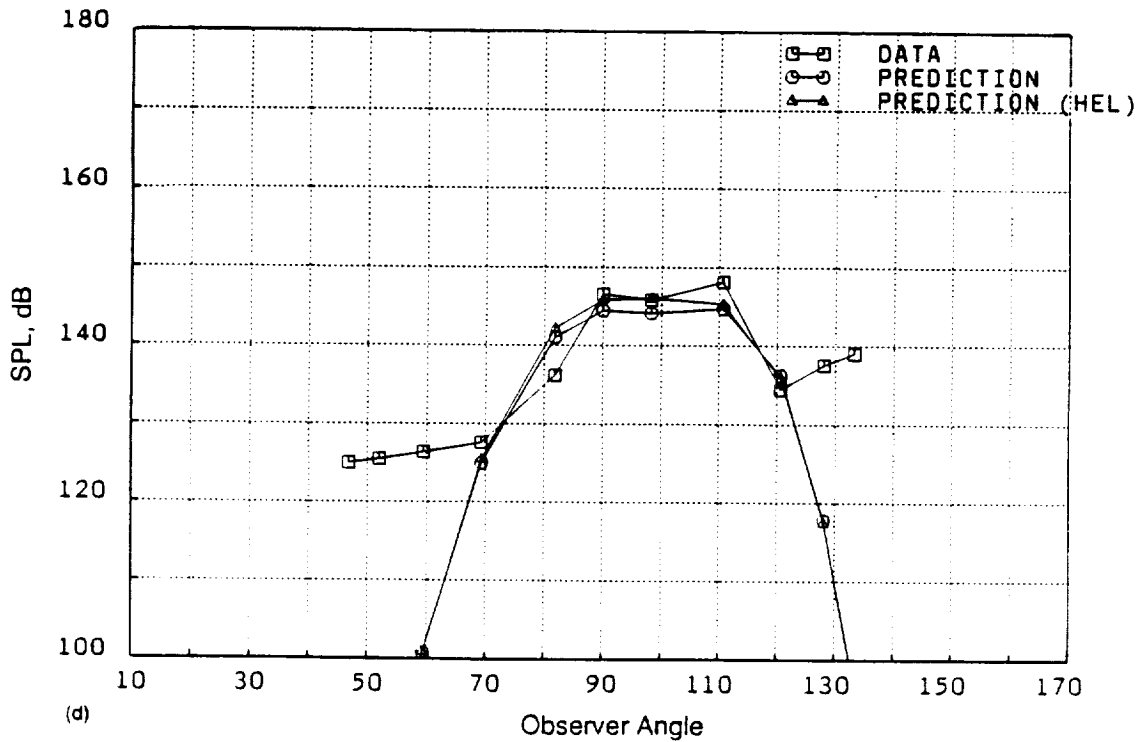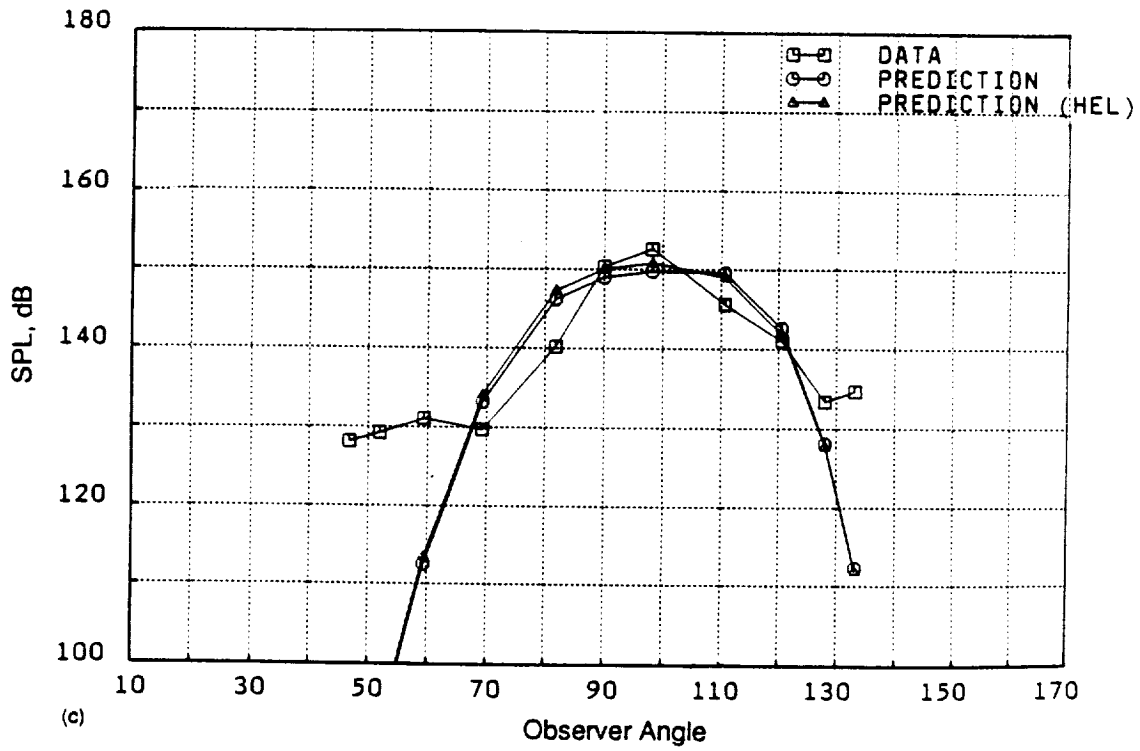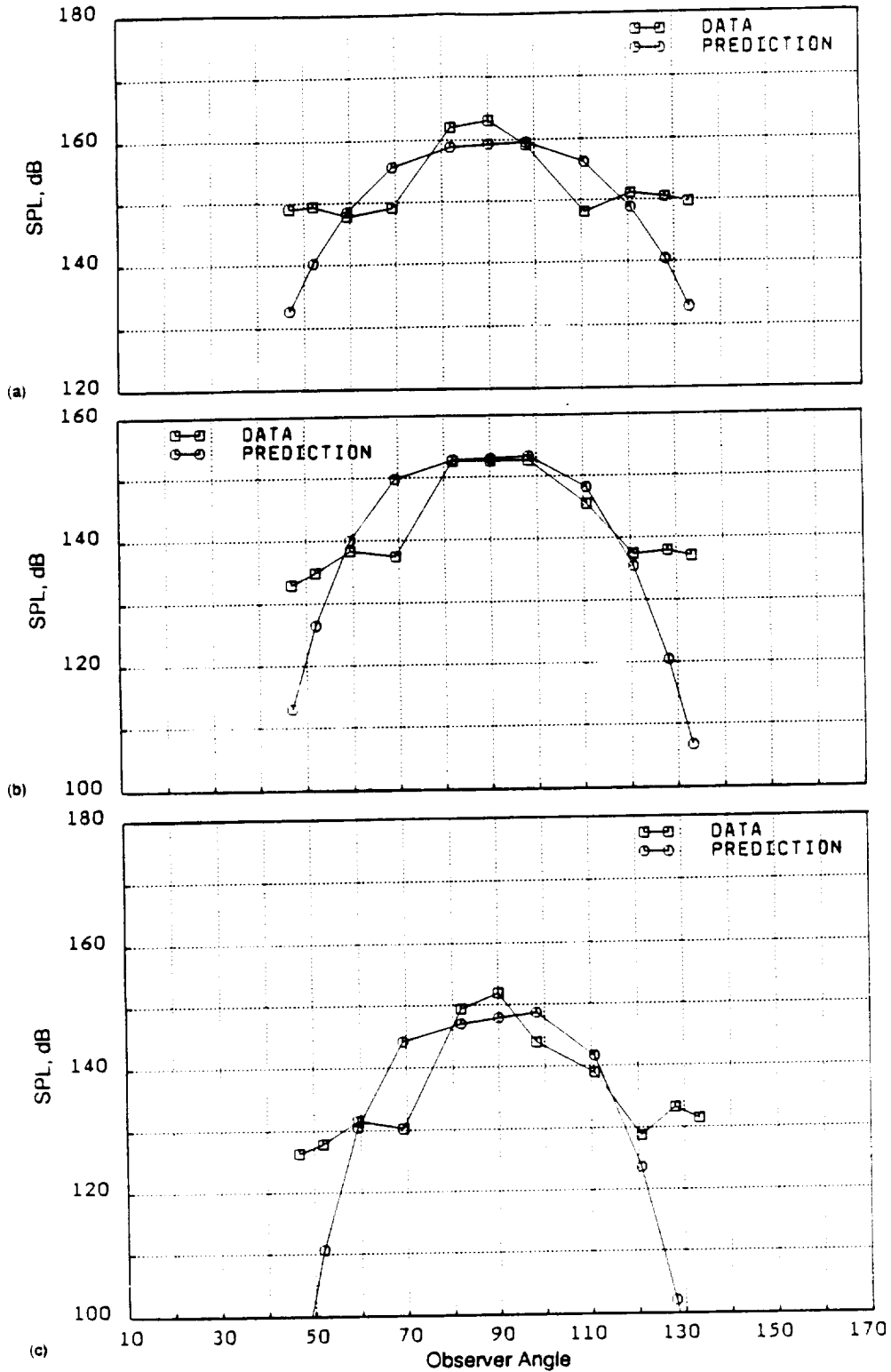
Figure 10. Comparison Between Data Acquired in the NASA Lewis Research Center 8x6 ft Transonic Wind Tunnel and Prediction: Acoustic Run 4793, F1 Blade Design, $M_0 = 0.72$, 100% RPM_c. (a) BPF1; (b) 2*BPF1; (c) 3*BPF1.

17
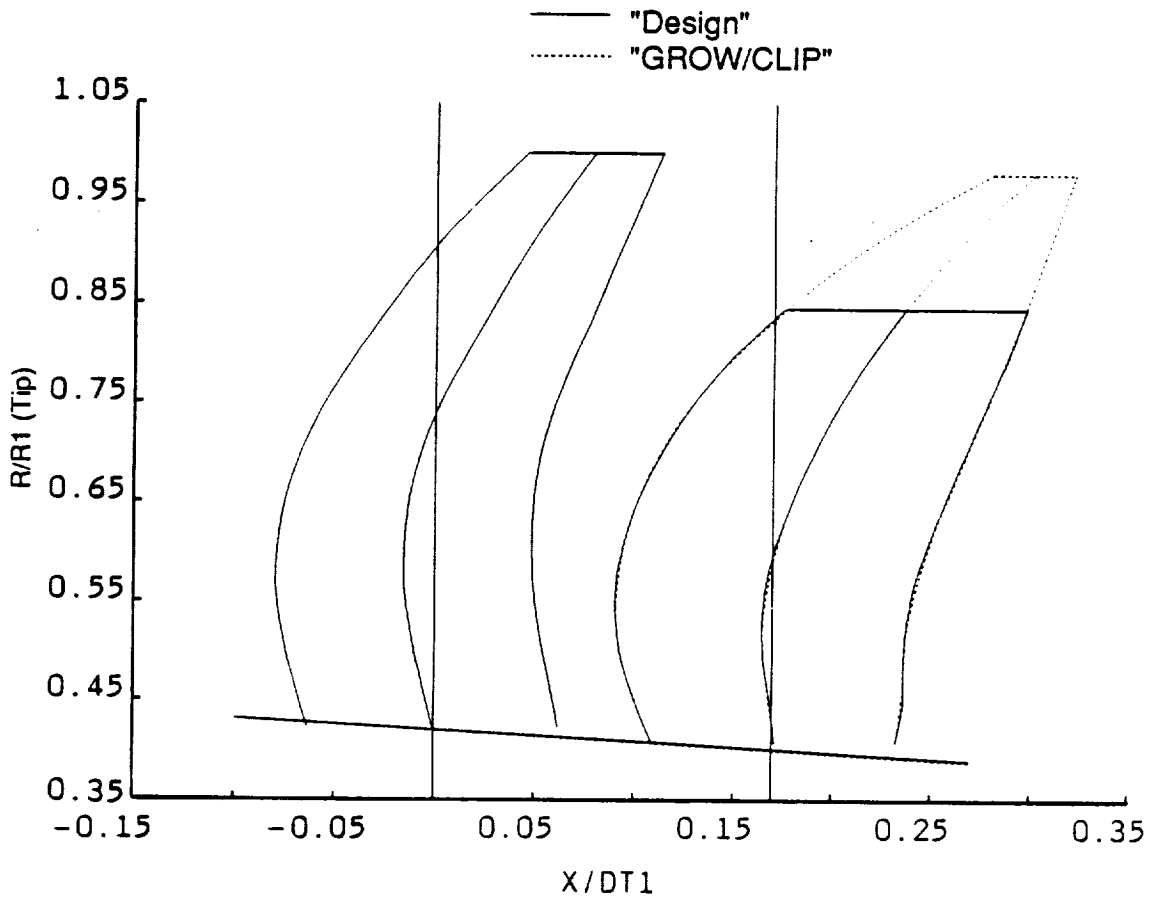
Figure 11. Comparison of A3 Blade Design with "GROW/CLIP" Pseudo-Blade.

18

Figure 12. Comparison Between Data Acquired in the NASA Lewis Research Center 8x6 ft Transonic Wind Tunnel and Prediction: Acoustic Run 4793, A3 Blade Design, Mo = 0.72, 100% RPMc. (a) BPF2; (b) 2*BPF2; (c) 3*BPF2; (d) 4*BPF2.

19

Figure 12. Comparison Between Data Acquired in the NASA Lewis Research Center 8x6 ft Transonic Wind Tunnel and Prediction: Acoustic Run 4793, A3 Blade Design, Mo = 0.72, 100% RPMc. (a) BPF2; (b) 2*BPF2; (c) 3*BPF2; (d) 4*BPF2 (Concluded).

20

(a)

(b)

Figure 13. Comparison Between Data Acquired in the NASA Lewis Research Center 8x6 ft Transonic Wind Tunnel and Prediction: Acoustic Run 4793, A3 Blade Design, Mo = 0.72, 100% RPM$_c$. (a) BPF2; (b) 2*BPF2; (c) 3*BPF2; (d) 4*BPF2.

(c)

(d)

Figure 13. Comparison Between Data Acquired in the NASA Lewis Research Center 8x6 ft Transonic Wind Tunnel and Prediction: Acoustic Run 4793, A3 Blade Design, $M_o = 0.72$, 100% RPM_c. (a) BPF2; (b) 2*BPF2; (c) 3*BPF2; (d) 4*BPF2 (Concluded).

What little difference there is between the two predictions is probably a function of the different spanwise loading distributions that resulted from the two approaches. Rather more disturbing is the disagreement between data and prediction seen in all harmonics above the fundamental shown in this figure. No fully satisfactory explanation for this discrepancy has been found. If, however, one assumes that either the loading or the thickness distributions that were assumed for this somewhat unconventional blade were in error, one may achieve the results shown in Figures 13 and 14, respectively. The original calculation (Figure 12) assumed that, for this high flight Mach number example, the normalized chordwise load distribution (described in detail in Reference 1) could, as is usual in this flight regime, be represented by a rectangle. In the event, the helical tip Mach number of the A3 blade is barely unity, suggesting that the parabolic load distribution normally employed for low flight speed cases might be more appropriate. Figure 13 demonstrates the sensitivity of the result to the chordwise loading distribution employed. Alternatively, errors in manufacturing could result in a thicker blade than that for which the predictions were made. Figure 14 shows the result of arbitrarily doubling the thickness of the blade (an extreme case). Again, the prediction moves closer to the data.

One further factor which can influence the predicted levels of the higher harmonics of BPF in particular is the chordwise thickness distribution. Figure 15 shows the effect of changing the leading edge thickness (ALE) from zero to 0.3 times the maximum thickness at any radial station, while simultaneously changing the trailing edge thickness (BTE) from zero to 0.4 times the maximum thickness. Figures 13 through 15 demonstrate the sensitivity of the model to certain input assumptions.

It should be explained here that the choice of zero for the parameters ALE and BTE was based on earlier data/theory comparisons for the F7A7 blading. Use of finite edge thickness values in those cases led to over-prediction of the measurements. The values of 0.4 and 0.3 for ALE and BTE respectively are extreme, and are intended merely to illustrate the range of variation in predicted noise levels resulting from changes in the input assumptions.

In conclusion, it has been shown that, under high speed conditions, the prediction model is in good agreement with measured data for F7A7 and F1A1 blading. A study of the sensitivity of the computer model to certain input quantities produced no fully plausible explanation for the underprediction of A3 tone noise.

2.1.3.2 Low Speed Comparisons

Low simulated flight speed acoustic data were taken under Contract NAS3–24080 in the NASA Lewis 9x15 foot acoustically treated low speed wind tunnel (Figure 16) and in the GE Aircraft Engines Cell 41 free–jet anechoic facility (Figure 17). As with the high speed testing of the previous section, the two facilities employ different philosophies in the acquisition of acoustic data from the Model Propulsion Simulators (MPS). In the 9x15 foot tunnel, accoustic data were taken using a floor–mounted traversing system at microphone sideline distances of 4.5 and 5.5 feet. (The results reported herein use data recorded by the 4.5 foot microphone). The GEAE Cell 41 free–jet anechoic facility is described in References 2 and 10 and shown in Figure 17. In contrast to the wind tunnel testing described earlier, here the MPS is supported in a vertical free jet inside a large (42 ft by 72 ft outside dimensions) anechoic chamber, with static microphones located in a vertical plane around the walls. The majority of the microphones are at a 27 foot sideline from the axis of the circular free jet, which is, itself, coincident with the axis of the MPS. In order to use the acoustic data taken in
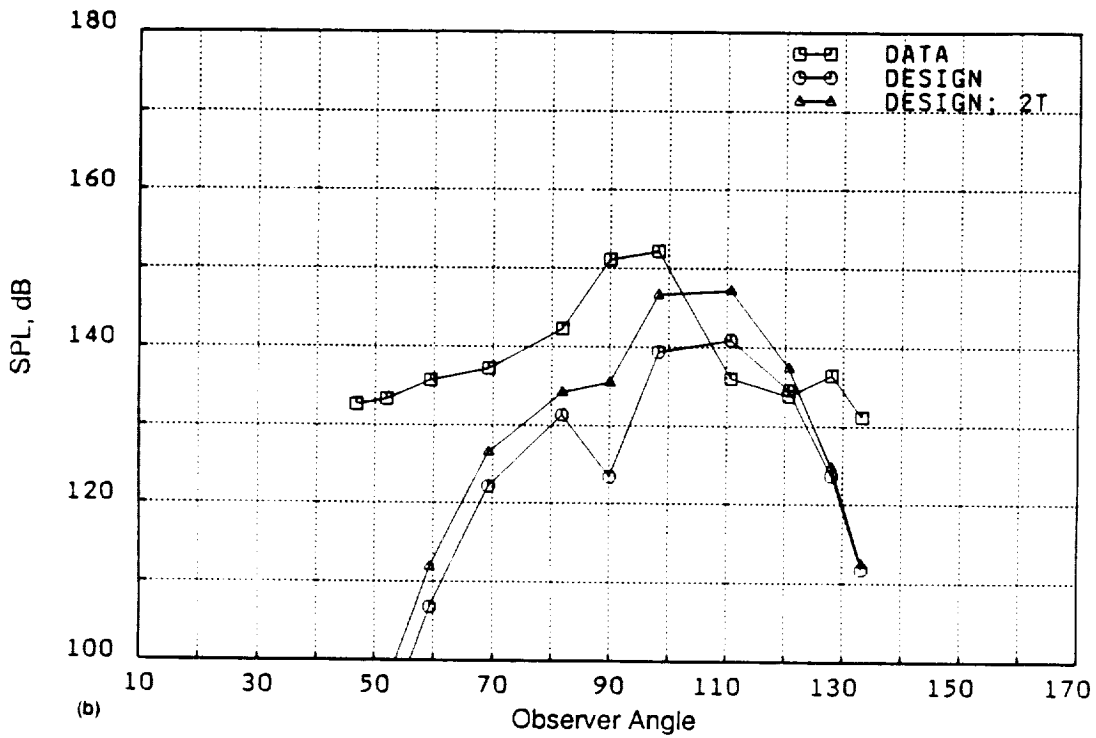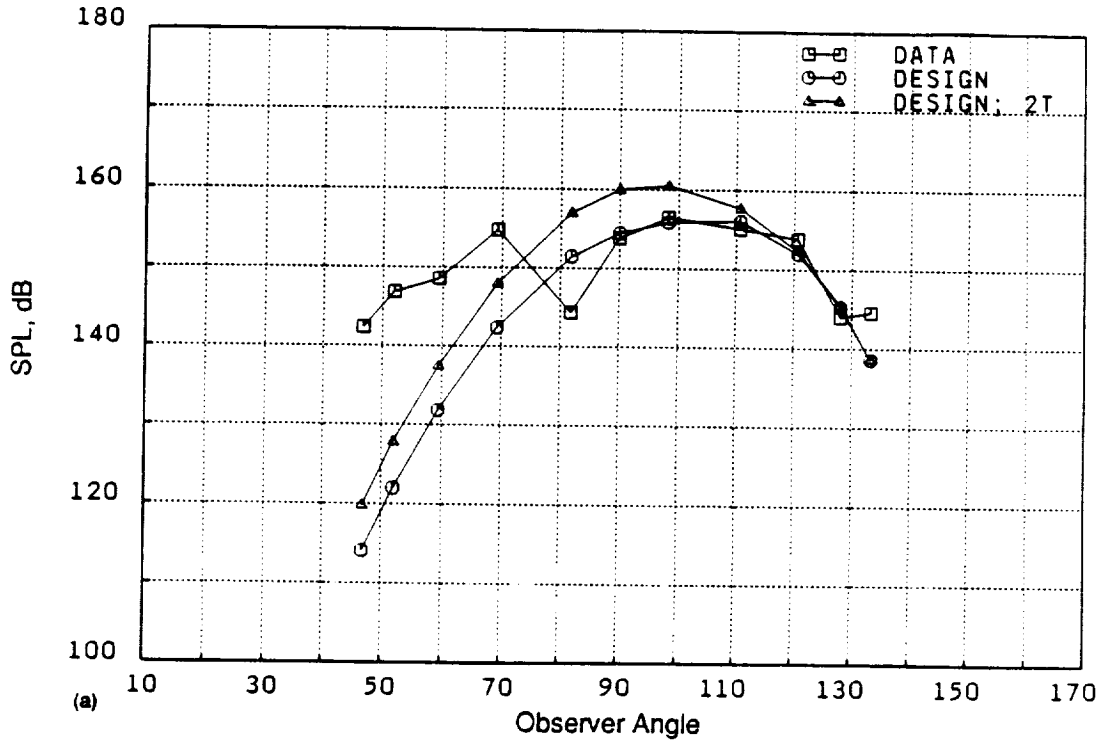
Figure 14. Comparison Between Data Acquired in the NASA Lewis Research Center 8x6 ft Transonic Wind Tunnel and Prediction: Acoustic Run 4793, A3 Blade Design, Mo = 0.72, 100% RPMc. (a) BPF2; (b) 2*BPF2; (c) 3*BPF2; (d) 4*BPF2.

Figure 14. Comparison Between Data Acquired in the NASA Lewis Research Center 8x6 ft Transonic Wind Tunnel and Prediction: Acoustic Run 4793, A3 Blade Design, Mo = 0.72, 100% RPM$_c$. (a) BPF2; (b) 2*BPF2; (c) 3*BPF2; (d) 4*BPF2 (Concluded).

25
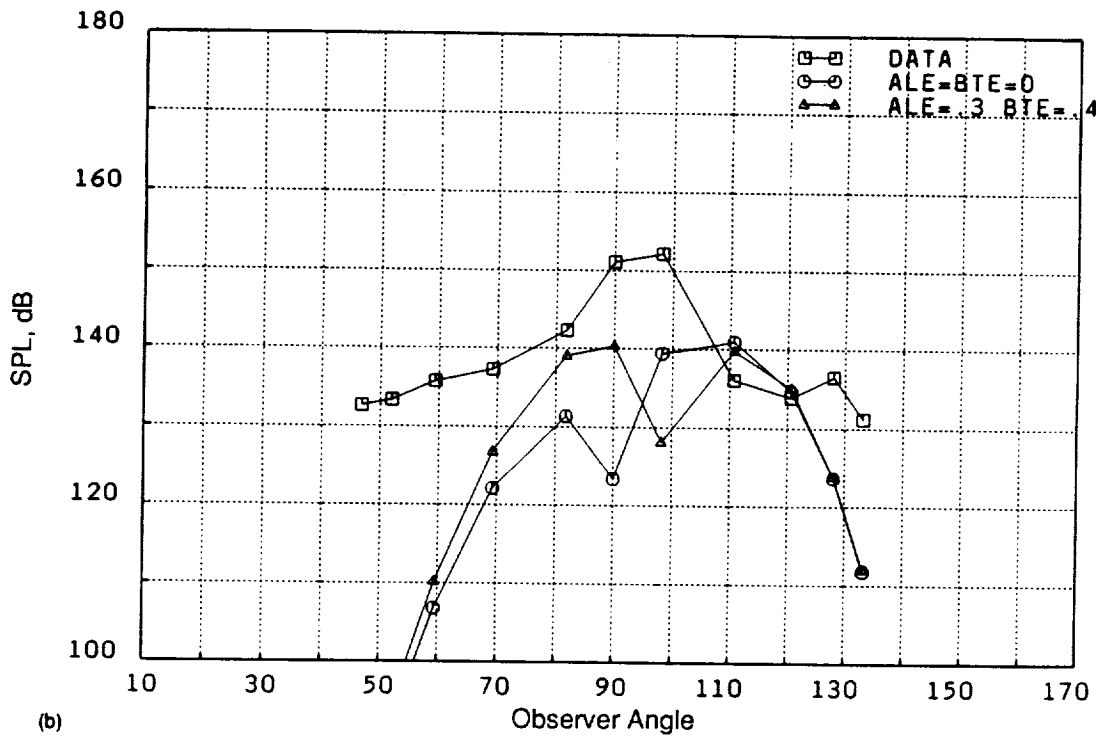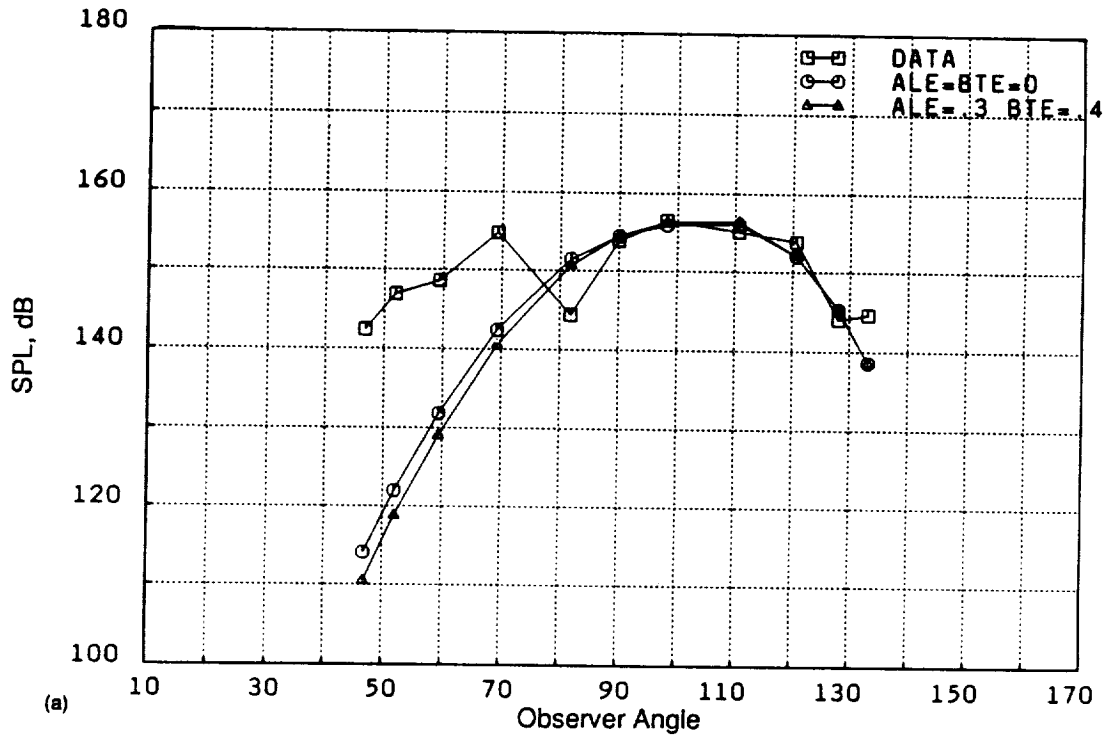
Figure 15. Comparison Between Data Acquired in the NASA Lewis Research Center 8x6 ft Transonic Wind Tunnel and Prediction: Acoustic Run 4793, A3 Blade Design, Mo = 0.72, 100% RPMc. (a) BPF2; (b) 2*BPF2; (c) 3*BPF2; (d) 4*BPF2.

Figure 15. Comparison Between Data Acquired in the NASA Lewis Research Center 8x6 ft Transonic Wind Tunnel and Prediction: Acoustic Run 4793, A3 Blade Design, Mo = 0.72, 100% RPMc. (a) BPF2; (b) 2*BPF2; (c) 3*BPF2; (d) 4*BPF2 (Concluded).
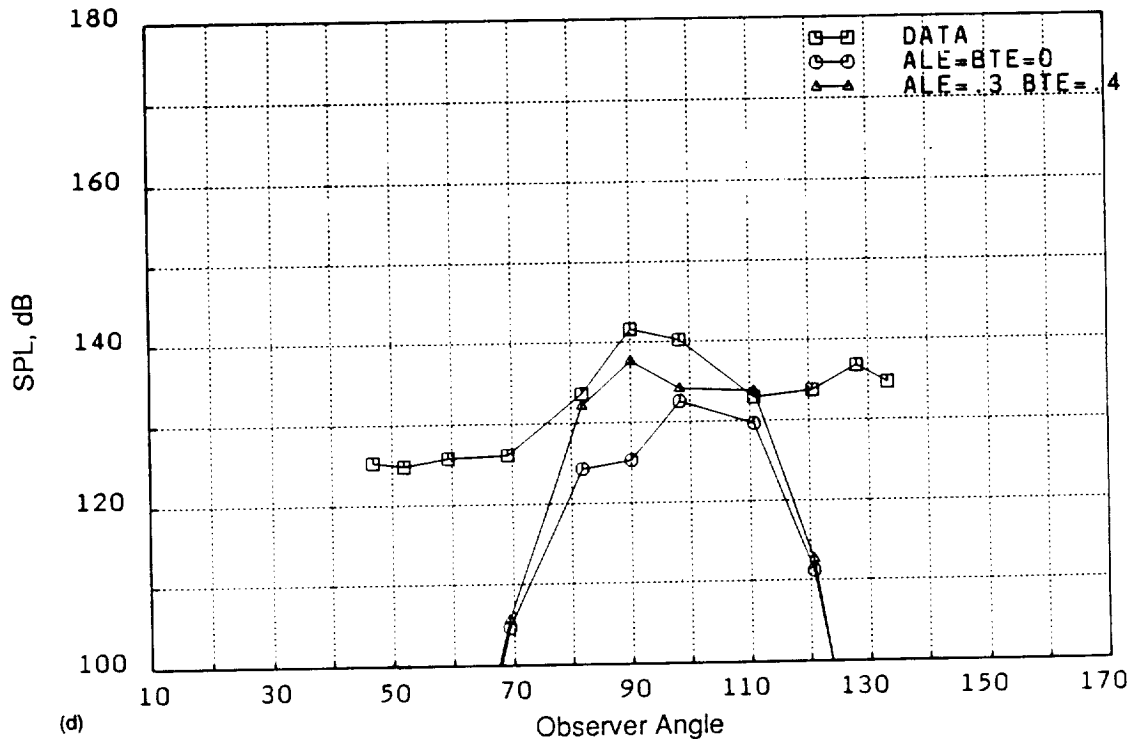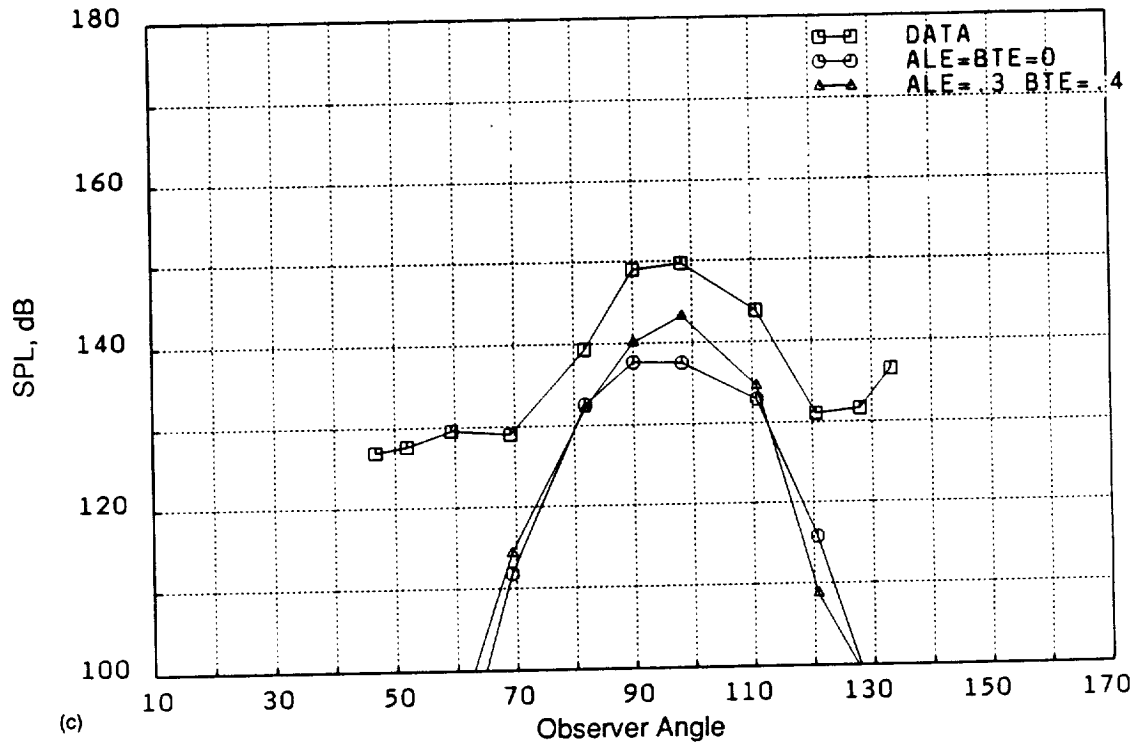
Figure 16. MPS (Model Propulsion Simulator) and Traversing Microphones in the NASA Lewis Research Center 9x15 foot Low Speed wind Tunnel (from Reference 9).
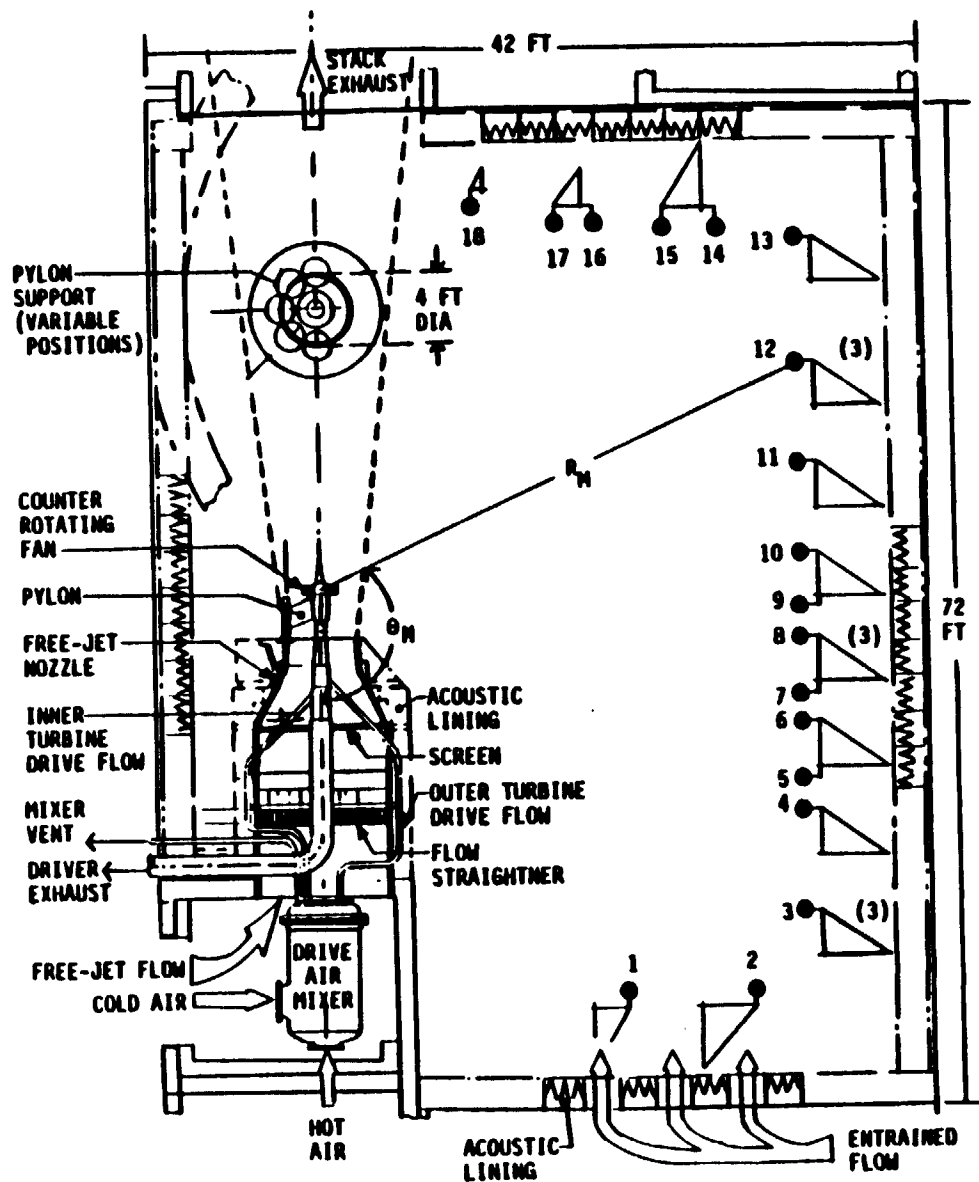
- **4 FT DIAMETER FREEJET**
- **MACH NUMBER: 0.3 (max)**
- **18+6 WALL MICROPHONES**
- **GEOMETRIC ANGULAR RANGE: 43° - 154°**

MIC No.	Radial Distance R, ft.	Angular Location θ, degrees
1	29.4	42.9
2	32.1	47.9
3	32.0	57.6
4	29.3	67.2
5	28.4	72.0
6	27.7	76.9
7	27.3	81.8
8	27.0	86.7
9	27.0	91.7
10	27.2	96.8
11	28.2	107.1
12	30.4	117.5
13	34.3	128.0
14	31.3	133.0
15	29.0	138.0
16	26.9	143.1
17	25.3	148.3
18	24.6	153.5

MICROPHONE LOCATIONS RELATIVE TO AXIAL MIDPOINT BETWEEN THE ROTORS THAT ARE 4.16 INCHES APART

Figure 17. MPS (Model Propulsion Simulator) in the GE Aircraft Engines Cell 41 Free Jet Anechoic Facility.

this facility, account must be taken of the effects of the shear layer between the moving fluid in the jet and the stationary fluid in the body of the facility. This is accomplished by means of the technique described in Reference 12.

Data/theory comparisons have been made for the F7A7, F7A3, and F11A11 blade designs shown in Figure 18. The data used for the F7A7 and F7A3 comparisons are from tests conducted in the 9x15 foot wind tunnel; the F11A11 data are from Cell 41. The F7A7 blade design, and the reduced diameter rear blade A3 were discussed previously, thus the only comment to be made at this point is the reminder that these blades were designed to operate at a flight Mach number of 0.72 in an 8-forward + 8-aft blade configuration. The F11A11 blades, on the other hand, were designed for a flight Mach number of 0.8 with 11-forward + 9-aft blades. In addition, as can be seen from Figure 18, the F11A11 planforms were designed with significantly more chord and sweep than F7A7. Figure 19 is a plot of the radial distribution of the axial distance from the trailing edge of the forward rotor to the 1/4-chord of the aft rotor, normalized by the axial chord of the forward rotor, for the F7A7 and F11A11 blades as tested. This parameter, together with the forward rotor drag coefficient, controls the strength of the wakes shed from the forward rotor when they encounter the aft rotor blades. Figure 19 demonstrates an attempt to reduce interaction noise by increasing the spacing between the blade rows.

2.1.3.2.1 F7A7 Comparisons

In view of the large amounts of data available for comparison with prediction, it was decided to concentrate on a few test points and examine them in detail, in order to demonstrate various aspects of the theoretical model.

Figure 20 shows typical data taken in the NASA 9x15 foot wind tunnel. The blades are F7A7 in an 11-forward plus 9-aft configuration, enabling identification of the various blade passing frequency harmonics and interaction tones. The data were obtained with the 4.5 foot sideline traversing microphone, and the angular location is referenced to the midpoint between the rotors, with zero degrees being the upstream axis. Figure 20(a) shows the acoustic spectrum obtained by averaging samples from the traversing microphone over the five degree segment centered on 90 degrees (the midpoint); with Figures 20(b) and 20(c) corresponding to upstream and downstream data respectively. The blade passing frequency (BPF) tones of the two rotors have been identified, together with the major "sum" tones ($n*BPF1 + m*BPF2$, where "m," "n" are integers). It can be seen from this figure that, whereas the BPF tones of the two rotors are visible above the background broadband level in the vicinity of 90 degrees, at the upstream and downstream locations shown they cannot be identified. In the comparisons that follow, both for BPF and the interaction tones, only those data points that protrude clearly above the broadband have been used.

2.1.3.2.1.1. "Standard" Comparisons

Comparisons between the as-measured data and prediction for acoustic run 367 (F7A7 11+9 blading, $\beta_{3/4} = 36.4/36.5$, RPM1 $\approx 6800 \approx$ RPM2) are shown in Figures 21 through 24. Figure 21 compares predicted and measured directivity patterns for the fundamental BPF tones of the two rotors. Agreement between the data and the predicted levels for these tones is disappointing at first sight, especially bearing in mind the agreement obtained for the same blading (albeit different blade numbers) at high speed (Figure 4). Examination of the data, however, shows the tones to be buried in the broadband noise (see Figure 20(b)) over most of the directivity, leaving only the region around
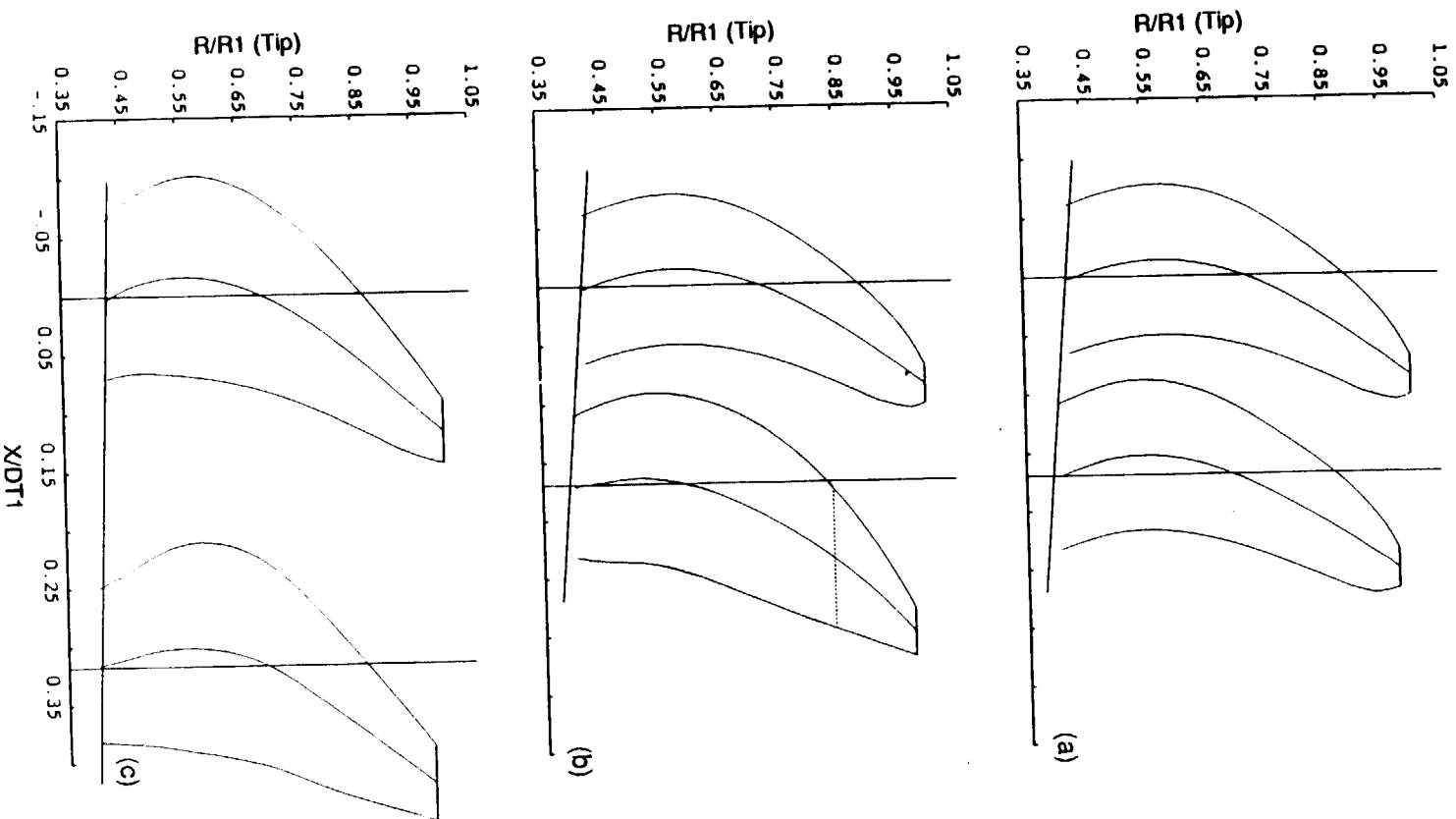
Figure 18. Planforms of: F7A7 (a), F7A3 (b) and F11A11 (c) Blade Designs.

31

GEOMETRIC PARAMETERS AFFECTING UDF ACOUSTICS
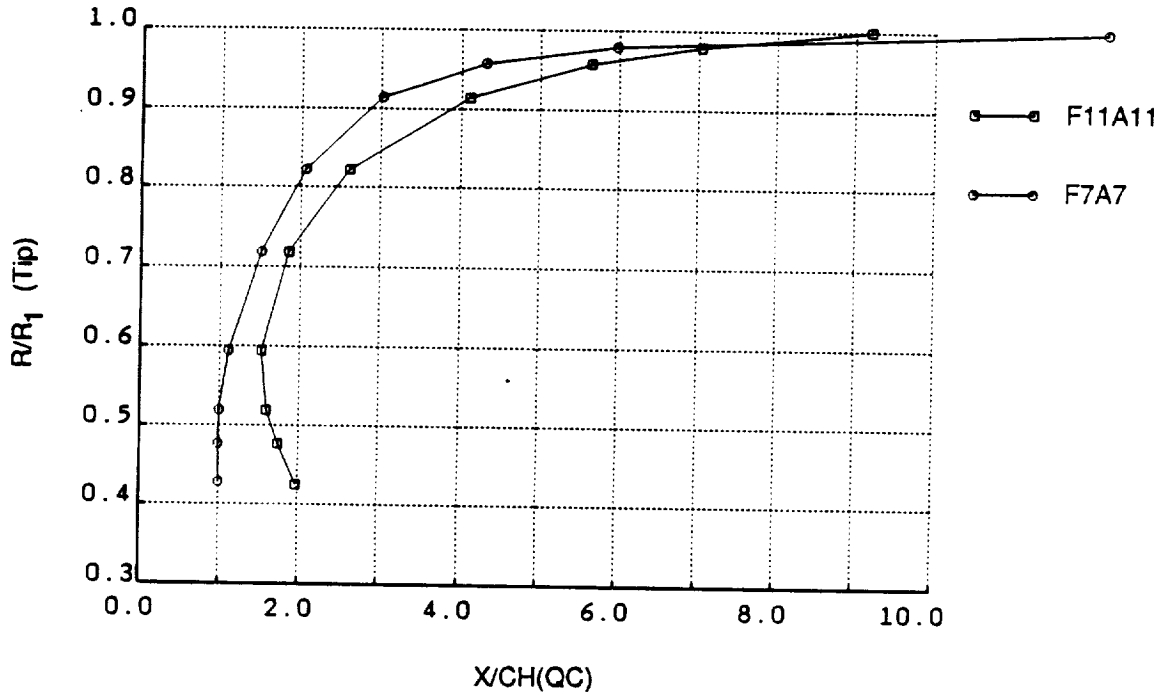
Figure 19. Comparison of (Axial Distance : Chord) Ratio for F7A7 and F11A11 Blade Designs.

NASA LERC 9X15 LSWT (11+9) F7A7
FWD RPM = 6780 , AFT RPM = 6840
FWD BETA= 36.4 , AFT BETA = 36.5
80.0% SPEED , NOMINAL SPACING
DATE:23-JAN-87 , TAPE: DUB #17
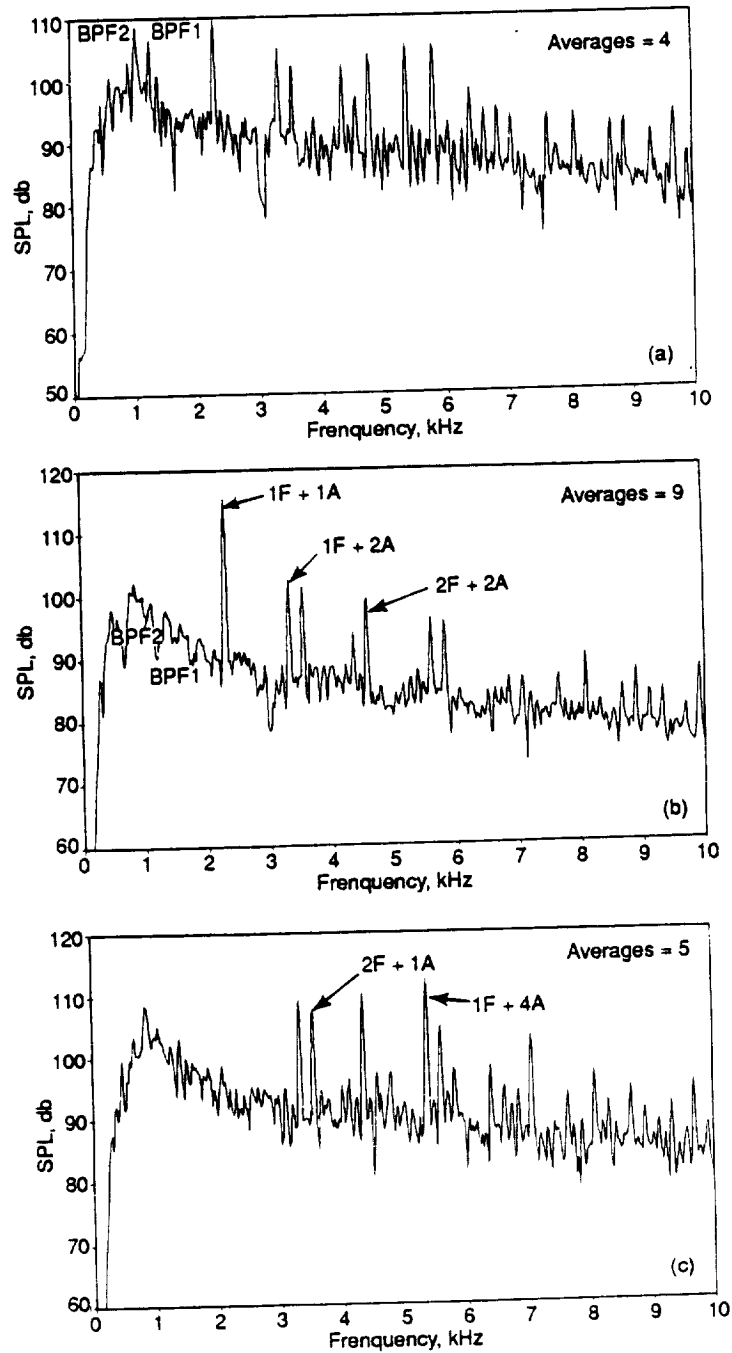
Figure 20. **Typical Data from the NASA Lewis Research Center 9x15 foot Wind Tunnel: Acoustic Run 367, F7A7 (11 + 9) Blades, Mach 0.2, 80% RPM$_c$. (a) Between the Rotors; (b) Upstream; (c) Downstream.**
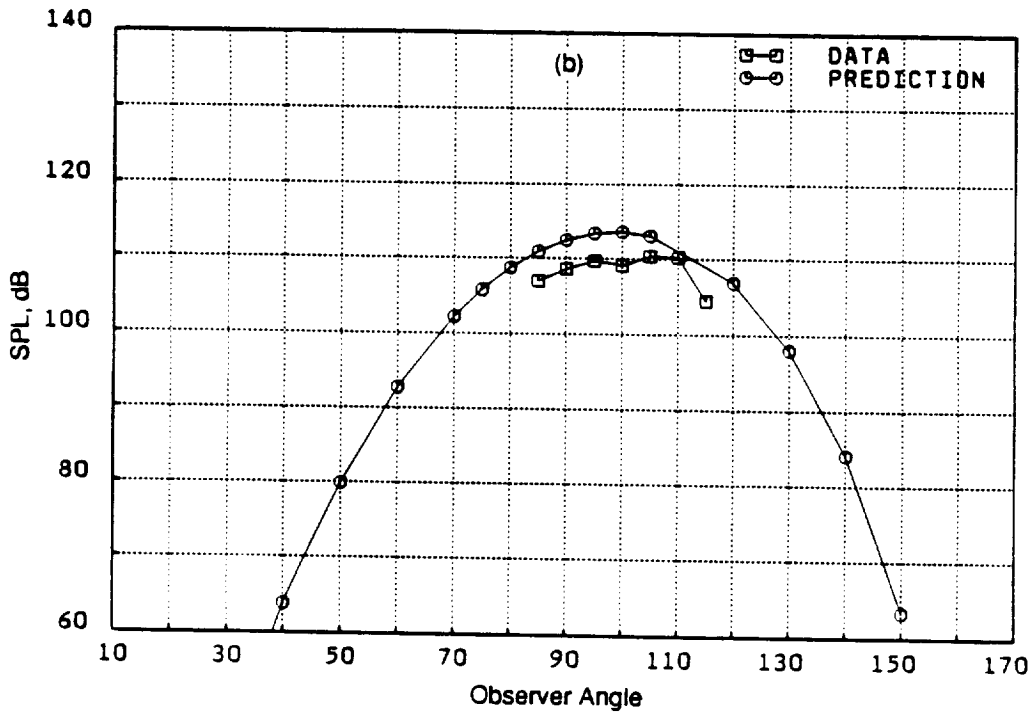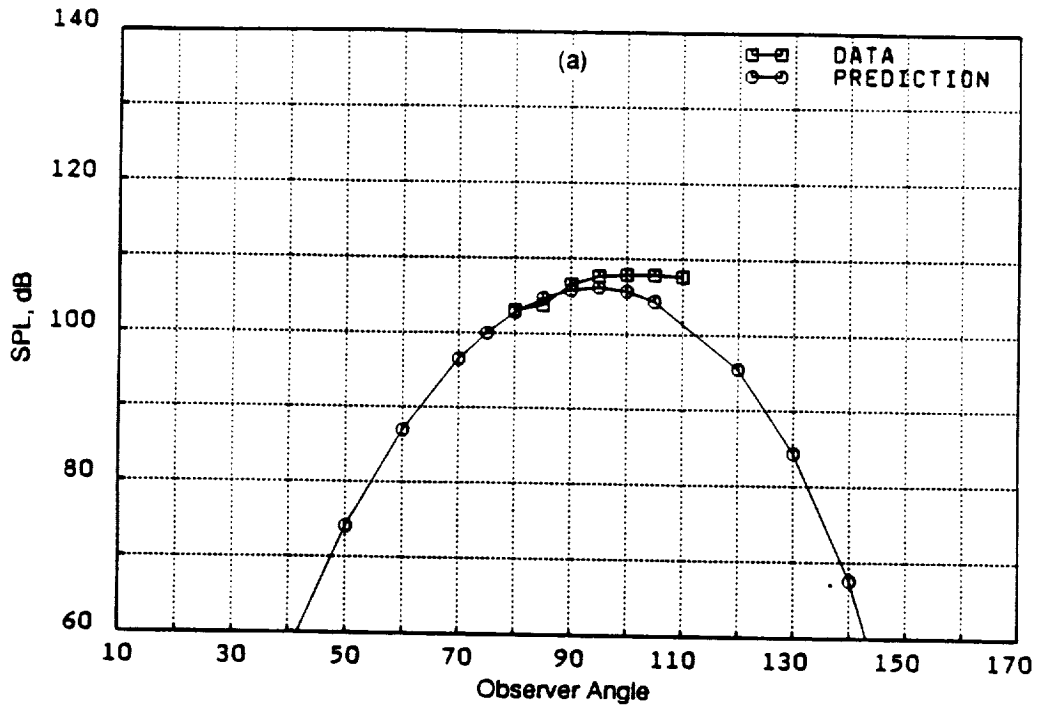
Figure 21. Comparison Between Data Acquired in the NASA Tunnel and Prediction: Acoustic Run 367, F7A7 (11 + 9) Blades, Mach 0.2, 80% RPMc. (a) BPF1; (b) BPF2.
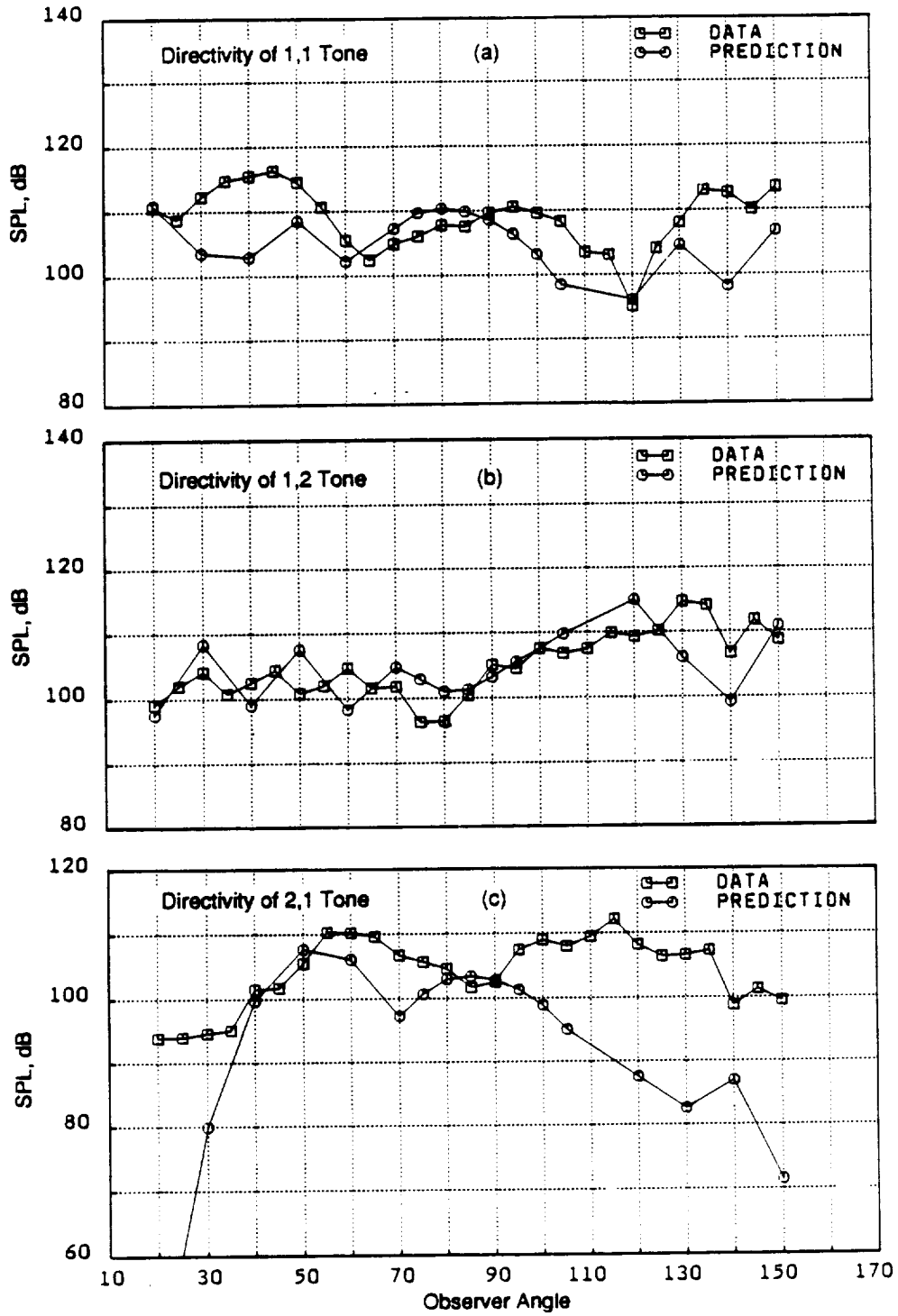
Figure 22. Comparison Between Data Acquired in the NASA Tunnel and Prediction: Acoustic Run 367, F7A7 (11 + 9) Blades, Mach 0.2, 80% RPM$_c$. (a) 1F + 1A; (b) 1F + 2A; (c) 2F + 1A.
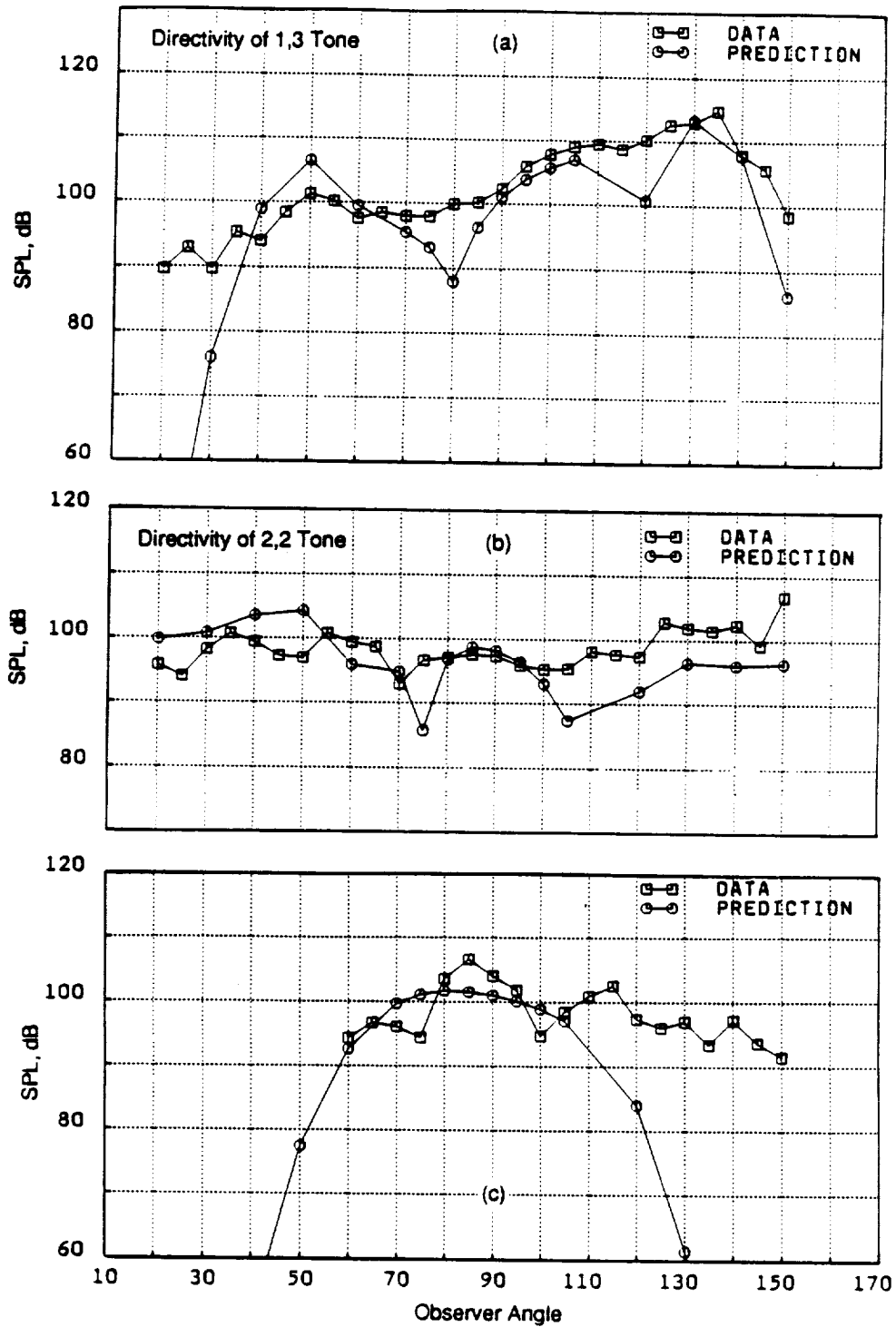
Figure 23. Comparison Between Data Acquired in the NASA Tunnel and Prediction: Acoustic Run 367, F7A7 (11 + 9) Blades, Mach 0.2, 80% RPMc. (a) 1F + 3A; (b) 2F + 2A; (c) 3F + 1A.
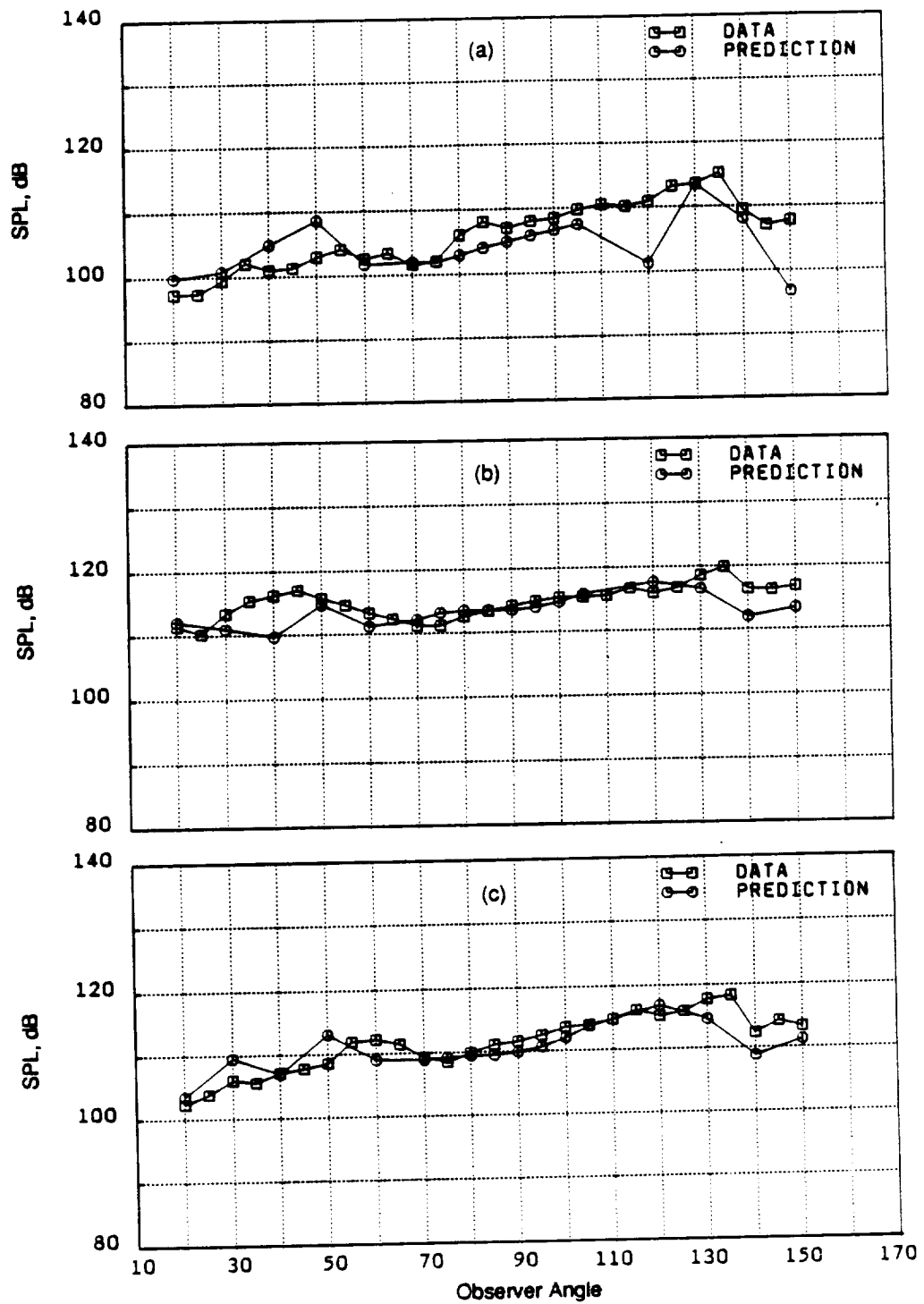
Figure 24. Comparison Between Data Acquired in the NASA Tunnel and Prediction: Acoustic Run 367, F7A7 (11 + 9) Blades, Mach 0.2, 80% RPMc. (a) "4th Harmonic"; (b) Rotor/Rotor Interaction Tone Sum; (c) "3 + 4 + 5 Harmonic" Tone Sum.

the rotors (between observer angles of 75° and 120°) open to question. Possible causes for the discrepancy between data and prediction in this region will be examined later.

Comparisons between predicted and measured levels for six interaction tones are shown in Figures 22 and 23 with tone sum comparisons shown in Figure 24. At the low simulated flight speed (M_0 = 0.2) at which these test were made, it is the interaction tones that are the main contributors to the measured noise; thus, the 1F + 1A tone of Figure 22(a) represents the "second harmonic" of blade passing frequency, with the 1F + 2A and 2F + 1A tones of Figure 22(b) and 22(c) combining to give the "third harmonic" level. Agreement between data and prediction is good for the 1F + 1A and 1F + 2A tones; the main features of the data are seen in the prediction (with a slight shift in directivity in the 1F + 1A tone) and the levels are in good agreement over the full directivity pattern. The same could be said for the 2F + 1A tone up to an observer angle of 90°; again, there is a forward shift of the directivity pattern in the predicted curve, relative to the data, but other than this, in the forward arc, agreement is good. Aft of 90°, the trends in the data and prediction are opposite. In these locations, as can be seen in Figure 20(c), the 2F + 1A tone protrudes strongly from the broadband, and the reason for the discrepancy between measured and predicted levels is, at present, not fully understood. In Figure 23, the data and prediction for the three tones that comprise the "fourth harmonic" are compared. Once again, the theoretical model shows very good agreement with the measured data for both the 1F + 3A and 2F + 2A tones. The forward arc 3F + 1A tone data were buried in the broadband level, thus allowing the difference between measured and predicted levels in this regime; but, again, in the aft arc, the differences between measurement and prediction warrant further study.

Figure 24 demonstrates the overall agreement between data and prediction obtained for this test point. The individual tones (both data and prediction) presented in Figure 23 have been summed to show the agreement in the "fourth harmonic" directivity (Figure 24(a)), while the levels in Figure 24(b) represent the sum of all interaction tones through the "seventh harmonic". Figure 24(c) shows the agreement between data and prediction for the interaction tones contributing to the third, fourth, and fifth harmonics. Experience has shown that it is these tones that have the greatest influence on the metrics used in the measurement of community noise from full–scale engines.

Figures 21 through 24 thus demonstrate excellent agreement between measured data and the "standard" theoretical prediction. This could be expected, since (Reference 7) the various semiempirical parameters employed in the tip vortex prediction model were calibrated using F7A7 blading.

2.1.3.2.1.2 "Optional" Comparisons

The isolated rotors prediction computer code delivered under this contract has several options available to assist the user in the prediction of noise from counterrotating high speed turboprops. Those concerned with the location (radial and tangential) and strength of the tip vortex have been discussed at length in Reference 7; this discussion is not repeated here. The overall effect of the tip vortex model, however, is shown in Figures 25 through 27. These Figures are the same as Figures 22 through 24, with one additional curve to show the prediction with no tip vortex effects included. It can be seen that, in this case, the inclusion of the tip vortex in the model is necessary to bring the prediction in line with the data. The only difference in the "prediction" curves in these figures lies in the presence or otherwise of the tip vortex in the flow field between the rotors. The development of the Rotor 1 wake is identical in both cases. Experience has shown that it is, in fact, possible to obtain reasonable agreement between data and prediction without employing the tip vortex model,

38
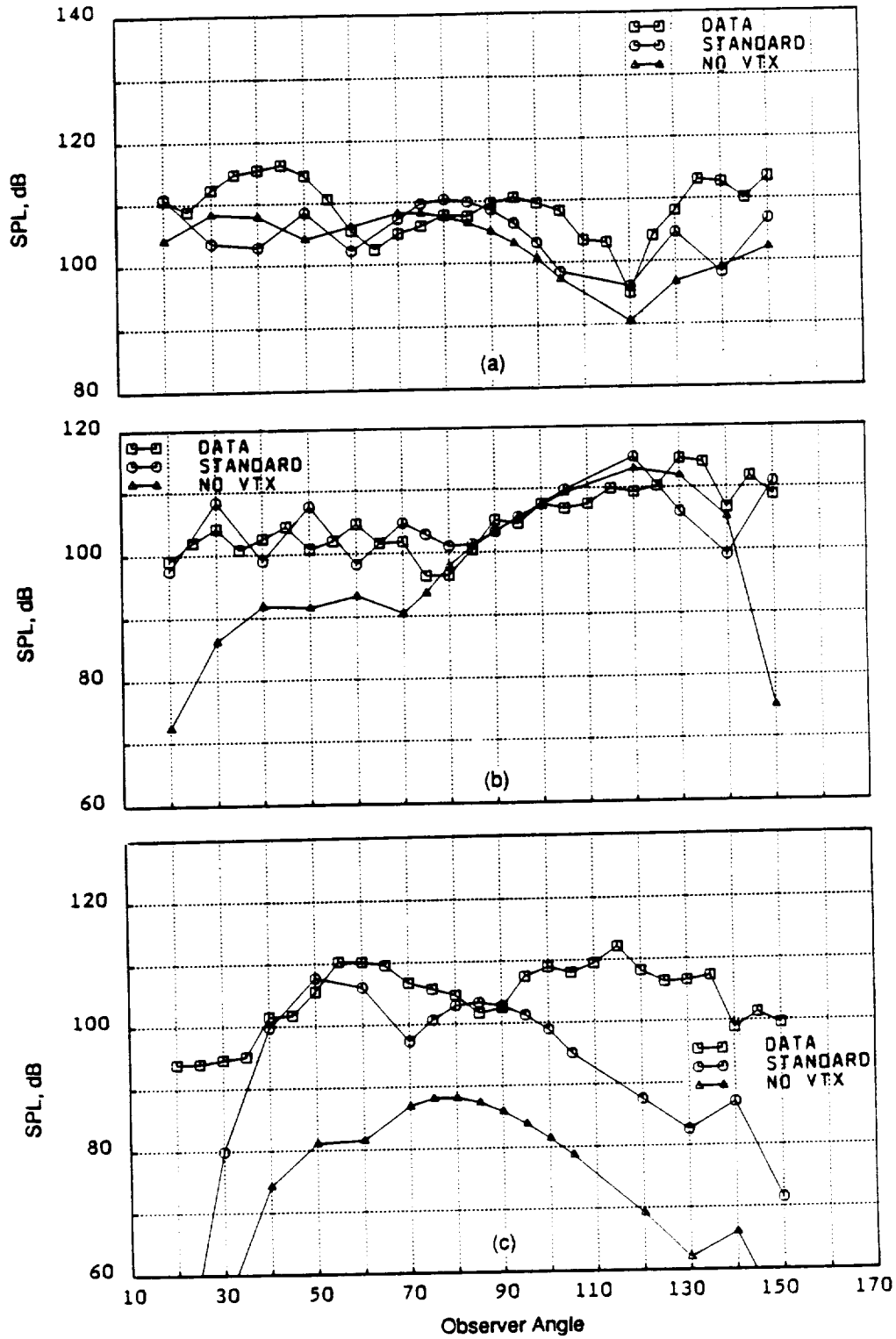
Figure 25. Comparison Between Data Acquired in the NASA Tunnel and Prediction: Acoustic Run 367, F7A7 (11 + 9) Blades, Mach 0.2, 80% RPMc. (a) 1F + 1A; (b) 1F + 2A; (c) 2F + 1A.
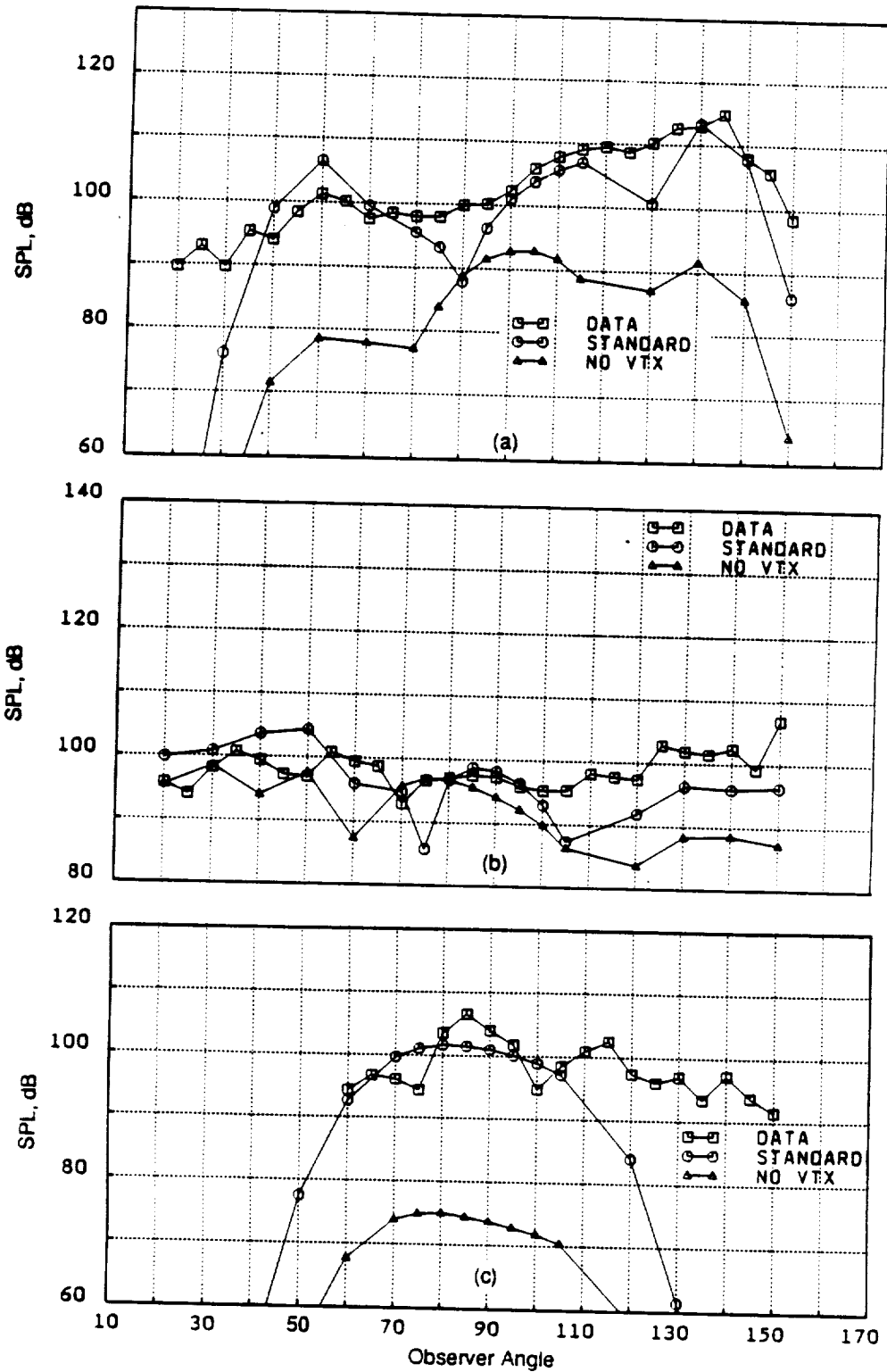
Figure 26. Comparison Between Data Acquired in the NASA Tunnel and Prediction: Acoustic Run 367, F7A7 (11 + 9) Blades, Mach 0.2, 80% RPM$_c$. (a) 1F + 3A; (b) 2F + 2A; (c) 3F + 1A.
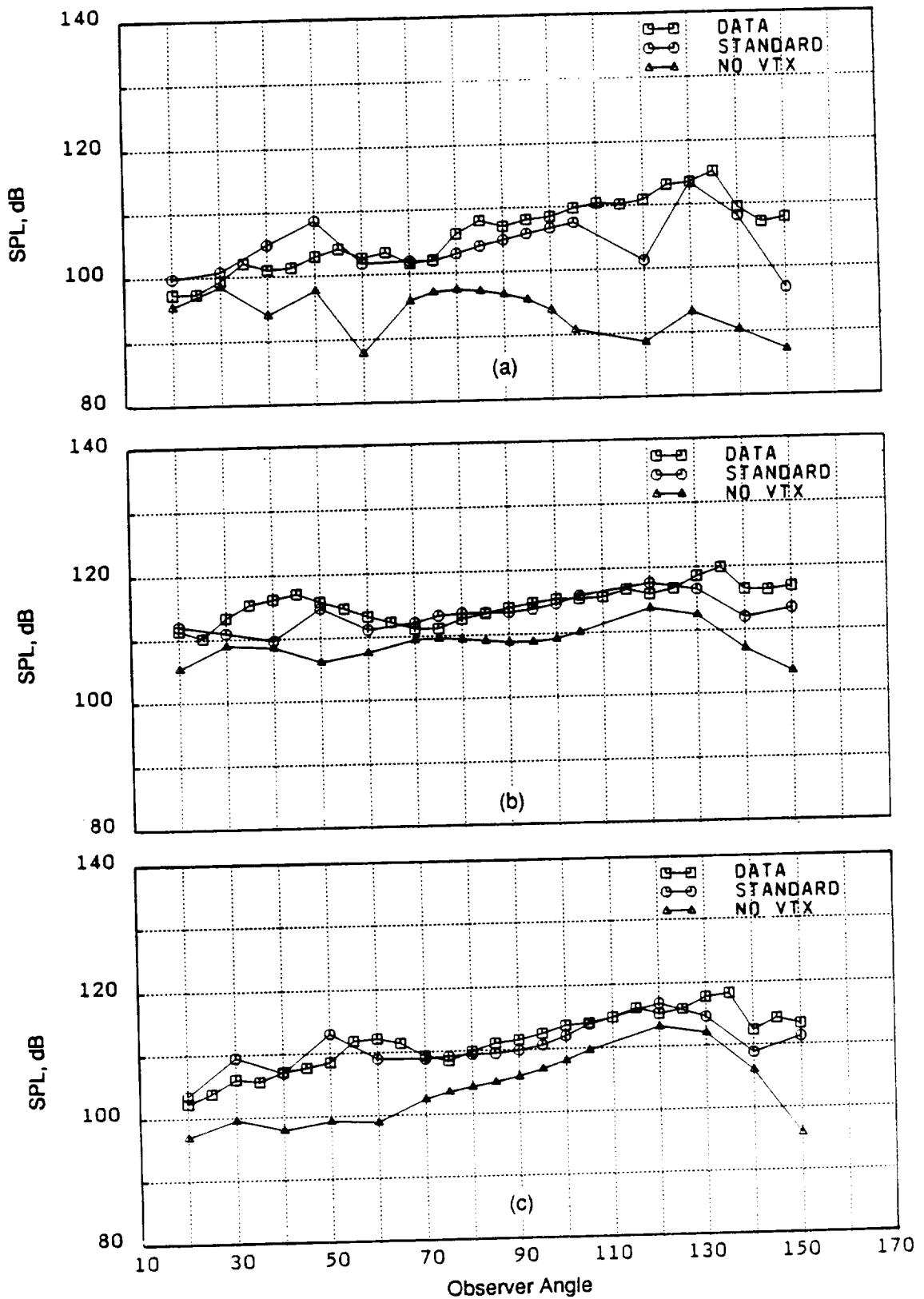
Figure 27. Comparison Between Data Acquired in the NASA Tunnel and Prediction: Acoustic Run 367, F7A7 (11 + 9) Blades, Mach 0.2, 80% RPMc. (a) "4th Harmonic"; (b) Rotor/ Rotor Interaction Tone Sum; (c) "3 + 4 + 5 Harmonic" Tone Sum.

provided suitable values are selected for the forward rotor drag coefficient distribution, against which the development of the wake is correlated. Figure 28 demonstrates the effects that can be achieved by a variation in drag coefficient. (It must be emphasized that the selection of drag coefficient should be made in such a way as to maintain consistency with either measured or predicted performance characteristics).

Figure 29 illustrates that the effects of the assumed spanwise loading distribution manifest themselves in the predictions of both the "steady loading" BPF tones and in the unsteady loading-generated interaction tones. The first effect is more obvious than the second, which results from modifications to the exit swirl from the forward rotor affecting the wake trajectory, as shown in Figure 30. The two spanwise loading distributions for which the predictions were made are shown in Figure 31. The total SHP absorbed in each case is the same, but the lift coefficient distributions are radically different. The curve labelled "ORIGINAL" was generated from an early flow solution of the blades under takeoff conditions, whereas that marked "DATA MATCH" contains the results of pressure/temperature surveys behind the second rotor. It is of interest to note, upon examination of Figure 29, that the "ORIGINAL" prediction is closer to the data than that obtained with the "DATA MATCH" loading. The final option exercised in this survey of features in the computer code is that of helicoidal surface versus pitch surface for the division of the lift on the blade into its thrust and torque components at any blade section. It will be recalled that, at high speed (Figures 8 and 9) there was very little difference between the two approaches. Here, on the other hand, at low speed, differences can be seen in both the steady and unsteady loading tones. Now when this exercise was performed for the (single rotation) SR–7L propfan operating on the Gulfstream PTA airplane under low flight Mach No. conditions, (Reference 1) it was noted that the difference between the two methods was of the order of 2 dB for each of the first three harmonics of BPF. For Run 367, however, as shown in Figures 32(a) and 32(b) for the fundamental BPF tones of the forward and aft rotors, respectively, the difference is of the order of 5 dB.

Examination of the relevant angles at a radius ratio of 0.75 shows the following:

Case	β(pitch)	β(helicoid)	Delta(β)
Ref. 1, Case 2	36.84	29.13	7.71
Ref. 1, Case 3	41.79	33.12	8.67
Run 367, R1(F)	36.04	22.34	14.06
Run 367, R2(A)	36.05	22.69	13.81

It can be seen from this table that the differences between the helicoidal and pitch angles for the F7A7 model blades as run in the wind tunnel are considerably greater than for the SR–7L propfan in flight on the PTA airplane. It is this increase in the delta (β) that leads to the increased difference in peak BPF tone noise calculated by the two procedures.

The approach used to determine the spanwise lift coefficient distribution on each blade is described in detail in Reference 1. In essence, the total tangential force determined from the input
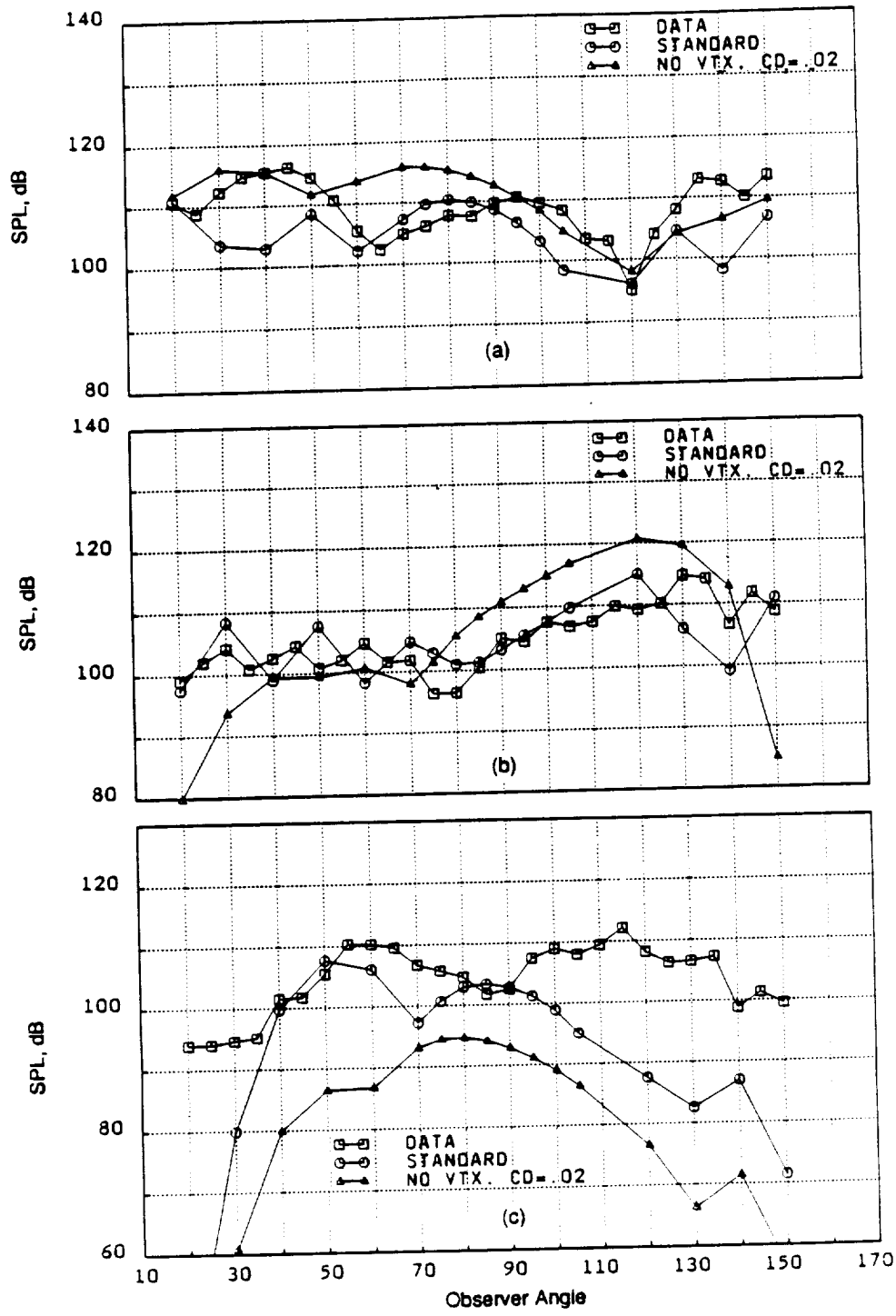
Figure 28. Comparison Between Data Acquired in the NASA Tunnel and Prediction: Acoustic Run 367. F7A7 (11 + 9) Blades. Mach 0.2, 80% RPM_c. (a) 1F + 1A; (b) 1F + 2A; (c) 2F + 1A.

Figure 29. Comparison Between Data Acquired in the NASA Tunnel and Prediction: Acoustic Run 367, F7A7 (11+9) Blades, Mach 0.2, 80% RPM_c. (a) BPF1; (b) BPF2 (c) 1F + 1A; (d) 1F + 2A; (e) 2F + 1A.

Figure 29. Comparison Between Data Acquired in the NASA Tunnel and Prediction: Acoustic Run 367, F7A7 (11 + 9) Blades, Mach 0.2, 80% RPMc. (a) BPF1; (b) BPF2 (c) 1F + 1A; (d) 1F + 2A; (e) 2F + 1A (Concluded)

45
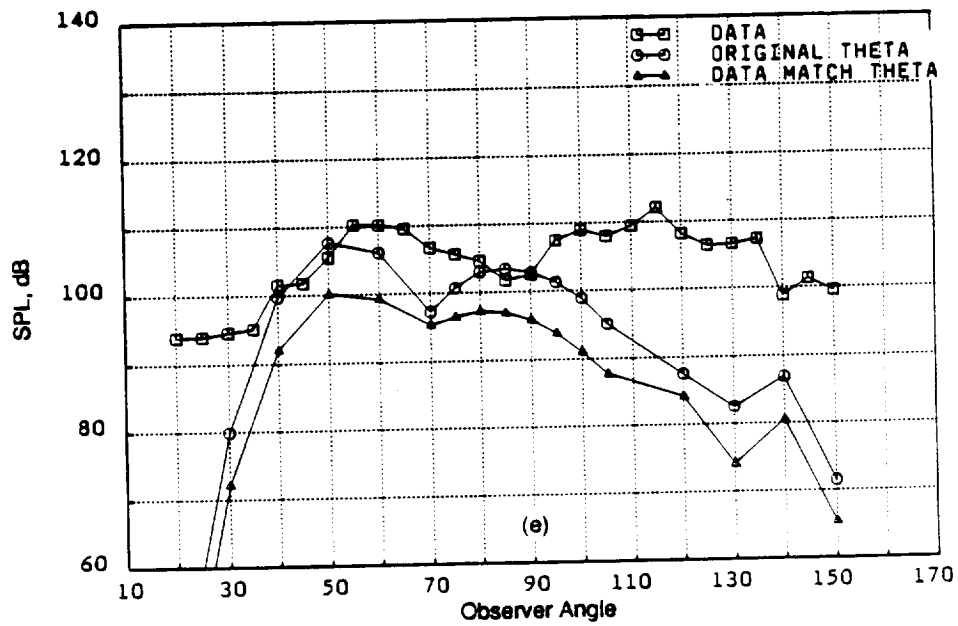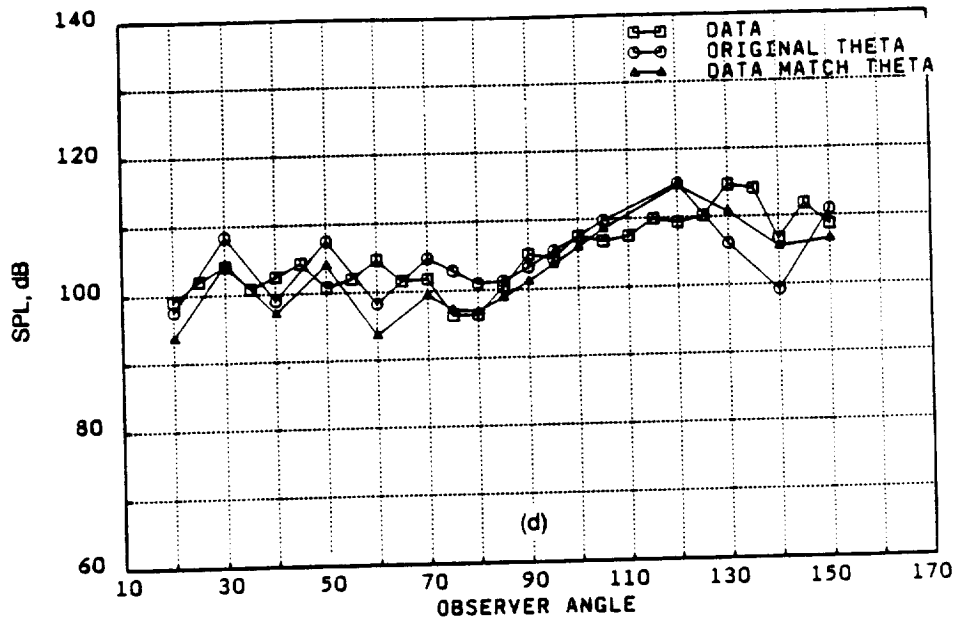
$$\text{Swirl Coefficient } (\theta) = \frac{Cu}{U}$$
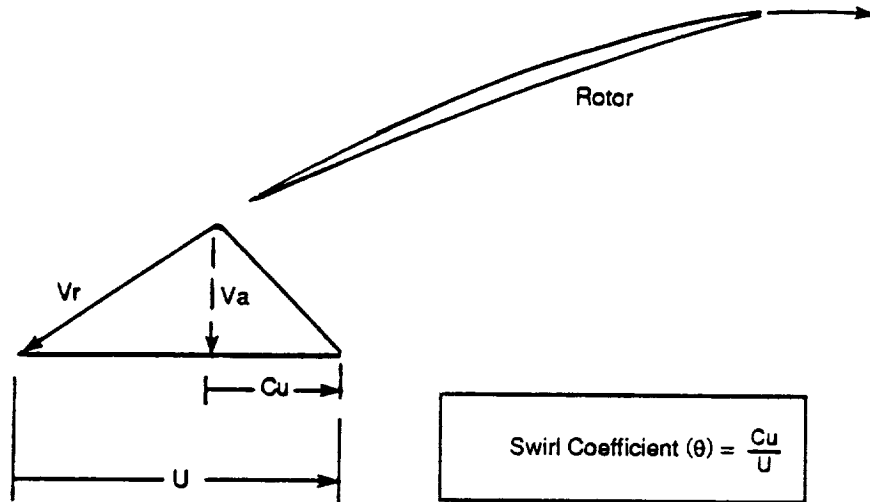
Figure 30. Definition of Swirl Coefficient (Theta).
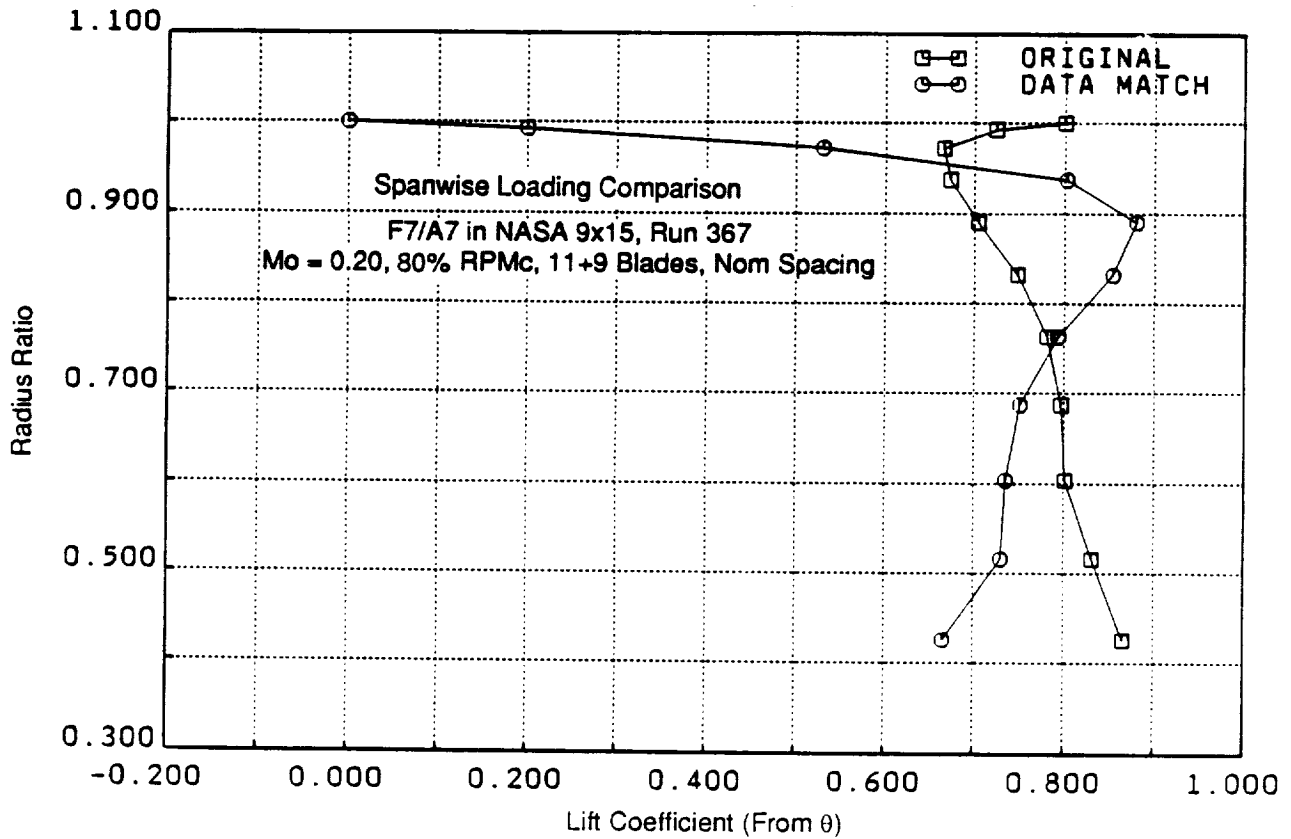
Figure 31. Spanwise Distribution of Lift Coefficients used to Generate Figure 29.
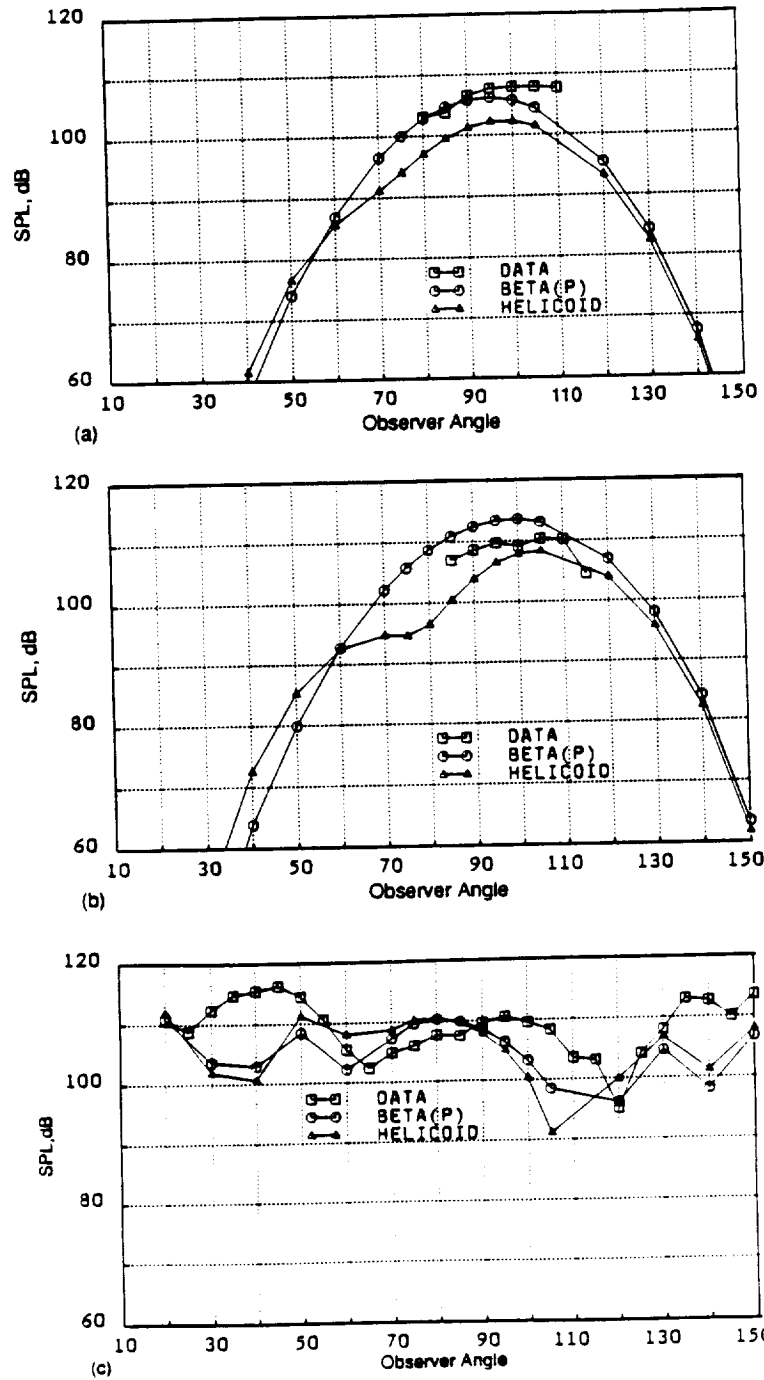
Figure 32. Comparison Between Data Acquired in the NASA Tunnel and Prediction: Acoustic Run 367, F7A7 (11 + 9) Blades, Mach 0.2, 80% RPM$_C$. (a) BPF1; (b) BPF2 (c) 1F + 1A; (d) 1F + 2A; (e) 2F + 1A.
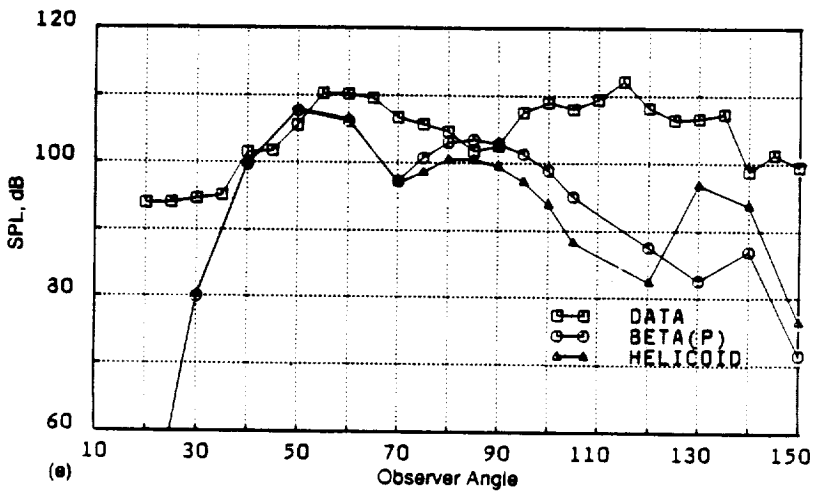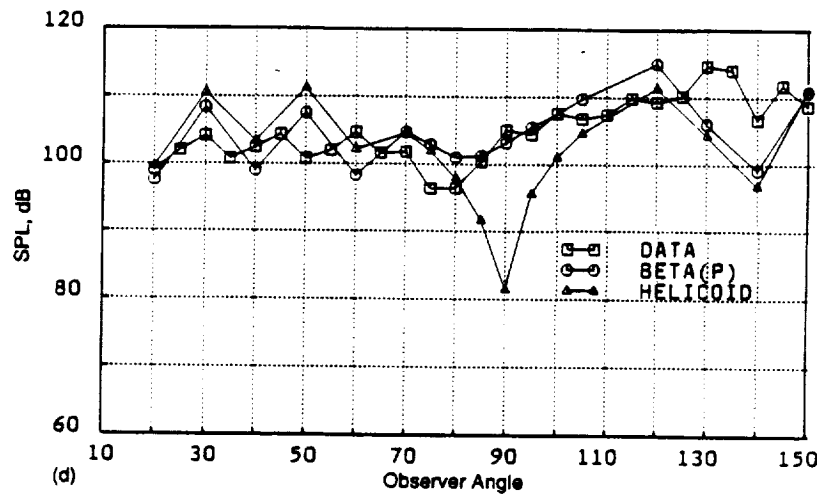
Figure 32. Comparison Between Data Acquired in the NASA Tunnel and Prediction: Acoustic Run 367, F7A7 (11 + 9) Blades, Mach 0.2, 80% RPM_c. (a) BPF1; (b) BPF2 (c) 1F + 1A; (d) 1F + 2A; (e) 2F + 1A (Concluded).

shp and rpm is equated with the tangential component of the local lift force, integrated over the blade span. The local lift force is obtained from an input swirl coefficient distribution, whose amplitude is scaled to match the input quantities. It is assumed, in this portion of the code, that the lift vector is normal to the helicoidal surface swept out by the advancing pitch change axis of the blade. This is sketched in Figure 33, where the helicoidal angle $\beta(H)$ is shown for a representative blade section, together with the pitch angle, $\beta(P)$. The magnitude of the lift vector is L in this sketch, and it is the tangential component labelled Q(H) (resulting from the use of the helicoidal angle) that is integrated spanwise to match the input quantities. The resultant axial force (thust) is denoted by T(H), and, if the IHEL = 1 option is employed in the code, T(H) and Q(H) are the axial and tangential forces that are employed in the acoustic calculation.

As modelled in the computer program, use of the blade pitch angle [$\beta(P)$] to resolve the lift into axial and tangential components results in T(P) and Q(P) of the same figure. The magnitude of the lift vector is the same as before (namely, that calculated using the helicoidal surface angle); it is only its direction that has changed. The geometry sketched in this figure is close to that found near the tip of the blades, and it can be seen that, for the small angles under consideration, the change in tangential component from Q(H) to Q(P) is considerable.

Given that the lift is the same for the two acoustic calculations, the change in the tangential/axial force split can be represented by the ratio of the tangents of the angles $\beta(P)$ and $\beta(H)$. If the 0.75 radius ratio location is taken as representative, converting the ratio of the tangents of the two angles into dB (using $20*Log_{10}$), gives an anticipated difference in predicted peak BPF tone level of approximately 2.6 dB for the SR–7L cases quoted above, and 5 dB for the tones shown in Figures 32(a) and 32(b). These are close to the differences observed.

Comparisons between the use of the blade pitch angle and the helicoidal angle in the Rotor 1/Rotor 2 unsteady loading noise calculation are shown in Figures 32(c) through 32(e). It can be seen that, overall, use of the blade pitch angle gives predictions that are in better agreement with the data, and this trend has been observed in the majority of data/theory comparisons conducted to date. It is appreciated that use of the pitch angle option in the acoustic calculation results in an inconsistency between the aerodynamic and acoustic models. However, based on the agreement with data obtained when using this option it is recommended that calculations made using this code employ the local pitch angle to divide the lift into its thrust and torque components..

2.1.3.2.2. F7A3 Comparisons

As was described in Section 2.1.3.1, the reduced rear diameter A3 blade can be represented in two ways within the computer prediction code. These are shown in the blade planforms of Figure 11, where the "grown" blade is plotted together with the "design" shorter version. Now, in the prediction program, the wake of the forward rotor automatically passes through the tip of the aft rotor, as discussed earlier. In addition, the location of the Rotor 1 tip vortex is referenced to the Rotor 1 tip streamline. Thus, by clipping the aft rotor in the "GROW/CLIP" approach, the effect is to force the tip vortex and wakes shed from the outer portion of the forward blades to miss the aft rotor. The results of this calculation are shown in Figures 34 through 37 labeled "GROW/CLIP". The data shown in this Figure came from Run 512 of the NASA 9x15 foot wind tunnel test. The test point is identical with Run 367 (F7A7) in terms of performance; the only difference lies in the substitution of nine A3 blades for the nine A7 blades used in the earlier test. Also shown in these Figure are three approaches to the use of the design blade geometry in the calculation. For the steady loading BPF
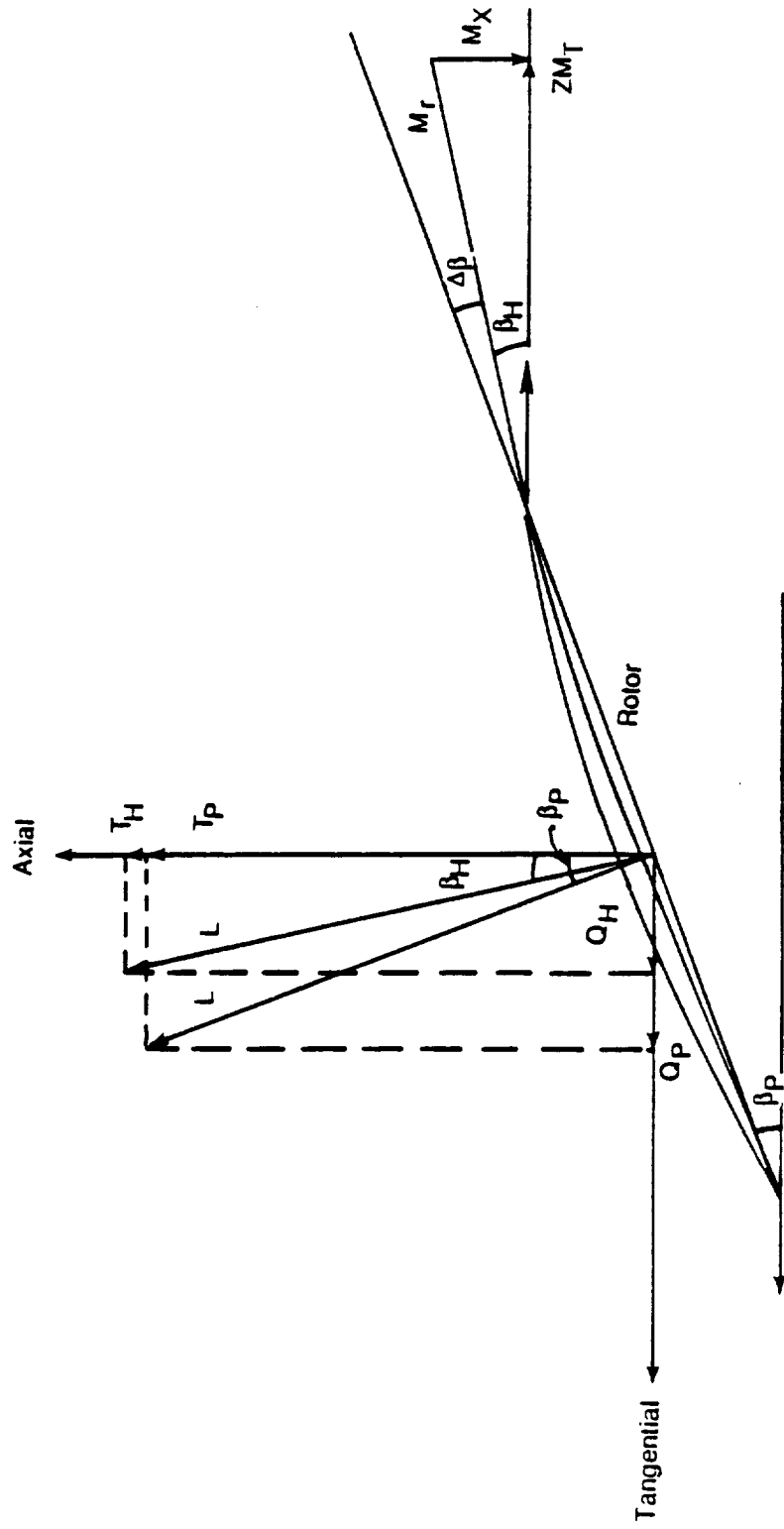
Figure 33. Implication of "Pitch Angle" vs. "Helicoidal Angle" Selection.

50
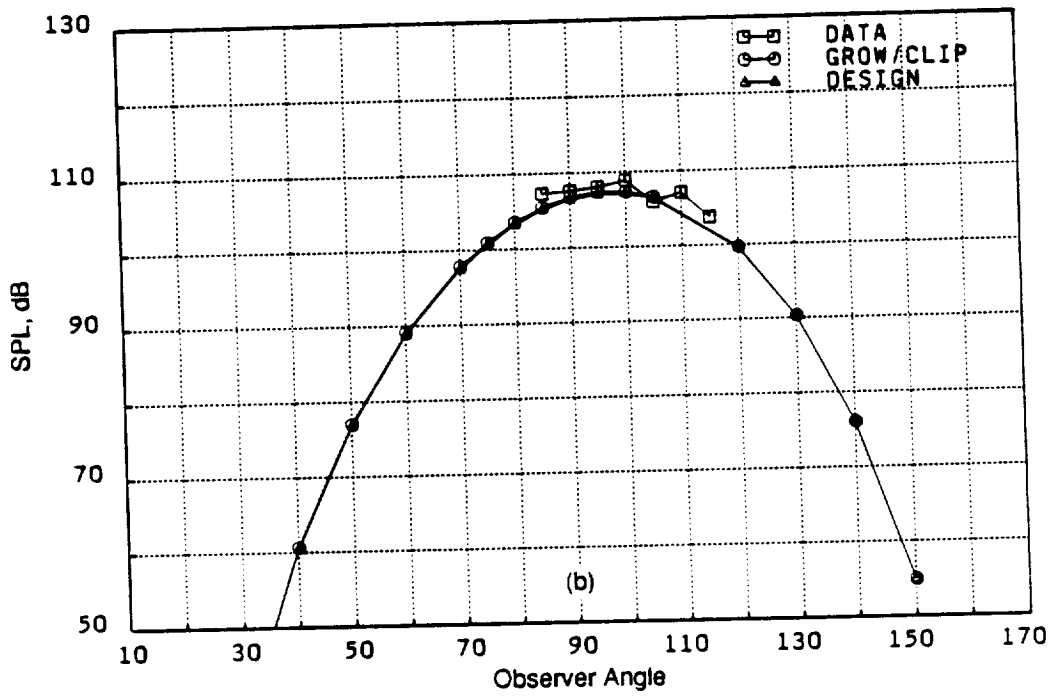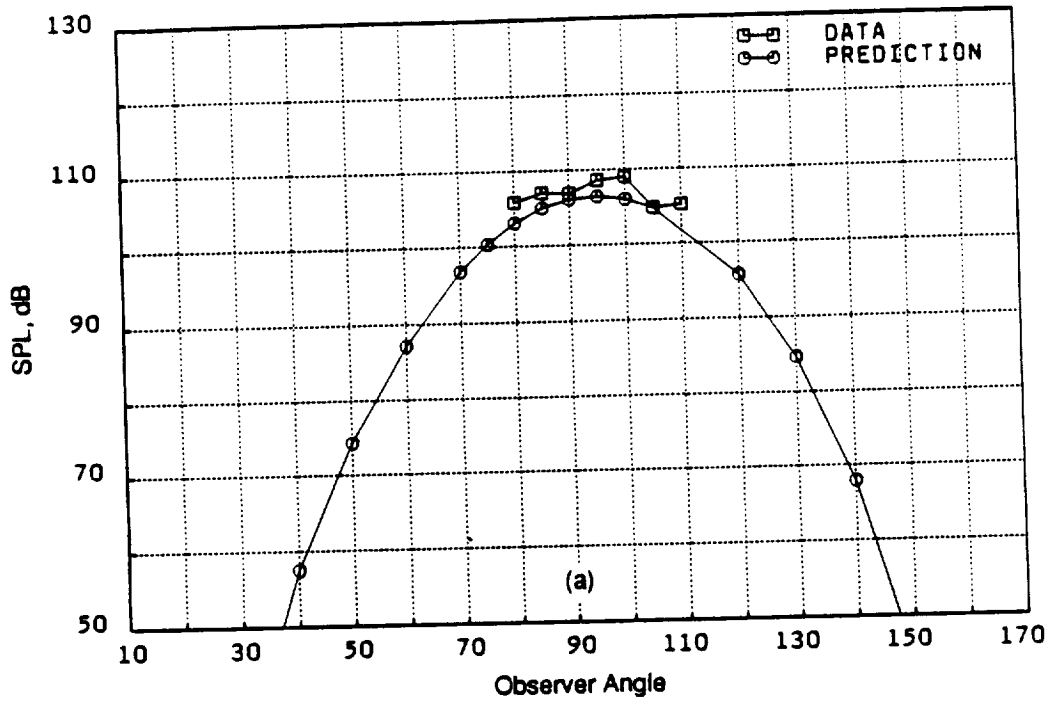
Figure 34. Comparison Between Data Acquired in the NASA Tunnel and Prediction: Acoustic
Run 512, F7A3 (11 + 9) Blades, Mach 0.2, 80% RPM$_c$. (a) BPF1; (b) BPF2.
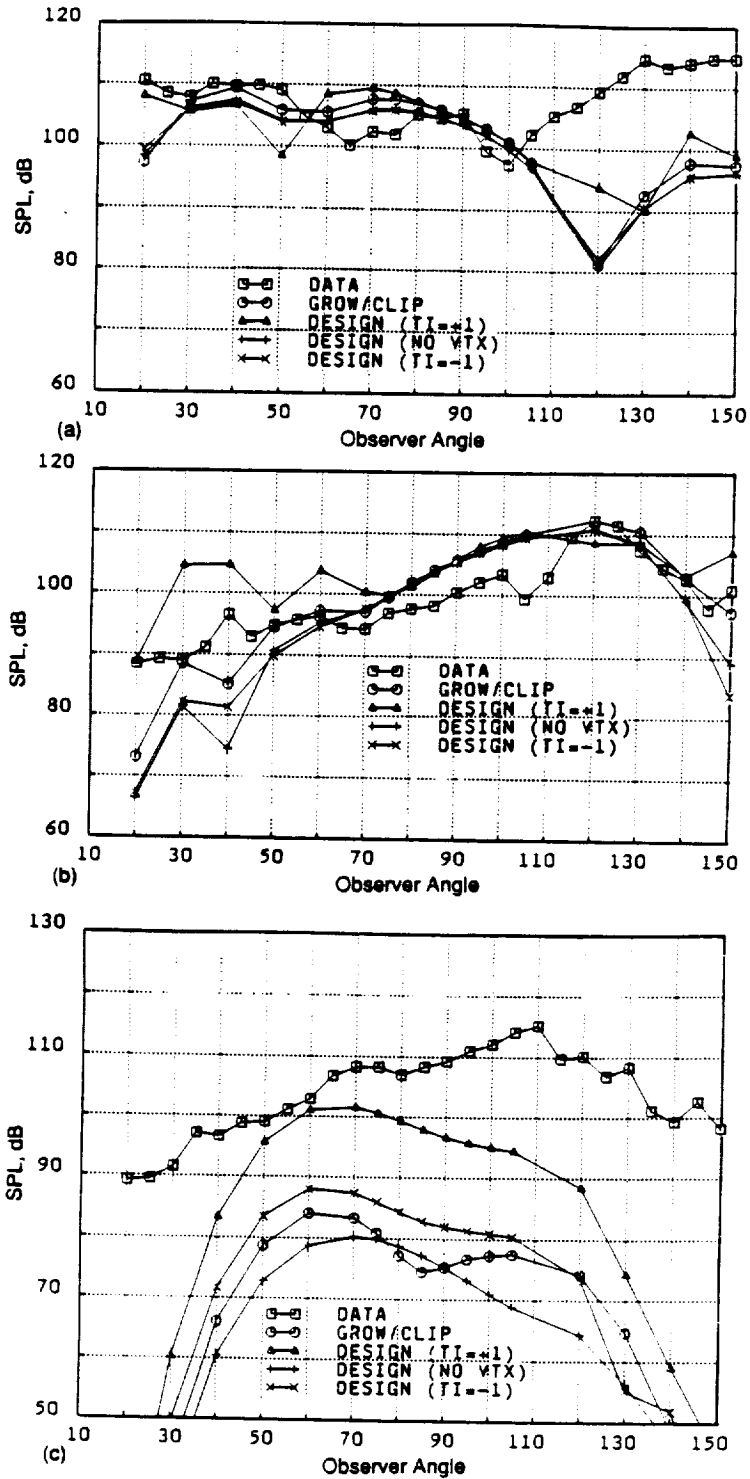
Figure 35. Comparison Between Data Acquired in the NASA Tunnel and Prediction: Acoustic Run 512. F7A3 (11 + 9) Blades, Mach 0.2, 80% RPMc. (a) 1F + 1A; (b) 1F + 2A; (c) 2F + 1A.
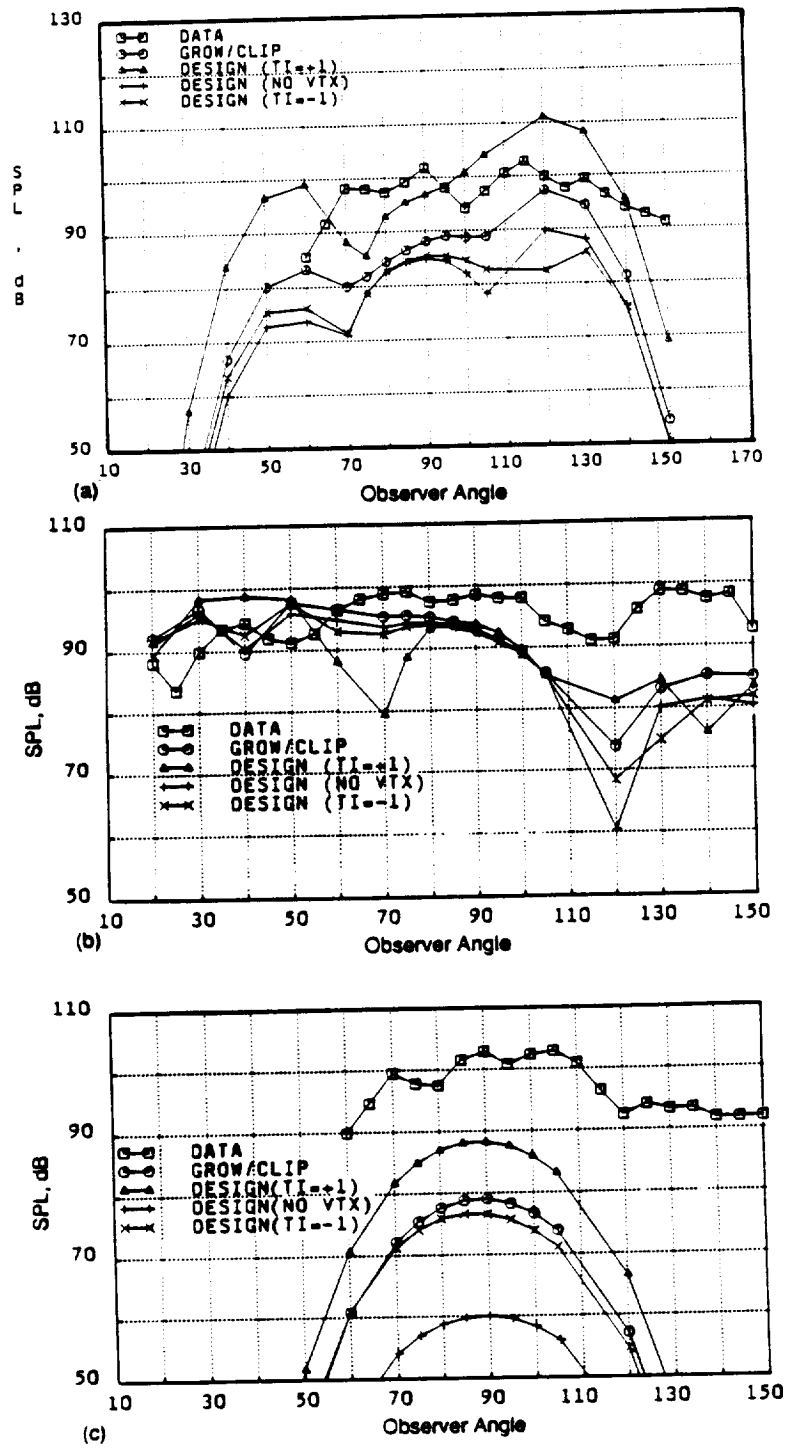
Figure 36. Comparison Between Data Acquired in the NASA Tunnel and Prediction: Acoustic Run 512, F7A3 (11 + 9) Blades, Mach 0.2, 80% RPMc. (a) 1F + 3A; (b) 2F + 2A; (c) 3F + 1A.
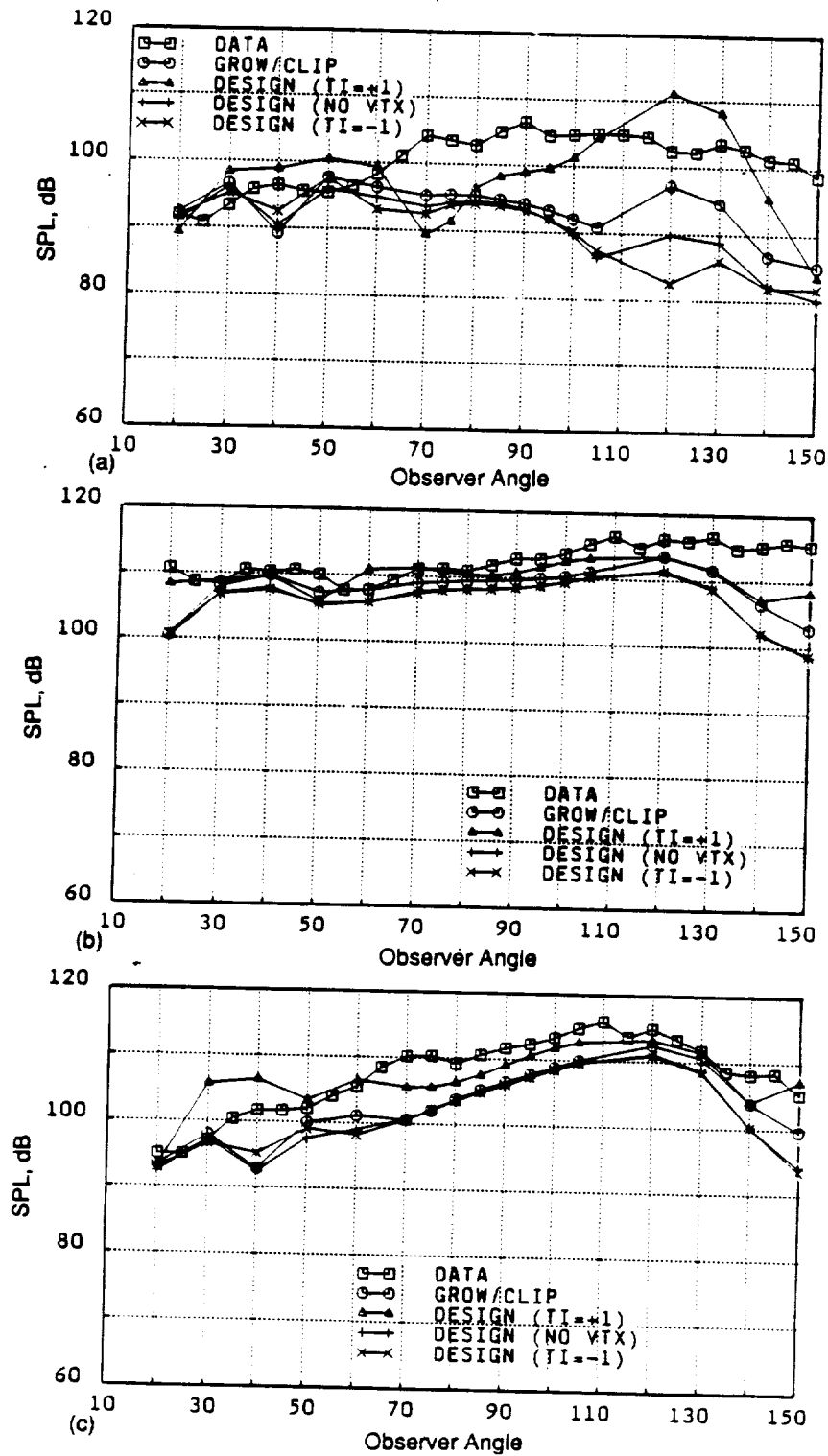
**Figure 37. Comparison Between Data Acquired in the NASA Tunnel and Prediction: Acoustic Run 512, F7A3 (11 + 9) Blades, Mach 0.2, 80% RPM_c.** (a) "4th Harmonic"; (b) Rotor/Rotor Interaction Tone Sum; (c) "3 + 4 + 5 Harmonic" Tone Sum.

tone of the aft rotor these give identical results; the difference between DESIGN and GROW/CLIP here arises from differences in spanwise loading resulting from the two approaches. For the unsteady loading tones, three DESIGN curves are shown. "TI = + 1" implies that the forward rotor tip vortex has been allowed to come inboard of the tip of the aft rotor and is contributing in full to the unsteady flow field experienced by that rotor. The effect of this can be seen in the higher levels predicted for the forward arc region of some of the tones. "NO VTX" means just that – the tip vortex model was not employed in the calculation. Finally, "TI = –1" represents an attempt to simulate the physics of the problem in a more realistic fashion in that, while the Rotor 1 tip streamline also passes through the tip of Rotor 2, carrying its wake defect with it, the tip vortex trajectory carries the vortex core outside the tip of the second rotor, so its effect is reduced.

The results presented in Figures 34 through 37 suggest that, in fact, the best agreement between data and prediction for this reduced diameter rear blade is obtained either by using the "GROW/CLIP" approach or by employing the full tip vortex model. This case serves to illustrate the need to understand the flowfield perceived by the aft rotor before, perhaps, examining in greater detail the unsteady response of that rotor to it. It is worth noting that, in all cases, the predicted benefits from use of a reduced diameter rear rotor were greater than those measured, suggesting there is room for improvement in the model.

2.1.3.2.3. F11A11 Comparisons

The F11A11 blades shown in Figure 18 were designed to operate at Mach 0.8 in a 11–forward plus 9–aft configuration. Low speed testing was carried out in the GEAE Cell 41 anechoic facility (Figure 17), and it is Run 4006 of this series that was selected for the comparisons shown in Figures 38 through 41. The blade geometry and design operating conditions are felt to be sufficiently different from those of the F7A7 and F7A3 designs discussed earlier that to obtain good data/theory comparisons for these blades, together with those already demonstrated, should provide verification for the model delivered under this contract.

The use of static microphones in Cell 41 means that there are not as many data points available over the observer angle range shown in Figures 38 through 41, as is the case for the traverse data shown earlier. However, Figure 38 demonstrates excellent agreement between the available data and the prediction model for the fundamental BPF tone of the forward rotor, with the agreement for the aft rotor BPF almost as good. In Figures 39 through 41, the same series of rotor/rotor interaction tones that was considered earlier for the F7A7 and F7A3 blades is shown for this F11A11 case. The absence of microphone data in the region forward of an observer angle of 67.5° is unfortunate, but the agreement between data and prediction shown in these figures is equivalent to that obtained for the earlier blade designs. It is worth noting here that while the blade numbers and percent corrected RPM were the same for the F11A11, F7A7, and F7A3 test points considered, the F11A11 data discussed above were taken in a free jet Mach No. of 0.25, rather than the 0.2 wind tunnel Mach No., and also, the thrust generated by the blading was approximately 1.2 times that of the F7A7 case con-sidered, leading to higher blade loadings and different wake characteristics. The overall agreement obtained between measured data and predicted results for these different blade designs and operating conditions demonstrates the general validity of the model.

2.1.4 Conclusions

The GE Aircraft Engines isolated counterrotation high speed turboprop noise prediction pro-gram has been compared with data gathered in four facilities under both cruise and low flight speed
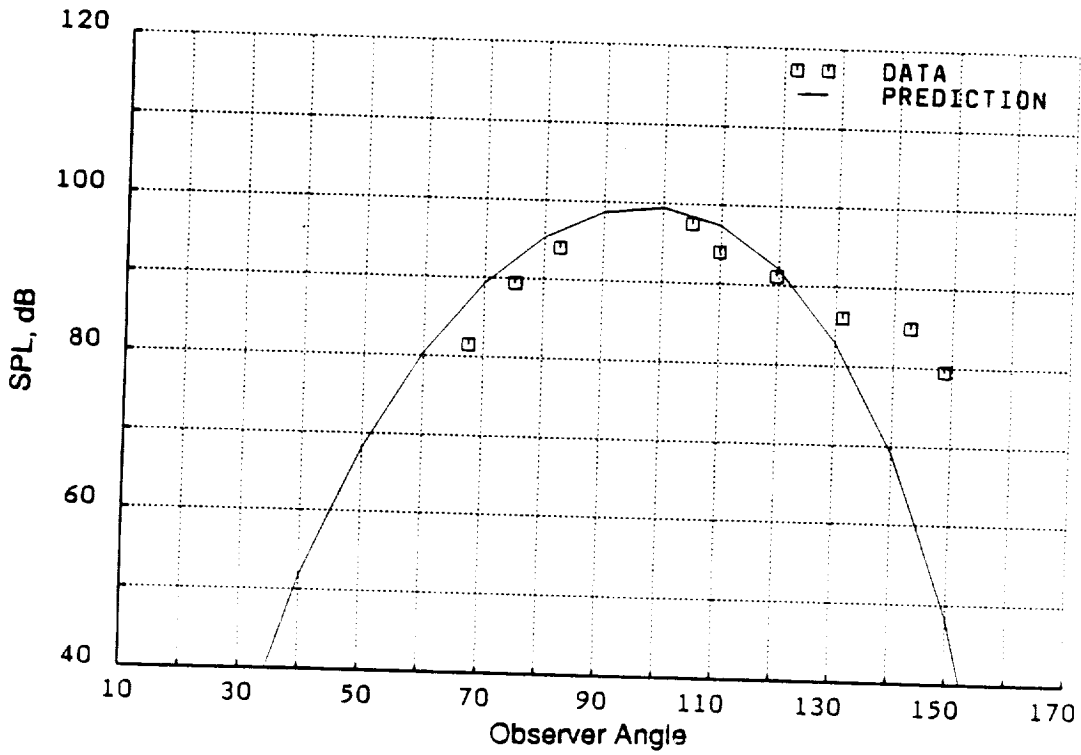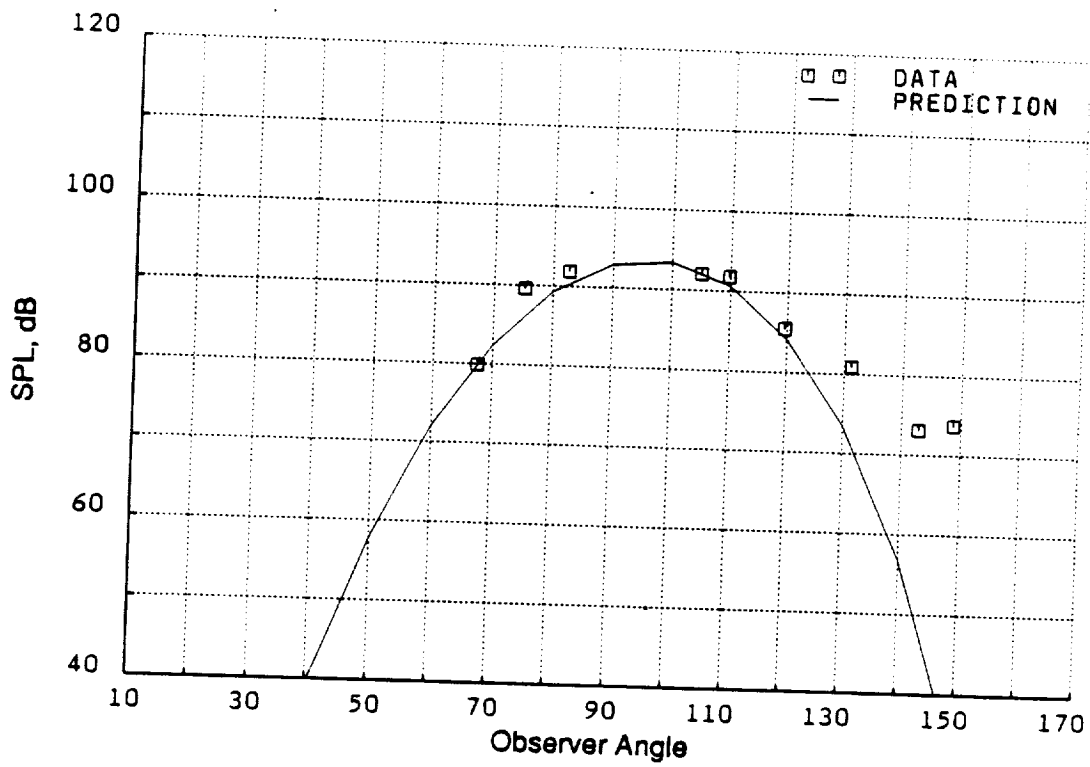
Figure 38. Comparison Between Data Acquired in the GE Aircraft Engines Cell 41 Free Jet Anechoic Facility and Prediction: Test Point 4006, F11A11 (11 + 9) Blades, Mach 0.25 80% RPM$_c$. (a) BPF 1; (b) BPF 2.
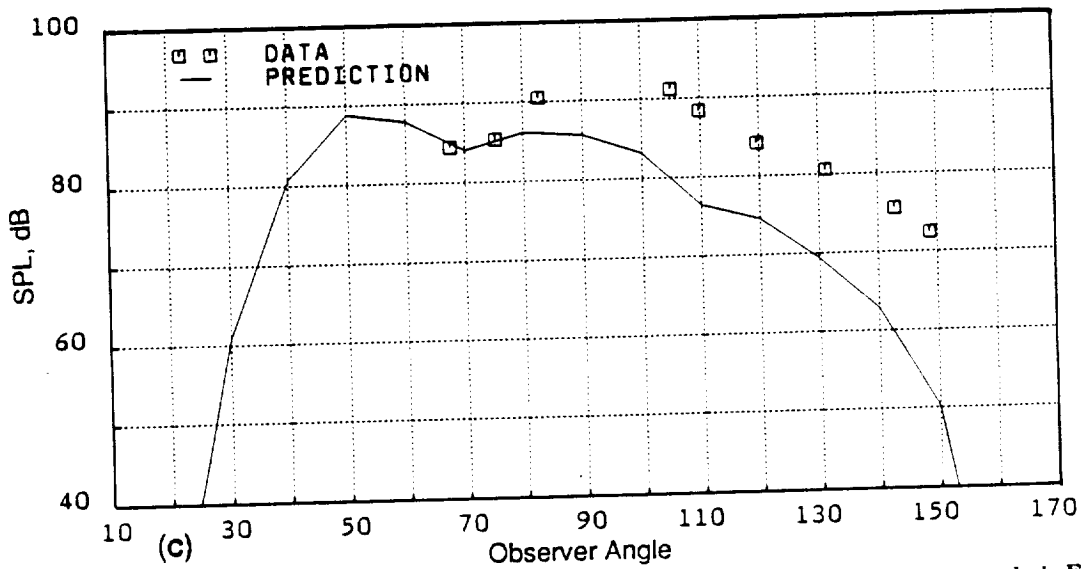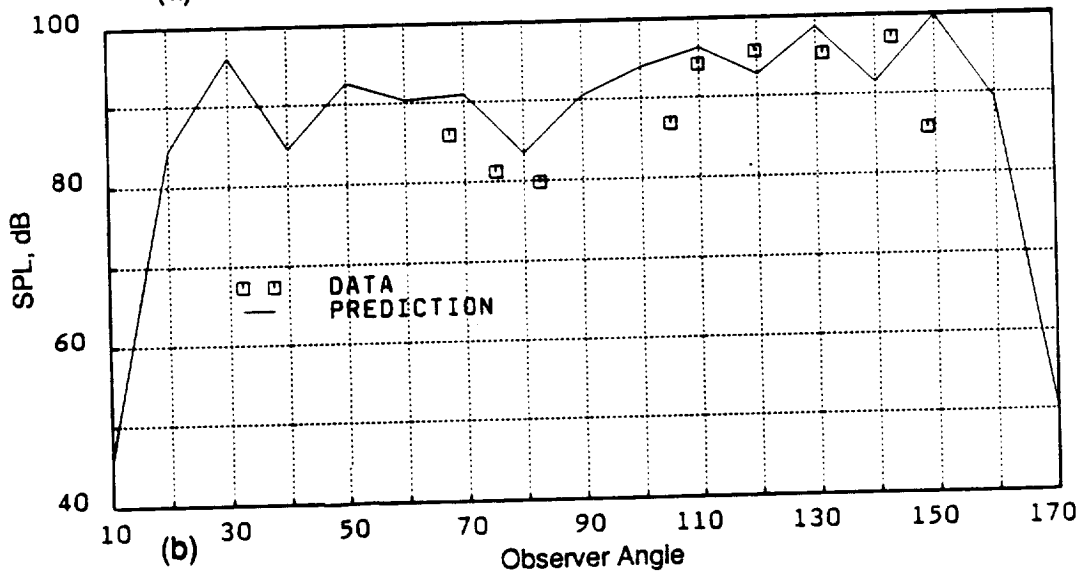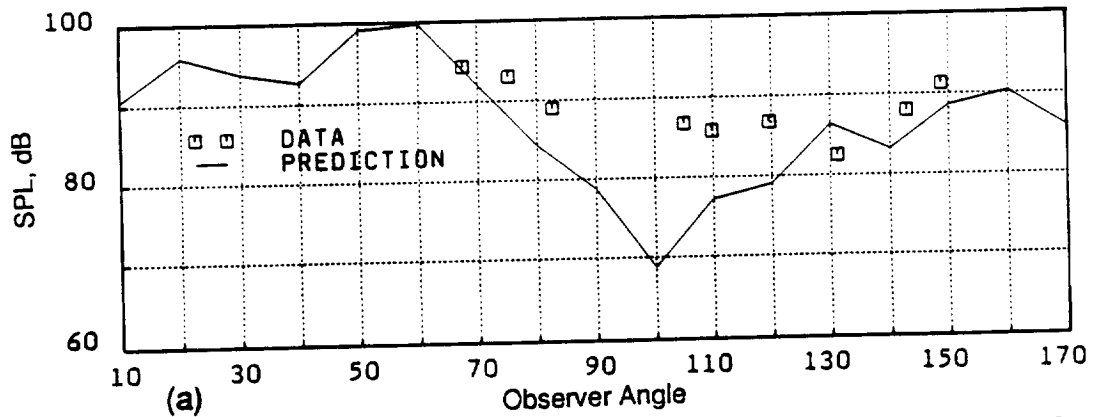
Figure 39. Comparison Between Data Acquired in the GE Aircraft Engines Cell 41 Free Jet Anechoic Facility and Prediction: Test Point 4006, F11A11 (11 + 9) Blades, Mach 0.25 80% RPMc. (a) 1F + 1A; (b) 1F + 2A; (c) 2F + 1A.
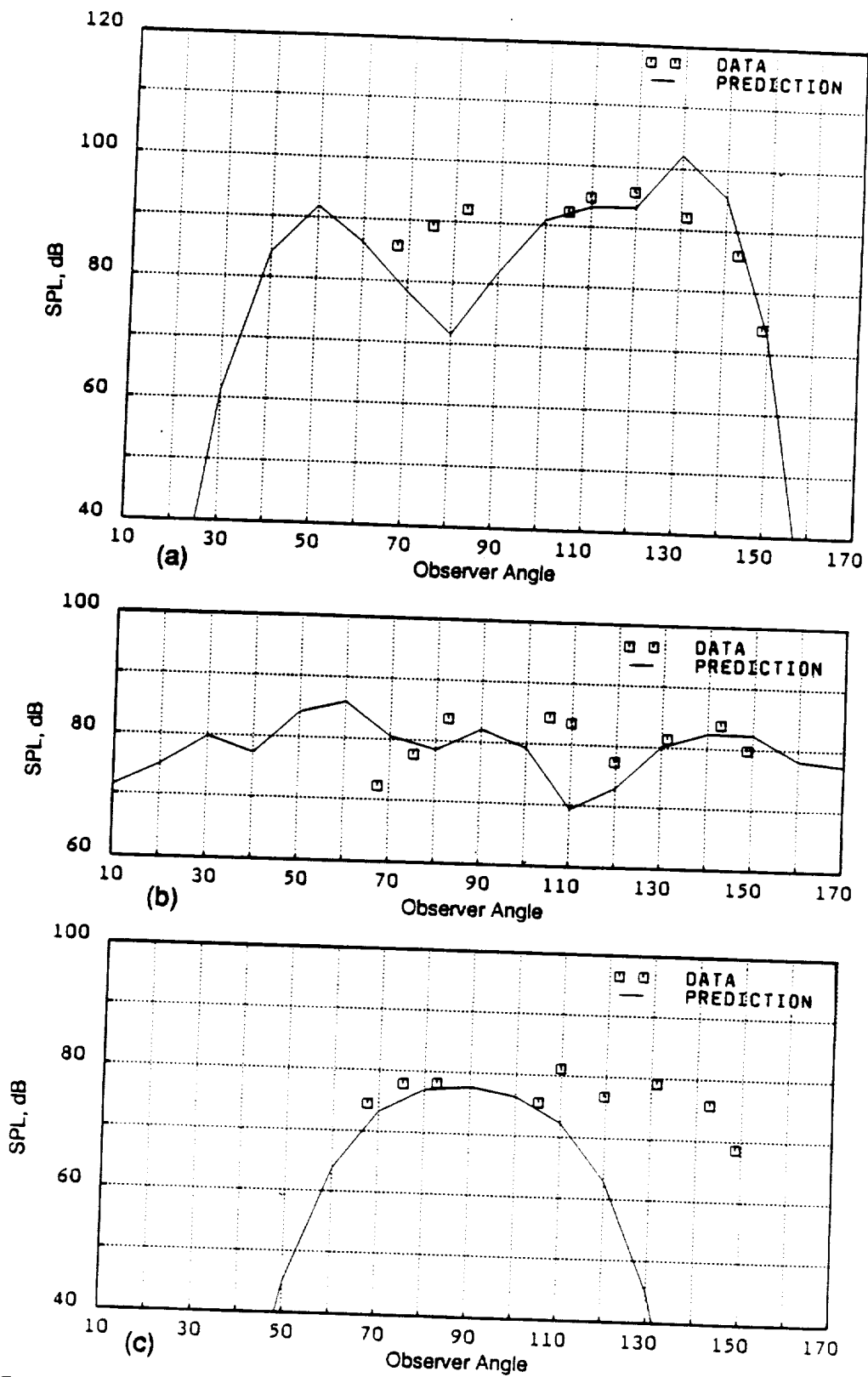
Figure 40. Comparison Between Data Acquired in the GE Aircraft Engines Cell 41 Free Jet Anechoic Facility and Prediction: Test Point 4006, F11A11 (11+9) Blades, Mach 0.25 80% RPM$_c$. (a) 1F + 3A; (b) 2F + 2A; (c) 3F + 1A.

58
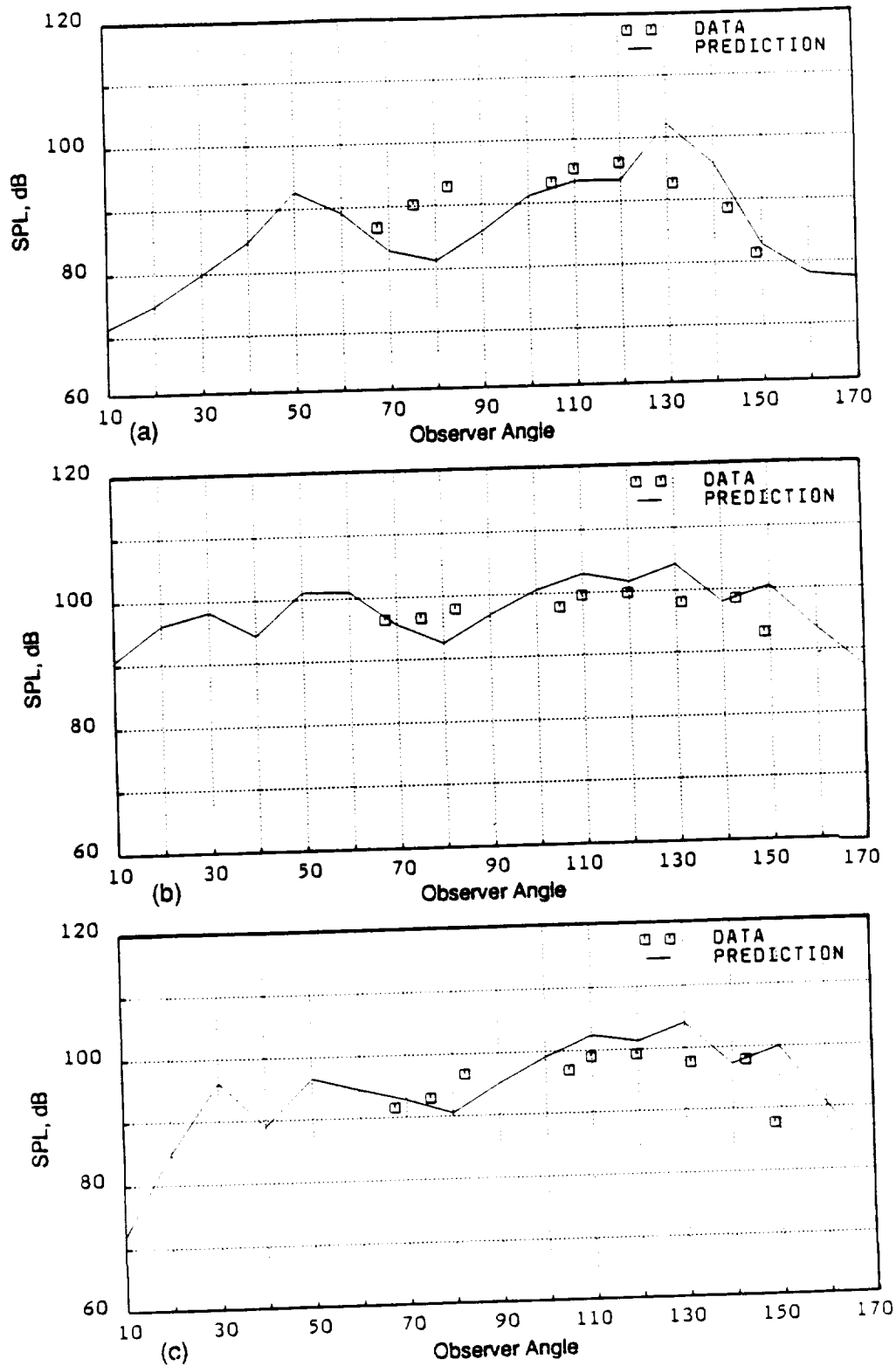
Figure 41. Comparison Between Data Acquired in the GE Aircraft Engines Cell 41 Free Jet Anechoic Facility and Prediction: Test Point 4006, F11A11 (11 + 9) Blades, Mach 0.25 80% RPM_c. (a) "4th Harmonic"; (b) Rotor/Rotor Interaction Tone Sum; (c) "3 + 4 + 5 Harmonic" Tone Sum.

simulated conditions. Five different blade design combinations have been examined, including an example of the reduced diameter aft rotor concept. The results show, in general, good agreement between data and prediction, with some areas still requiring clarification. This study has demonstrated the overall validity of the modeling employed in the computer code while identifying regions for future refinement of the prediction methodology.

2.2 Installation Effects on Counterrotating Propeller (CRP) Noise

2.2.1 Introduction

The purpose of this study was to extend the results of Reference 1 (wherein installation effects on single–rotation propeller (SRP) noise were evaluated) to the counterrotating case (CRP). In both this study and in the prior study only the effects on blade passing frequency (BPF) noise (and its harmonics) were considered. In the current work, the effects of the installation environment on the BPF noise of both front and rear rotors have been considered.

The scope of the current work encompassed:

- Steady state aerodynamics of a CRP
- Quasi steady theory for CRP
- Velocity fields caused by "installation" effects (including the effect of an upstream mounting pylon)
- Acoustic theory
- Theory data comparisons.

2.2.2. Steady State Aerodynamics of a CRP

In this section, the extension of the single–rotation propeller theory to predict axial and tangential force coefficients (given lift/drag relations for each radial section as functions of angle of attack) to the CRP case is outlined. The key element is Figure 42 giving the velocity triangles for the CRP case at radius "r".

Notation for Figure 42:

a: Axial interference factor

a′: Tangential interference factor

c: Slipstream contraction factor

k: Prandtl tip loss or tangential average factor

r: Radius of analysis

U: Forward flight speed

Ω: Angular velocity of rotor, radians/second

ϕ: Angle of flow relative to blade from tangential

Subscripts

F: Front rotor

R: Rear rotor

60

$U[1 + a_F + k_R a_R c_R]$

$r\Omega_F (1 - a'_F)$

ϕ_F

FRONT

$U(1 + a_R + k_F a_F c_F)$

ϕ_R

$\Omega_R r[1 - a'_R + 2k_c a'_F \Omega_F / \Omega_R]$

REAR
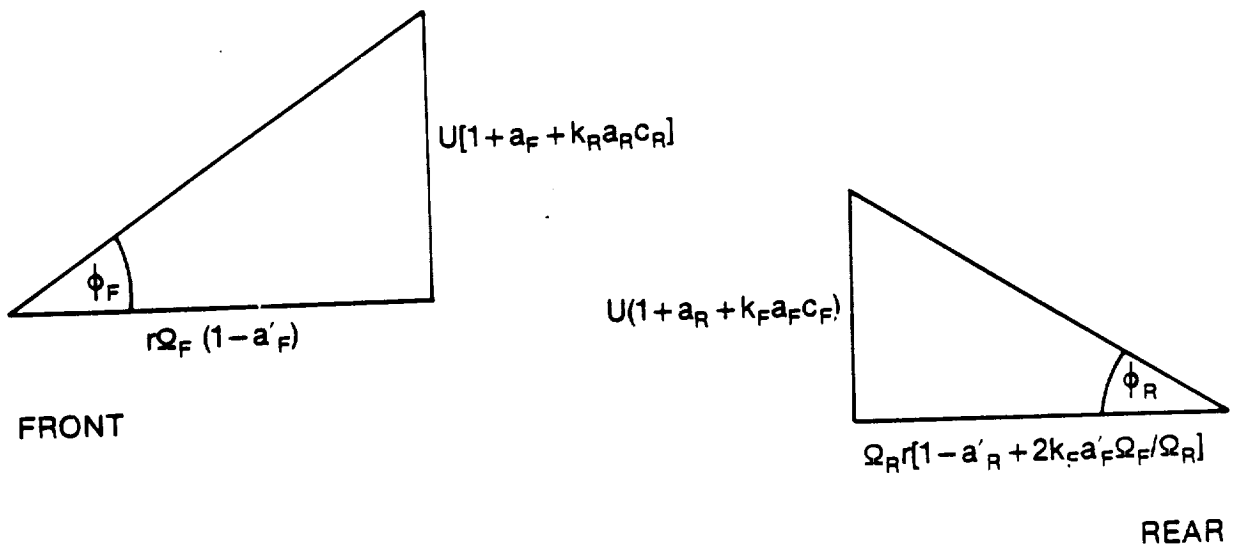
Figure 42. CRP Velocity Triangles at Radius "r".

Some remarks concerning the axial and tangential interference factors of Figure 1 are in order. Consider first the axial interference factor. In terms of the effect of one rotor on the adjacent rotor the axial interference factor is modified first by the tangential average or Prandtl tip loss factor because each rotor blade of one rotor experiences only the tangential average effect of the adjacent rotor, which is moving relative to the chosen rotor blade. Second the effect of the slipstream contraction needs to be accounted for. The slipstream contraction factor is taken in this study as:

$$c = 1 \pm \frac{x}{\sqrt{x^2 + r^2}}$$

where x is the axial separation between the planes of the two rotor actuator disks. The plus sign is applicable when the influence of one rotor on the downstream rotor is evaluated and the minus sign when the influence of a rotor on the upstream rotor is evaluated.

Now consider the tangential interference factor. First the downstream rotor exerts no tangential interference on the upstream rotor. Second (except for the Prandtl tip loss or tangential averaging factor) the upstream rotor exerts twice the tangential interference on the downstream rotor as it does on itself since the turning through a rotor is fully complete aft of the rotor.

The procedure for computing the steady axial and tangential force coefficients is as follows. Assume initial guesses for ϕ_F, ϕ_R. Determine angles of attack from known blade orientation at the appropriate radius and determine lift/drag coefficients C_L, C_D. Obtain C_x, C_y (nondimensional force coefficients in direction of rotor rotation and thrust direction) via:

$$C_y = C_L \cos \phi - C_D \sin \phi$$

$$C_x = C_L \sin \phi + C_D \cos \phi$$

Then by arguments similar to the SRP case, we can solve for "a'_F" via:

$$\frac{a'F}{(1-a'F)} = \frac{C_{xF}\sigma_F}{4\cos\phi_F \sin\phi_F k_F}$$

where "σ_F" denotes the solidity of the front rotor.

Likewise, application of the tangential momentum equation for the aft rotor yields an equation for calculating "a'_R" via:

$$\frac{a'R}{1-a'_R + 2k_F a'_F \Omega_F} = \frac{C_{xR}\sigma_R}{4\cos\phi_R \sin\phi_R k_R}$$

Application of the axial momentum equation to the forward rotor yields an equation for calculation of "a_F".

$$a_F = \frac{(1-a'F)}{k_F}\left(\frac{r}{R}\right)\left(\frac{C_{yF}}{4\lambda_F}\right)\left(\frac{\sigma_F}{\sin\phi_F \cos\phi_F}\right)$$

("λ_F" is the advance ratio of the forward rotor). Lastly, the axial momentum equation for the aft rotor yields an equation for "a_R" as:

$$a_R = \frac{(1 + 2k_F a'_F (\Omega_F/\Omega_R) - a'_R}{k_R}\left(\frac{r}{R}\right)\left(\frac{C_{yR}}{4\lambda_R}\right)\left(\frac{\sigma_R}{\sin\phi_R \cos\phi_R}\right)$$

As indicated above, the quantities a'_F, a'_R, a_F, and a_R have been obtained in terms of ϕ_F and ϕ_R. The two equations needed to close the system are:

$$\lambda_F = \tan(\phi_F)\left(\frac{r}{R}\right)\frac{(1-a'_F)}{(1 + a_F + k_R a_R c_R)}$$

and:

$$\lambda_R = \tan(\phi_R)\left(\frac{r}{R}\right)\frac{(1-a'_R + 2k_F a'_F \Omega_F/\Omega_R)}{(1 + a_R + k_F a_F c_F)}$$

The above completes the procedure to solve the steady–state aerodynamic problem for the CRP in a manner similar to that of the SRP.

2.2.3 Quasi–steady theory for CRP

In this section, the extension of the quasi–steady theory for the counterrotation case to obtain the unsteady forces (in the quasi–steady approximation) is outlined. The notation employed is as follows (some notation from Section 2.2.2 is repeated for convenience):

C_F, C_R: Constants of proportionality associated with front and rear rotors at a given radius, r

r: Local radius of analysis

R: Propeller tip radius

U: Forward flight speed

u: Perturbation axial velocity component "far upstream of rotors" (positive downstream)

v: Perturbation tangential velocity "far upstream of rotors" (positive corresponds to "v" in same sense as direction of rotation of forward rotor).

Ω_F, Ω_R: Speeds of rotation of forward and rear rotor

λ: Advance ratio based on front rotor, i.e., $\lambda = U/(R\,\Omega_F)$. (Note the use of λ rather than J, where $J = \pi\lambda$)

S: Rotor speed ratio, i.e., $S = \Omega_F/\Omega_R$

Now, in general, the extension of the steady single rotation propeller theory to the counter rotation case will yield for quantities (Q_F) associated with the front rotor a functional relation of type:

$$Q_F = C_F\Omega_F^2 f_F\ (\lambda, S)$$

where "C_F" is a suitable constant of proportionality at a given radius and Q_F can represent a quasi–steady force. Likewise, for quantities (Q_R) associated with the rear rotor we may write:

$$Q_R = C_R\Omega_R^2 f_R\ (\lambda, S)$$

We now wish to compute the variation δQ_F, δQ_R, due to the extra (u,v) velocity field "far upstream." We note the following intermediate relations:

$$\delta\Omega_F = -v/r, \delta\Omega_R = v/r$$

$$\delta\lambda = \lambda[u/U + v/(r\Omega_F)]$$

$$\delta S = -S[v/(r\Omega_F) + v/(r\Omega_R)]$$

$$= -S\ (1+S)\ v/(r\Omega_F)$$

$$= -S\ (1+S)\ \lambda\left(\frac{R}{r}\right)(v/U)$$

Thus:

$$\delta Q_F = C_F\left[2\Omega_F\delta\Omega_F f_F + \Omega_F^2\left(\frac{\partial f_F}{\partial\lambda}\right)\delta\lambda + \Omega_F^2\left(\frac{\partial f_F}{\partial S}\right)\delta S\right]$$

$$= C_F\Omega_F^2\left[\lambda\left(\frac{\partial f_F}{\partial\lambda}\right)\left(\frac{u}{U}\right) + \left[-2\,\lambda\left(\frac{R}{r}\right)f_F + \lambda^2\left(\frac{R}{r}\right)\left(\frac{\partial f_F}{\partial\lambda}\right) - S\,(1+S)\,\lambda\left(\frac{R}{r}\right)\left(\frac{\partial f_F}{\partial S}\right)\right]\left(\frac{v}{U}\right)\right]$$

Likewise:

$$\delta Q_R = C_R\left[2\,\Omega_R\,\delta\Omega_R\,f_R + \Omega_R^2\left(\frac{\partial f_R}{\partial\lambda}\right)\delta\lambda + \Omega_R^2\left(\frac{\partial f_R}{\partial S}\right)\delta S\right]$$

$$= C_R\Omega_R^2\left[\lambda\left(\frac{\partial f_R}{\partial\lambda}\right)\left(\frac{u}{U}\right) + \left[2\,\lambda\,S\left(\frac{R}{r}\right)f_R + \lambda^2\left(\frac{R}{r}\right)\left(\frac{\partial f_R}{\partial\lambda}\right) - S\,(1+S)\,\lambda\left(\frac{R}{r}\right)\left(\frac{\partial f_R}{\partial S}\right)\right]\left(\frac{v}{U}\right)\right]$$

These are the relations that are used to determine the fluctuation quantities in the quasi–steady approximation for the counterrotation case. Note that partial derivatives with respect to both "λ" and "S" (advance ratio and speed ratio) are now required. These are evaluated by examining steady

solutions for the following five pairs of points in the (λ, S) space:

$$(\lambda, S), (\lambda+0.01, S), (\lambda-0.01, S), (\lambda, S+0.01), \text{ and } (\lambda, S-0.01)$$

2.2.4. Velocity Fields due to "Installation" Effects – Effect of Pylon

The velocity fields due to the angle–of–attack effect, fuselage, and horseshoe vortex system associated with the wing were described in Reference 1. However, the effect of the pylon needs discussion.

In the current work, the pylon (apart from its geometry) is assumed to be characterized for fluid mechanical purposes by three quantities:

- Drag coefficient, C_{Dp}

- Camber of the pylon

- Angle of attack experienced by pylon

The pylon is then assumed to operate at a location upstream of the CRP where it experiences an axial velocity:

$$U(1 + k_F a_F C_{Fp} + k_R a_R C_{Rp})$$

where the additional terms "C_{Fp}, C_{Rp}" represent the slipstream contraction factors of the front and rear rotors at the location of the pylon.

Based on this "freestream" flow velocity field, the total distortion components u_p, v_p (axial and tangential) due to both lift and drag of the pylon at the leading edge plane of the CRP are calculated. The lift related components are calculated from potential flow theory whereas the drag components are computed from the usual semiempirical representations relating the wake velocity defect to the drag coefficient.

However, knowledge of the distortion components u_p, v_p at the leading edge plane of the rotor is not directly convenient for unsteady force/noise calculations which are based on distortion components "far upstream" of the CRP. To circumvent this difficulty the following procedure is adopted.

Consider that the distortion velocity components at the leading edge plane (u_p, v_p) are induced by virtual components "far upstream" labelled as $(u_{p\infty}, v_{p\infty})$. By the quasi–steady theory outlined previously, we can write that:

$$u_p = a\, u_{p\infty} + b v_{p\infty}$$

and

$$v_p = v_{p\infty}$$

The quantities "a", "b" can be related to propeller aerodynamic quantities and their partial derivatives with respect to advance ratio and speed ratio.

Now in the present case (of the pylon induced distortion) we know u_p, v_p. Then knowing "a", "b", we calculate the virtual components ($u_{p\infty}$, $v_{p\infty}$) far upstream by the relations:

$$v_{p\infty} = v_p$$

$$u_{p\infty} = (u_p - bv_p)/a$$

The virtual components ($u_{p\infty}$, $v_{p\infty}$) can now be added to "far upstream" velocity distortions due to angle of attack, aircraft wing induced flowfield, and fuselage induced flow.

We now address briefly an issue concerning the viscous wakes shed from the pylon. Since these wake regions are thin, it is preferable to have an explicit formula for the Fourier components of the wake rather than rely on numerical integration. The wake velocity defect function (for $0 \le \theta \le 2\pi$ with θ denoting an azimuthal angle) typically has a form:

$$f(\theta) = 0 \text{ for } \theta \ge (\theta_o + \alpha) \text{ or } \theta \le (\theta_o - \alpha)$$

where "2α" is the wake width and "θ_o" is the center of the wake, and for $(\theta_o - \alpha) \le \theta \le (\theta_o + \alpha)$:

$$f(\theta) = \cos^2\left(\frac{\pi(\theta - \theta_o)}{2\alpha}\right)$$

We wish to determine the Fourier coefficients of $f(\theta)$; i.e., represent it as:

$$f(\theta) = a_o + \sum_1^\infty (a_n \cos(n\theta) + b_n \sin(n\theta))$$

It can be shown that:

$$a_o = \alpha/2\pi$$

$$(a_n, b_n) = (\cos(n\theta_o), \sin(n\theta_o)) * \frac{\sin(\alpha n)}{\pi}\left[\frac{1}{n} + \frac{\alpha^2 n}{(\pi^2 - \alpha^2 n^2)}\right]$$

If some "n" = "m", "αn" = π then the corresponding coefficients are:

$$(a_m, b_m) = \frac{\alpha}{2\pi}(\cos(m\theta_o), \sin(m\theta_o))$$

Similarly an explicit expression for the Fourier components of velocity associated with the circulation (potential flow) of the pylon is obtained. The conditions at a radius "a" are calculated (see Figure 43)

The stream function Ψ satisfies:

$$\frac{\partial^2\psi}{\partial x^2} + \frac{1}{a^2}\frac{\partial^2\psi}{\partial\theta^2} = \frac{\Gamma}{a}\delta(x)\delta(\theta - \theta_o) \dots$$

The right hand side can be written as:

$$\frac{\Gamma\delta(x)}{2\pi a}\left\{1 + 2\sum_1^\infty [\cos(n\theta)\cos(n\theta_o) + \sin(n\theta)\sin(n\theta_o)]\right\}$$

65
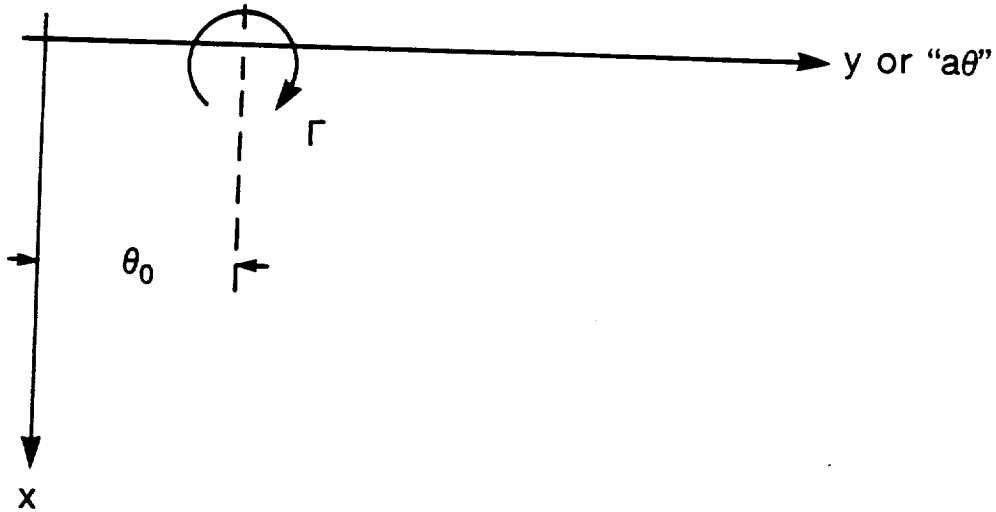
Figure 43. Calculation of Potential Flow Fields Due to Pylon Bound Circulation.

Consider the components of the above for $n \geq 1$.

$$\psi_n = \frac{-\Gamma}{2\pi n} \exp\left(\frac{-n|x|}{a}\right) (\cos(n\theta)\cos(n\theta_o) + \sin(n\theta)\sin(n\theta_o))$$

So that with $u_n = \dfrac{\partial \psi_n}{a\partial\theta}$, $v_n = \dfrac{-\partial\psi_n}{\partial x}$:

$$u_n = \frac{\Gamma}{2\pi a} \exp\left(\frac{-n|x|}{a}\right)(-\cos(n\theta)\sin(n\theta_o) + \sin(n\theta)\cos(n\theta_o))$$

$$v_n = \frac{-\Gamma \text{sgn}(x)}{2\pi a} \exp\left(\frac{-n|x|}{a}\right) (\cos(n\theta)\cos(n\theta_o) + \sin(n\theta)\sin(n\theta_o))$$

The relation of the viscous wake half width and of the centerline velocity defect to C_{Dp} is taken from semiempirical relations suggested in Reference 13.

The circulation per unit span around the pylon required in Figure 43 can be estimated from thin airfoil theory (Reference 14) as:

$$\Gamma = \pi c V_o (\alpha + \gamma/4)$$

where:

$c =$ pylon chord

$V_o =$ freestream fluid speed at pylon mid chord

$\alpha =$ angle of attack on pylon

$\gamma =$ pylon camber

2.2.5 Acoustic theory

Initially it was surmised that there would be no need to revise the acoustic prediction procedure as presented in Reference 1 except that the procedure would be applied separately to the front and rear rotors (more precisely to the BPF and higher harmonics of BPF tones of each rotor). To recapitulate this procedure, based on the steady loading calculated in the absence of any installation effects and the rotor geometry (for the steady thickness effects), a steady loading/thickness noise contribution is first calculated presuming each propeller to operate in uniform axial flow. Next unsteady loading and unsteady thickness source terms are evaluated for each propeller (based on the quasi steady theory and calculated velocity distortions due to the angle of attack, fuselage, aircraft horseshoe vortex system and the pylon) and once again noise due to the unsteady sources is calculated by presuming the propeller to be immersed in a stream of uniform axial flow. The steady and unsteady noise contributions are added with proper consideration of phase. As noted in Reference 1, this procedure seemed adequate in predicting the angle of attack effects measured and reported in Reference 15.

Initially this procedure was adopted and applied to the data reported in Reference 16 concerning angle of attack effects on a CRP. Figures 44 and 45 show a theory–data comparison for the installation effect on the BPF tone of the front rotor due to an angle of attack of 16°. The azimuthal variation of the installation effect was obtained at an angle of approximately 104° relative to the propellor inlet axis and hence theoretical predictions are shown for both 100° and 110°. Clearly there is a very substantial underestimation of the installation effect due to angle of attack. Considering the much better agreement obtained in case of Reference 15 (as reported in Reference 1), it may be pointed out that the front and rear rotors of Reference 16 have a larger number of blades (11 and 9) compared to that of Reference 15 (4) and are also characterized by loading levels (e.g., lift coefficient) much higher (3–4 times) than in case of Reference 15. Figures 44 and 45 are representative of all the theory–data comparisons attempted with respect to the data of Reference 16 namely, a tendency for the theory to substantially underpredict the measured noise change due to angle of attack.

Several avenues were pursued in an attempt to explain this significant theory–data discrepancy. One avenue related to the angle of attack effect proved to be worth pursuing. This approach is described in detail in Reference 3, and is outlined below. It actually pertains to a modification of the steady loading/thickness noise due to the small cross flow component of the steady flow and may be visualized by means of Figure 46. In this figure we show a steady source executing a circular motion as would be characteristic of steady sources rotating with the blade. Also shown in the figure is the uniform upwash provided by the cross flow due to angle of attack. Now the radiative efficiency of a source depends on the relative velocity between the source and the fluid surrounding it and as Figure 46 shows this relative velocity (and hence the radiative efficiency) is modulated in a non axisymmetric fashion due to the cross flow. This effect has been neglected in prior analyses.

To capture this effect, we proceed as follows. Including the cross flow (designated as "M_y" in Figure 47), the acoustic pressure due to steady loading satisfies:

$$p_{xx}(1-M_x^2) + p_{yy}(1-M_y^2) + p_{zz} + 2jkM_xp_x + 2jkM_yp_y - 2M_xM_yP_{xy} + k^2p = \left(\frac{\partial f_x}{\partial x} + \frac{1}{r}\frac{\partial f_\phi}{\partial \phi} \right)$$
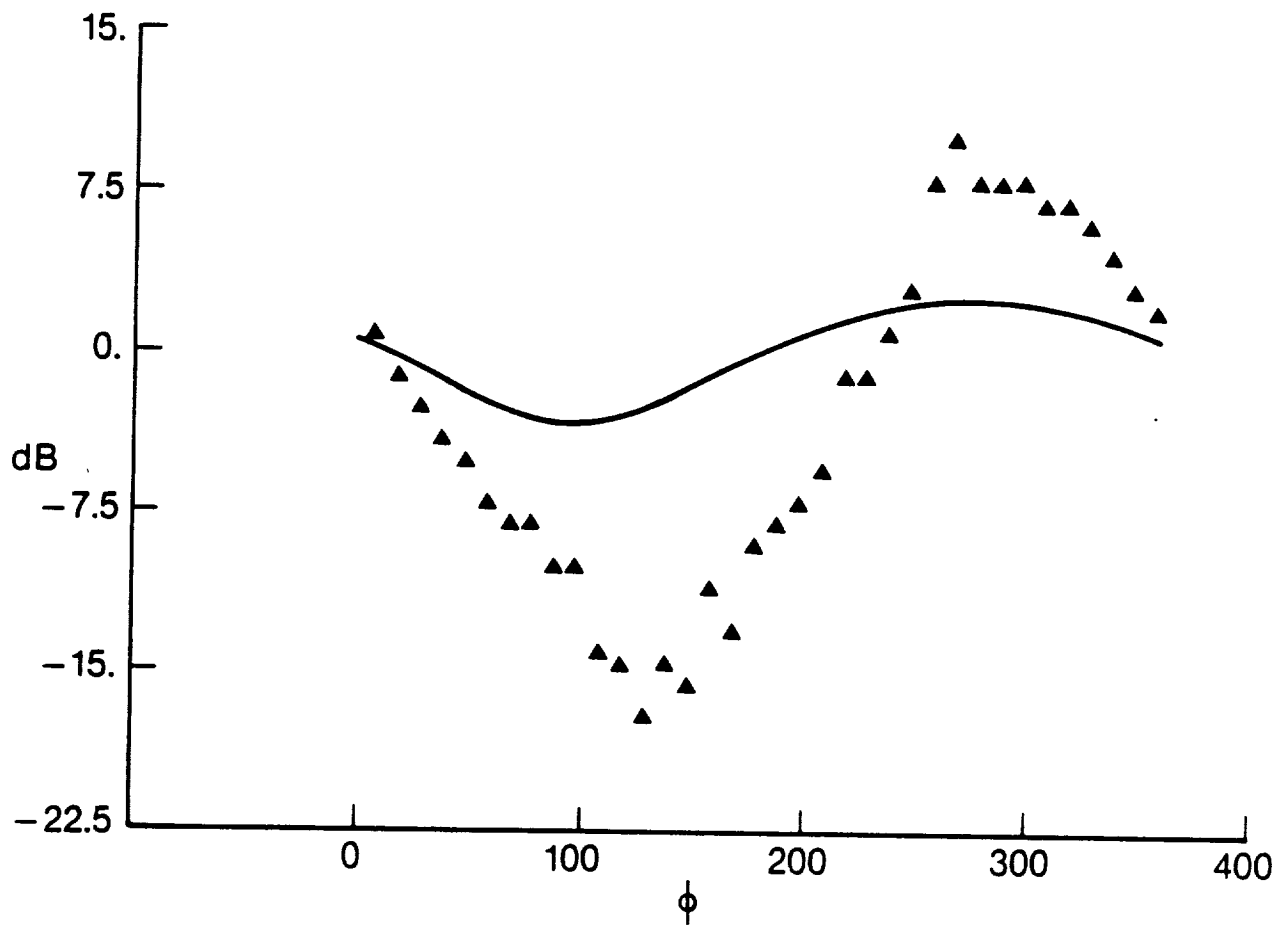
Figure 44. 11 x 9 Bladed 2-Foot-Diameter CRP; 75% Radius Pitch Angles 41.1/39.4 Degrees; rpm 7614/7674; Axial Flow Mach Number 0.2; 16 Degree Angle-of-Attack; Symbols are Measured Data and Solid Line is Prediction; θmeasured = 104° and θpredicted = 100°; Front Rotor BPF; Data Source is Reference 16; Increase/Decrease of Noise Due to Angle-of-Attack.
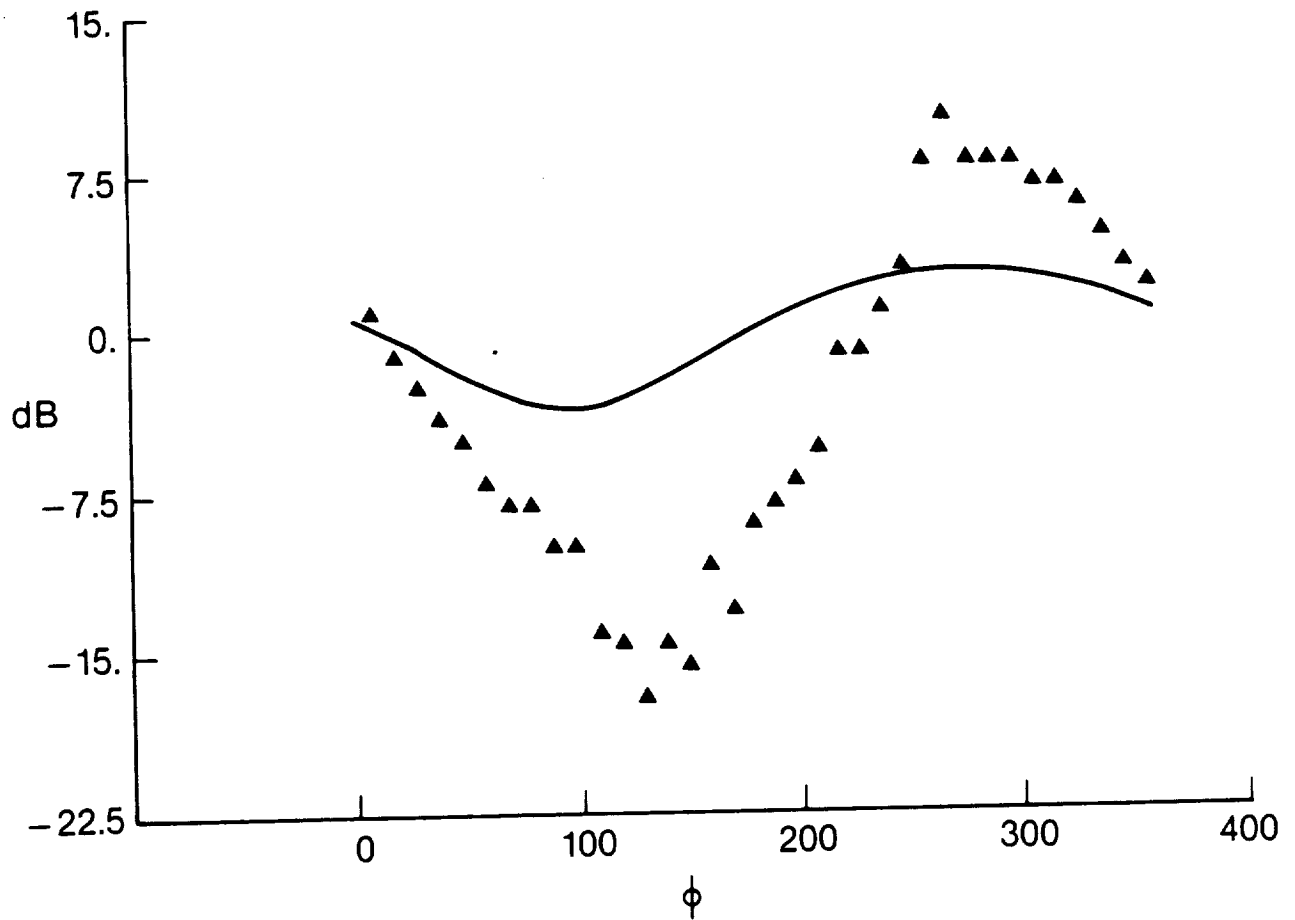
Figure 45. 11 x 9 Bladed 2-Foot-Diameter CRP; 75% Radius Pitch Angles 41.1/39.4 Degrees; rpm 7614/7674; Axial Flow Mach Number 0.2; 16 Degree Angle-of-Attack; Symbols are Measured Data and Solid Line is Prediction; θmeasured = 104° and θpredicted = 110°; Front Rotor BPF; Data Source is Reference 16; Increase/Decrease of Noise Due to Angle-of-Attack.
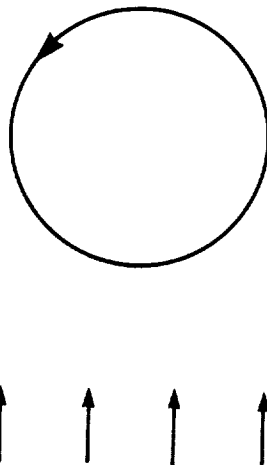
Figure 46. Modulation of Radiation Efficiency
of a Source Due to Cross Flow.

$$y = r \sin \phi$$
$$z = r \cos \phi$$

upstream
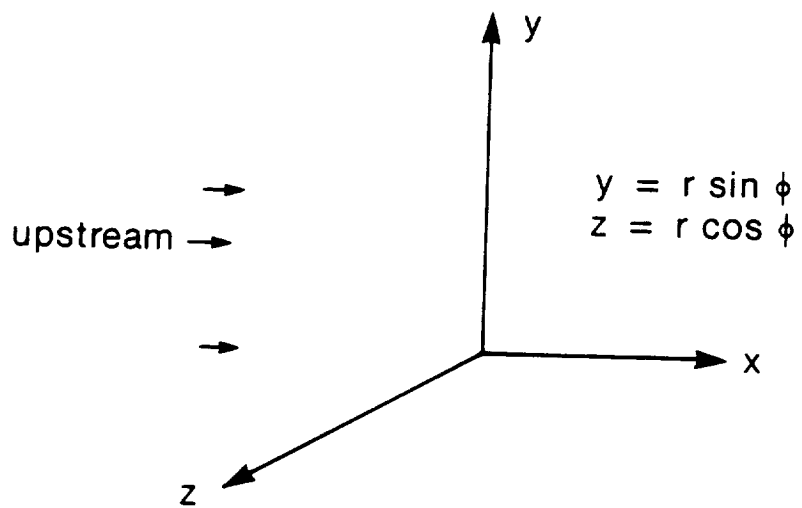
Figure 47. Coordinate System for Convected Wave Equation Including
Cross Flow.

where $k = \omega/c$, all quantities have a time dependence as exp $(-j\omega t)$, "c" is the speed of sound, M_x and M_y are axial and cross flow Mach numbers, "f_x, f_ϕ" are the force terms and $j = \sqrt{-1}$ and p_{xx} denotes $\partial^2 p/\partial x^2$, etc.

Let

$$f_x = f_{xo} \exp (jm\phi)\, \delta\,(x)\, \delta\,(r-a)$$

$$f_\phi = f_{\phi o} \exp (jm\phi)\, \delta\,(x)\, \delta\,(r-a)$$

where "ϕ" is the azimuthal coordinate, and note that thus far it has been possible to solve the above problem only to $O(M_y)$.

Define the axial Fourier transform pair:

$$P = \int_{-\infty}^{\infty} p \exp (-j\alpha x)\, dx$$

and

$$p = \frac{1}{2\pi} \int_{-\infty}^{\infty} P \exp (j\alpha x)\, dx$$

Then to $O(M_y)$, P satisfies:

$$P_{yy} + P_{zz} + 2jM_y P_y\,(k-\alpha M) + \left[(k-\alpha M)^2 - \alpha^2 \right] P = j \left[\alpha f_{xo} + \left(\frac{m}{a} \right) f_{\phi o} \right] \delta\,(r-a) e^{jm\phi}$$

Now let

$$\bar{P} = P \exp \left[jyM_y(k-\alpha M) \right]$$

Then to $O(M_y)$, $\bar{P}$ satisfies:

$$\bar{P}_{yy} + \bar{P}_{zz} + \left[(k-\alpha M)^2 - \alpha^2 \right] \bar{P} = j \left[\alpha f_{xo} + \left(\frac{m}{a} \right) f_{\phi o} \right] \delta(r-a) e^{jm\phi} \left[1 + M_y(k-\alpha M)\ \alpha \left(\frac{e^{j\phi} - e^{-j\phi}}{2} \right) \right]$$

Let

$$\gamma = \sqrt{(k-\alpha M)^2 - \alpha^2}$$

Then

$$P = \frac{\pi}{2} \left[(\alpha a)\, f_{xo} + m f_{\phi o} \right] \exp\left[-jM_y y\,(k-\alpha M) \right]\ *$$

$$\left[e^{jm\phi} J_m\,(\gamma a)\, H_m^{(1)}\,(\gamma r) + \frac{M_y\,(k-\alpha M)\, a}{2}\, e^{j(m+1)\phi} J_{m+1}\,(\gamma a)\, H_{m+1}^{(1)}\,(\gamma r) - \frac{M_y\,(k-\alpha M) a}{2}\, e^{j(m-1)\phi} J_{m-1}\,(\gamma a)\, H_{m-1}^{(1)}\,(\gamma r) \right]$$

We can now set x=R cos θ, r = R sin θ and y = R sin θ sin φ (see Figures 48 and 49) and carry out an asymptotic evaluation of "p" for large R. The full details of this asymptotic evaluation are not necessary and it suffices to note the following. Firstly in the evaluation of the "m" azimuthal mode in the above there are small $O(M_y)$ shifts in the point of stationary phase (relative to the case $M_y = 0$). For the "m–1" and "m+1" modes we can use the point of stationary phase as for "$M_y = 0$" since these are $O(M_y)$ contributions and hence relative to the "m" mode, these contribute as:

$$m-1: \quad \frac{-\exp\left[-j(\phi-\pi/2\right] M_y \text{ (ka)}}{2 (1+M \cos \psi)} J_{m-1}\left(\frac{ka \sin \psi}{1 + M \cos \psi}\right)$$

$$m+1: \quad \frac{-\exp\left[-j(\phi\pi/2\right] M_y \text{ (ka)}}{2 (1+M \cos \psi)} J_{m+1}\left(\frac{ka \sin \psi}{1 + M \cos \psi}\right)$$

where the relation between "θ" and retarded angular coordinate "ψ" is shown in Figure 48. Clearly the "m–1" term contributes much more significantly than the "m+1" term. A virtually identical treatment applies to thickness noise. Note that "ka = nBM_t" where "n" is harmonic of BPF noise, "B = number of blades" and "M_t = wheel tip Mach number" at radius "a".

This revised acoustic theory was applied both to the theory–data comparisons reported in Reference 1 and the data of Reference 16.

2.2.6. Theory–data comparisons

The computer code developed and delivered under this program uses the revised acoustic theory for steady loading/thickness noise and the old acoustic theory of Reference 1 (wherein the only mean flow effect dealt with is a uniform, axial flow) for the unsteady loading/thickness noise. This approach is consistent with the idea that at present only an $O(M_y)$ acoustic theory has been developed where "M_y" is the crossflow Mach number due to angle of attack. Also while the computer code has provisions for considering installation effects due to sources other than angle of attack, the theory–data comparisons shown herein are only for angle of attack and are restricted to data reported in References 15 and 16. The coordinate system for "θ,φ" is shown in Figure 49. All "θ" coordinates referred to in Figures 50 through 72 are current coordinates (as opposed to retarded coordinates). All predictions are for the fundamental BPF tone of the relevant propeller and are for the noise change due to angle of attack. It should be noted that, in common with the isolated rotors predictions of Section 2.3.2, the predictions shown here are for the acoustic farfield, and while every attempt has been made to ensure correspondence between the physical measurement location and that used for the prediction, it would be misleading to assume that exact coincidence has been achieved. Also in all of the predictions shown in Figures 44, 45, and 50 through 72, the phase lag due to unsteady lift response is not included. Our assessment, as in Reference 1, continues to be that there is no evidence that inclusion of this effect is warranted based on the theory–data comparisons for the angle of attack effect. The applicability of linearized, two dimensional convected gust response formulae to the present problem is highly dubious in any event.

In Figures 50 through 57, using the new acoustic theory, we show theory–data comparisons for the SR–2 data of Reference 15 that were used in Reference 1. It can be seen that the comparisons are at least as good as shown in Reference 1. At shallow angles to the propeller axis the sound pressure levels tend to be low and hence it is not surprising that "discrepancies" between theory and data appear large at these locations. The new effect discussed in Section 2.2.5 scales as "nBM_t" and

72
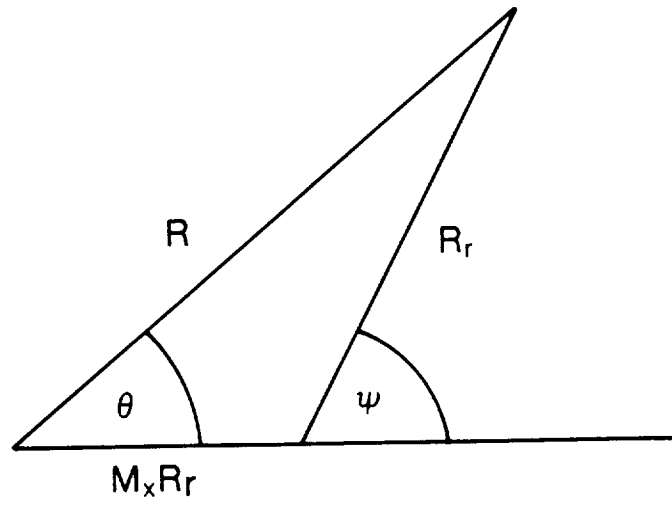
Figure 48. Relation Between Current (R, θ) and Retarded Coordinates (R$_r$, ψ).

Flow ⟶

Propellor Axis

φ

Forward Looking Aft
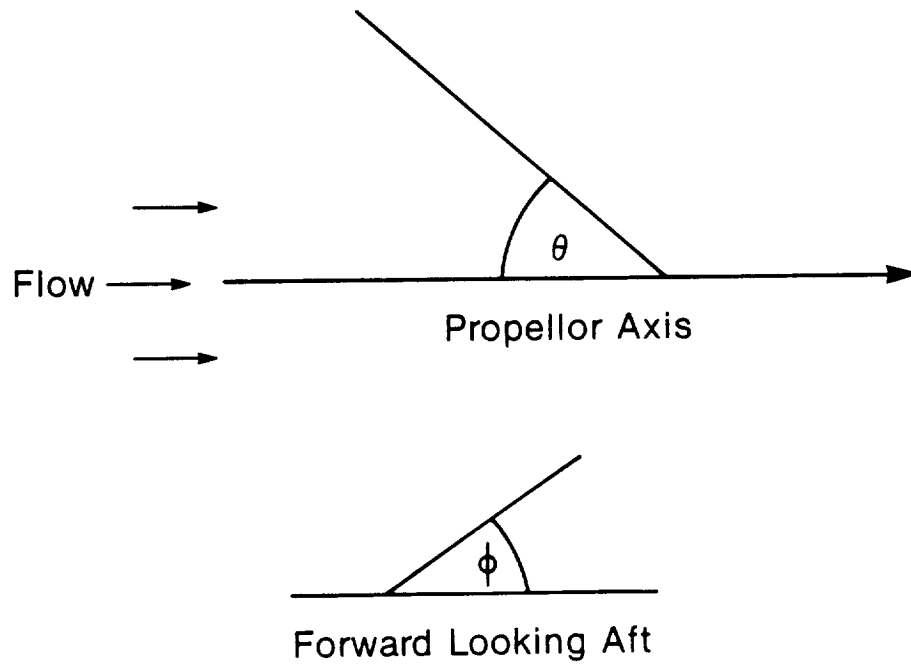
Figure 49. θ, φ Coordinate System used for Theory Data Comparisons.
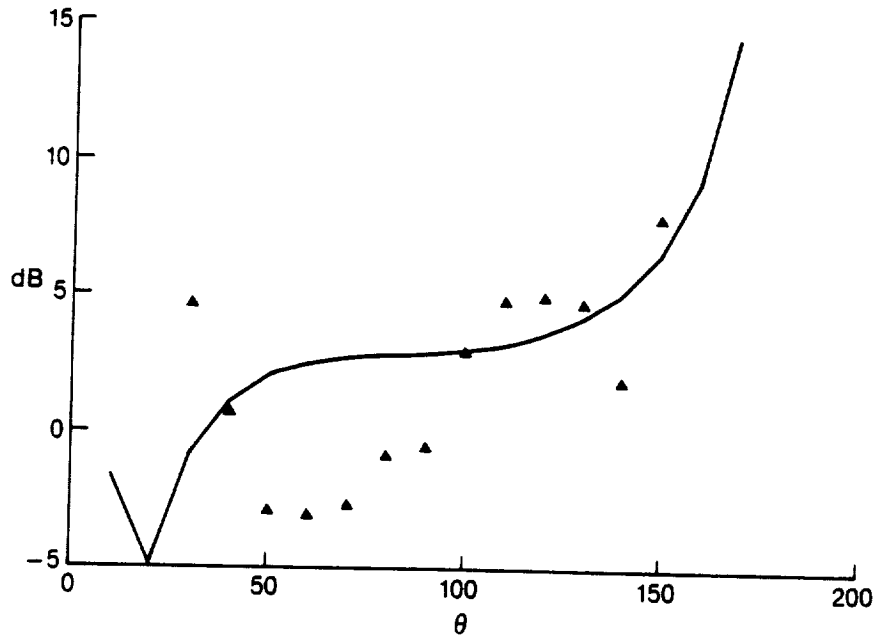
Figure 50. Four-Bladed SR-2, 443 fps Tip Speed, 100 fps Forward Flight Speed, Fundamental Blade Passing Frequency Noise. Acoustic Data Source is Reference 15, Symbols are Measured Data, and Full Line is Theoretical Prediction. Increase/Decrease of Noise Due to 9° Angle-of-Attack (Relative to Zero Angle-of-Attack) Versus θ, ϕ = 0°.
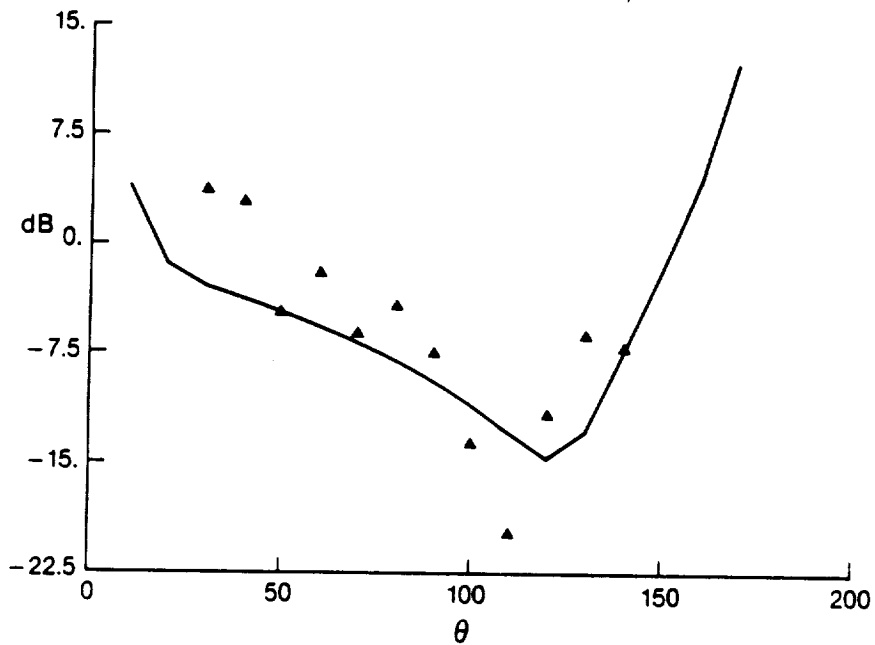
Figure 51. Four-Bladed SR-2, 443 fps Tip Speed, 100 fps Forward Flight Speed, Fundamental Blade Passing Frequency Noise. Acoustic Data Source is Reference 15, Symbols are Measured Data, and Full Line is Theoretical Prediction. Increase/Decrease of Noise Due to 9° Angle-of-Attack (Relative to Zero Angle-of-Attack) Versus θ, ϕ = 90°.

74
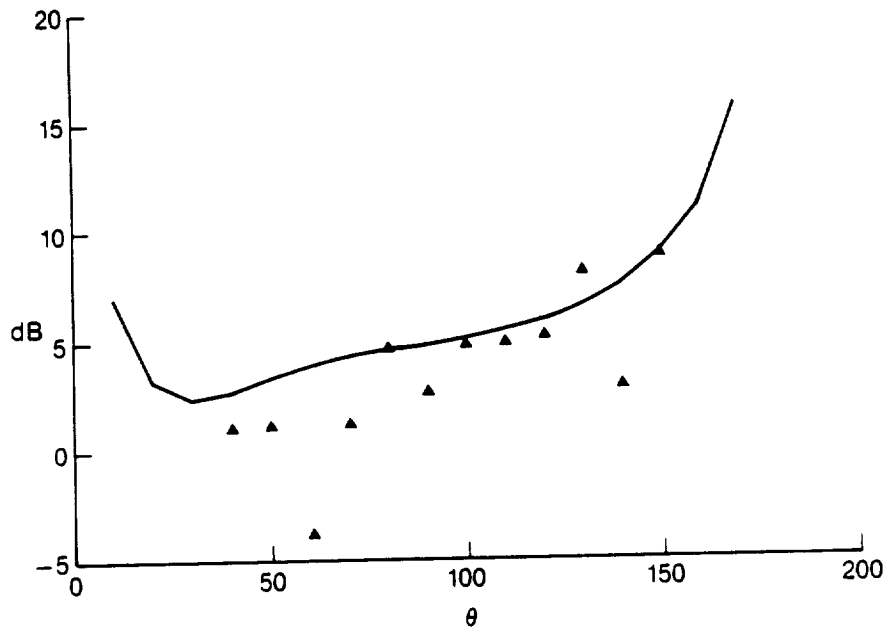
Figure 52. Four-Bladed SR-2, 443 fps Tip Speed, 100 fps Forward Flight Speed, Fundamental Blade Passing Frequency Noise. Acoustic Data Source is Reference 15, Symbols are Measured Data, and Full Line is Theoretical Prediction. Increase/Decrease of Noise Due to 9° Angle-of-Attack (Relative to Zero Angle-of-Attack) Versus θ, $\phi = 270°$.
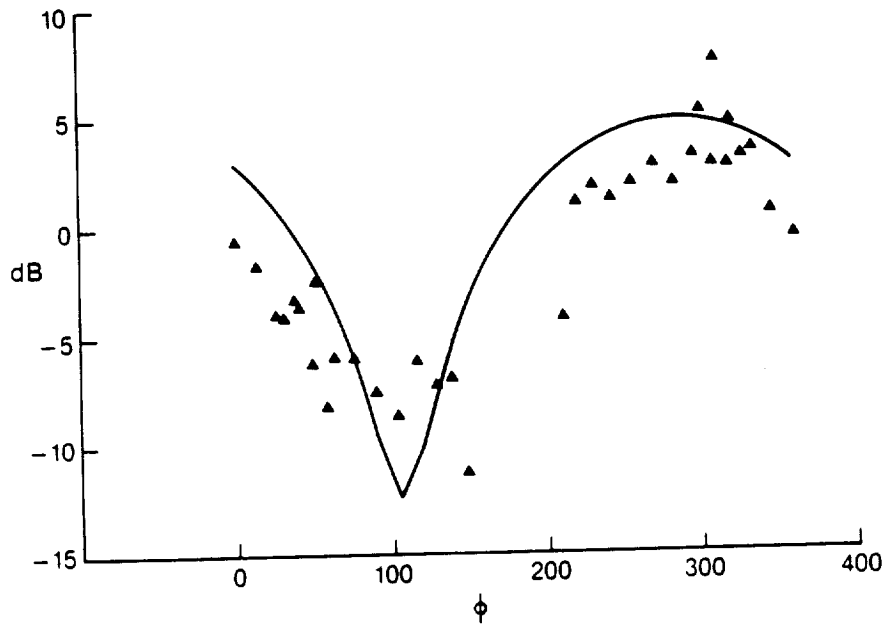
Figure 53. Four-Bladed SR-2, 443 fps Tip Speed, 100 fps Forward Flight Speed, Fundamental Blade Passing Frequency Noise. Acoustic Data Source is Reference 15, Symbols are Measured Data, and Full Line is Theoretical Prediction. Increase/Decrease of Noise Due to 9° Angle-of-Attack (Relative to Zero Angle-of-Attack) Versus ϕ, $\theta = 90°$.

75
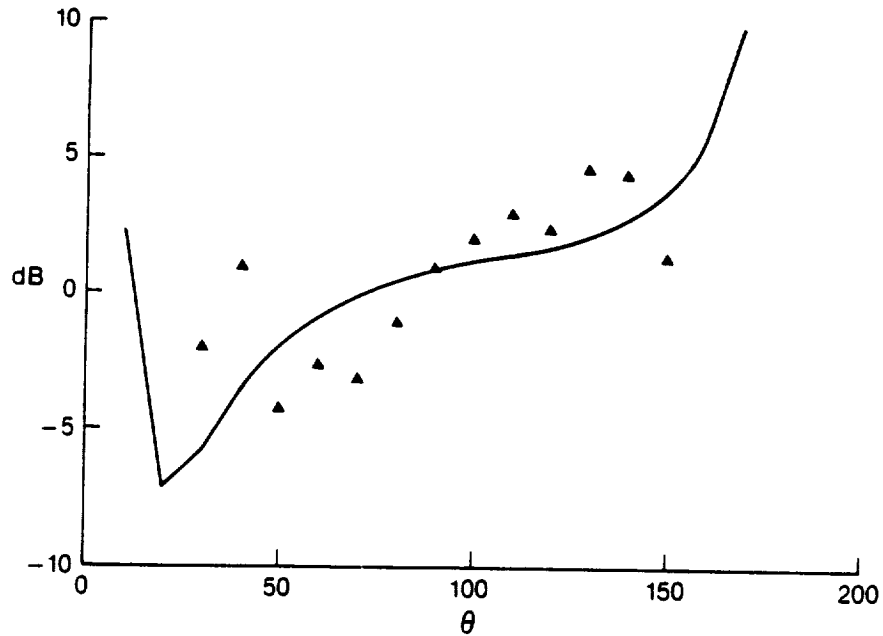
Figure 54. Four-Bladed SR-2, 745 fps Tip Speed, 100 fps Forward Flight Speed, Fundamental Blade Passing Frequency Noise. Acoustic Data Source is Reference 15, Symbols are Measured Data, and Full Line is Theoretical Prediction. Increase/Decrease of Noise Due to 9° Angle-of-Attack (Relative to Zero Angle-of-Attack) versus θ, φ = 0°.
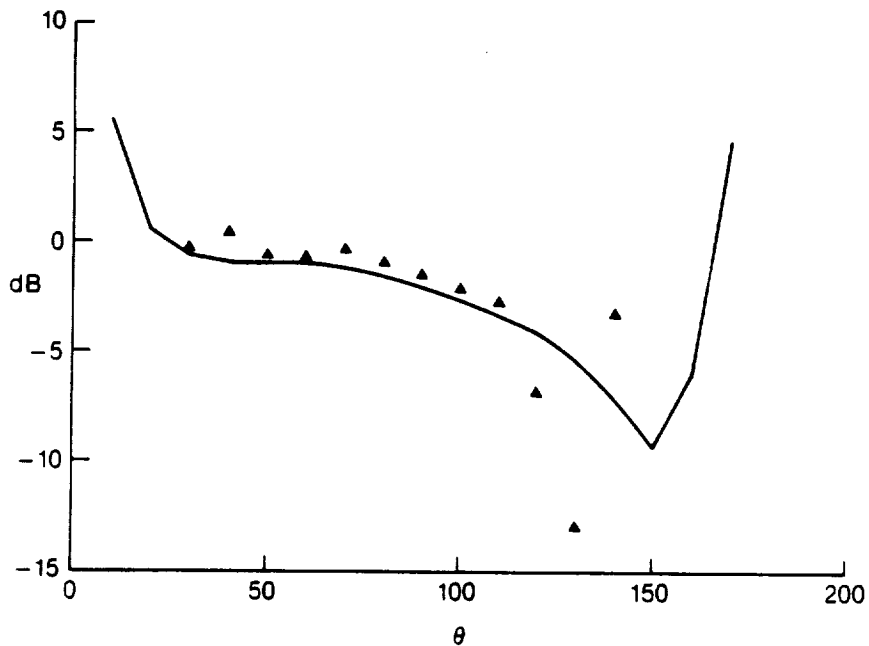
Figure 55. Four-Bladed SR-2, 745 fps Tip Speed, 100 fps Forward Flight Speed, Fundamental Blade Passing Frequency Noise. Acoustic Data Source is Reference 15, Symbols are Measured Data, and Full Line is Theoretical Prediction. Increase/Decrease of Noise Due to 9° Angle-of-Attack (Relative to Zero Angle-of-Attack) versus θ, φ = 90°.
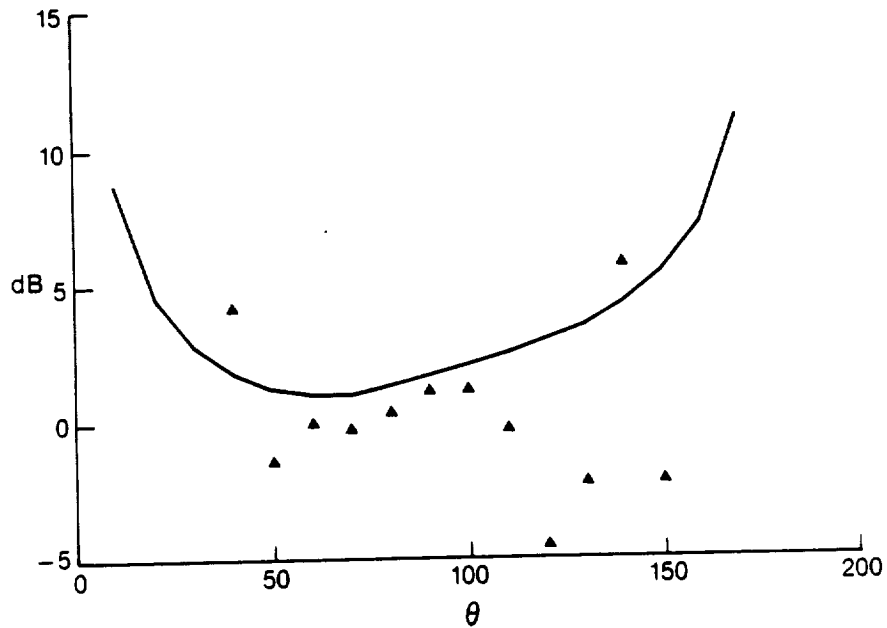
Figure 56. Four-Bladed SR-2, 745 fps Tip Speed, 100 fps Forward Flight Speed, Fundamental Blade Passing Frequency Noise. Acoustic Data Source is Reference 15, Symbols are Measured Data, and Full Line is Theoretical Prediction. Increase/Decrease of Noise Due to 9° Angle-of-Attack (Relative to Zero Angle-of-Attack) versus θ, φ = 270°.
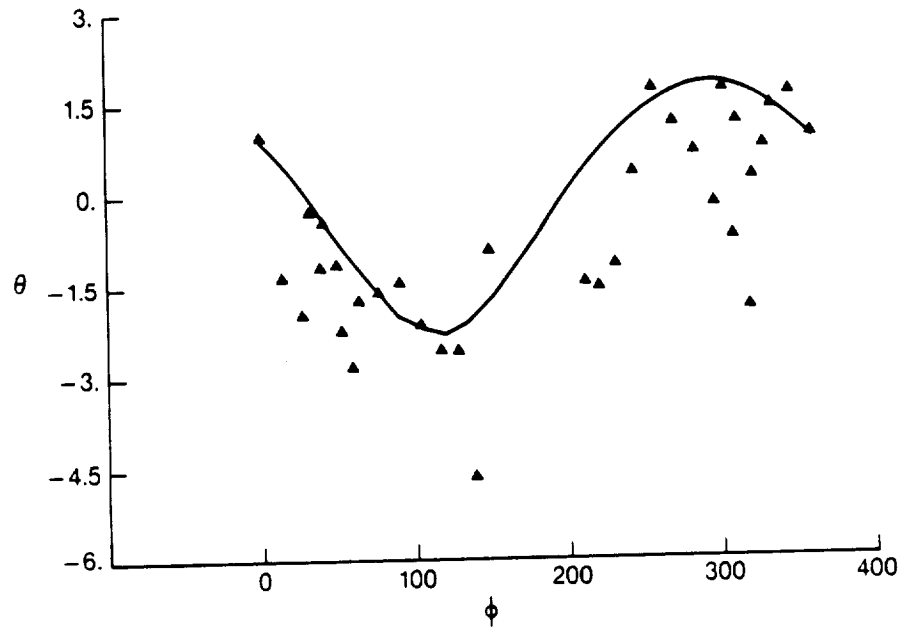

Figure 57. Four-Bladed SR-2, 745 fps Tip Speed, 100 fps Forward Flight Speed, Fundamental Blade Passing Frequency Noise. Acoustic Data Source is Reference 15, Symbols are Measured Data, and Full Line is Theoretical Prediction. Increase/Decrease of Noise Due to 9° Angle-of-Attack (Relative to Zero Angle-of-Attack) versus φ, θ = 90°.

77
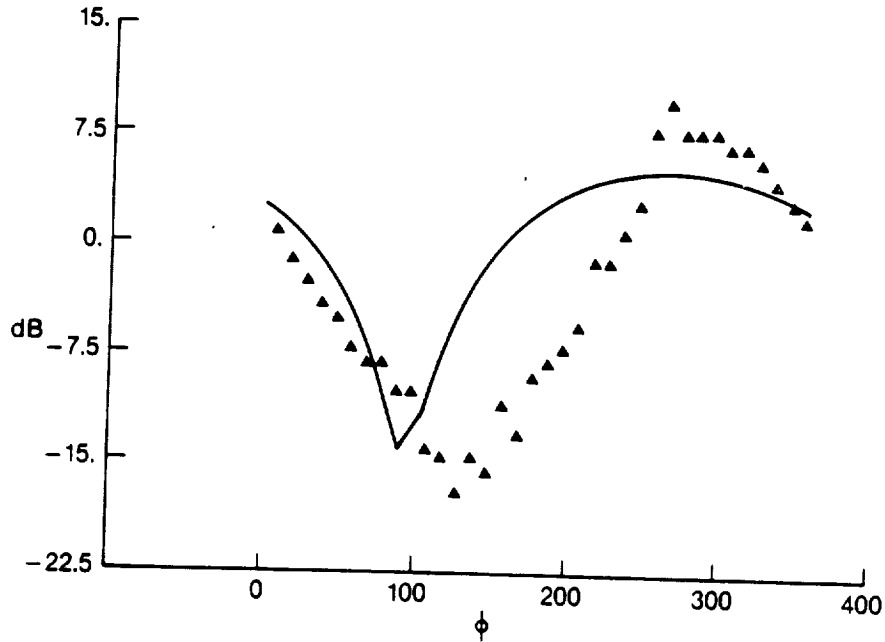
Figure 58. 11 x 9 Bladed 2-Foot-Diameter CRP; 75% Radius Pitch Angles 41.1°/39.4°; rpm 7614/7674; Axial Flow Mach Number 0.2; 16° Angle-of-Attack; Symbols are Measured Data and Solid Line is Prediction; θmeasured = 104° and θpredicted = 100°; Front Rotor BPF; Data Source is Reference 16; Increase/Decrease of Noise Due to Angle-of-Attack.
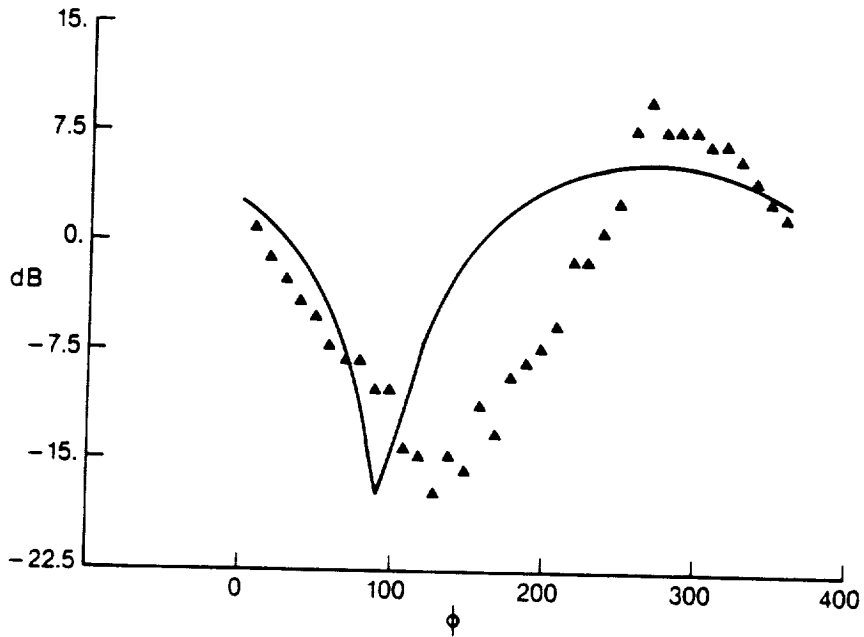
Figure 59. 11 x 9 Bladed 2-Foot-Diameter CRP; 75% Radius Pitch Angles 41.1°/39.4°; rpm 7614/7674; Axial Flow Mach Number 0.2; 16° Angle-of-Attack; Symbols are Measured Data and Solid Line is Prediction; θmeasured = 104° and θpredicted = 110°; Front Rotor BPF; Data Source is Reference 16; Increase/Decrease of Noise Due to Angle-of-Attack.

78
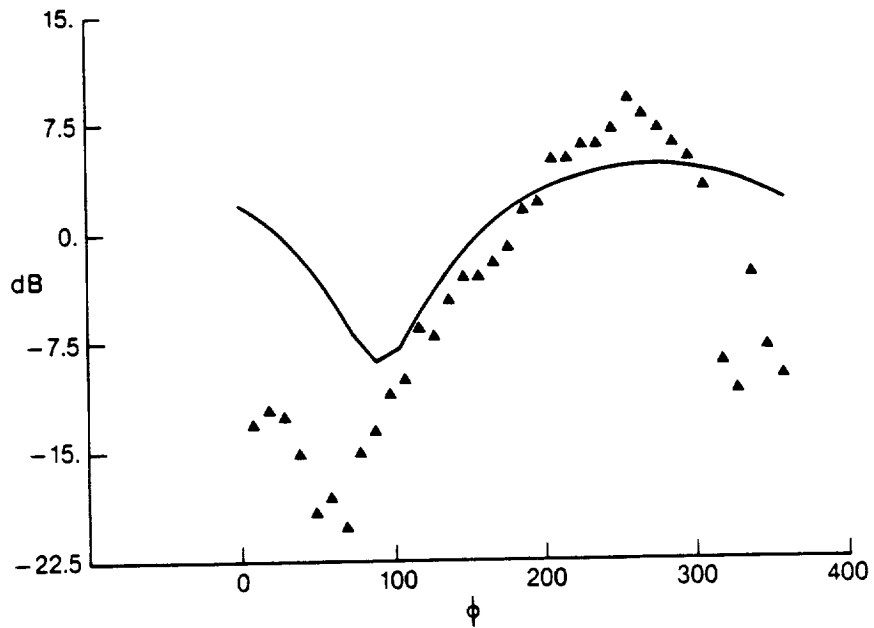
Figure 60. 11 x 9 Bladed 2-Foot-Diameter CRP; 75% Radius Pitch Angles 41.1°/39.4°;
rpm 7614/7674; Axial Flow Mach Number 0.2; 16° Angle-of-Attack;
Symbols are Measured Data and Solid Line is Prediction; θmeasured
= θpredicted = 90°; Rear Rotor BPF; Data Source is Reference 16;
Increase/Decrease of Noise Due to Angle-of-Attack.
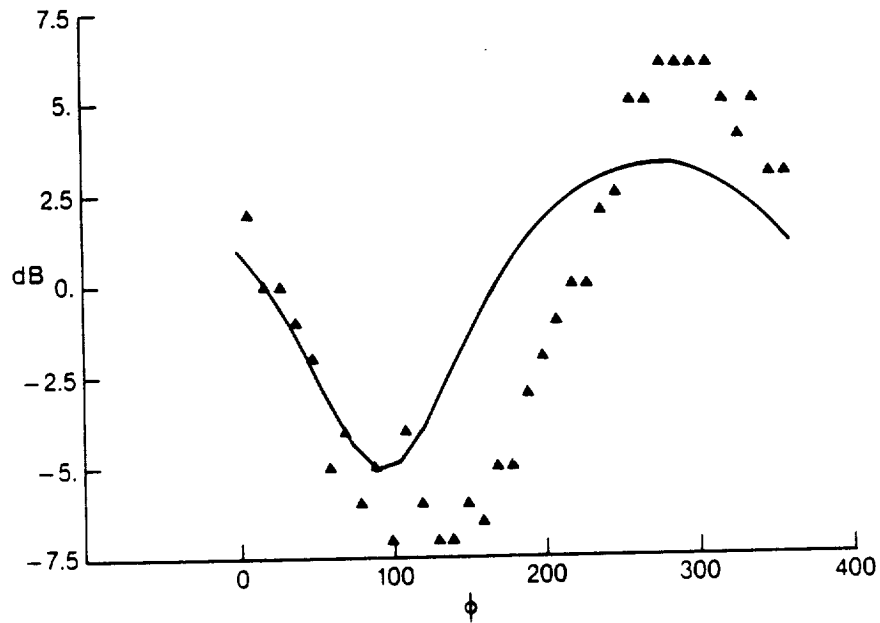
Figure 61. 11 x 9 Bladed 2-Foot-Diameter CRP; 75% Radius Pitch Angles 36.4°/36.5°;
rpm 7633/7695; Axial Flow Mach Number 0.2; 8° Angle-of-Attack; Symbols
are Measured Data and Solid Line is Prediction; θmeasured = 104° and
θpredicted = 100°; Front Rotor BPF; Data Source is Reference 16;
Increase/Decrease of Noise Due to Angle-of-Attack.
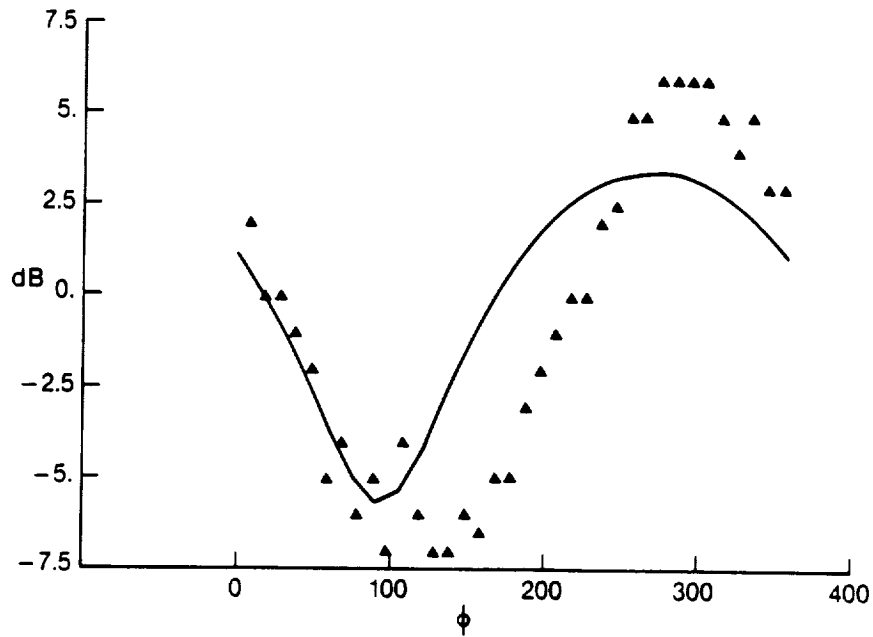
Figure 62. 11 x 9 Bladed 2-Foot-Diameter CRP; 75% Radius Pitch Angles 36.4°/36.5°; rpm 7633/7695; Axial Flow Mach Number 0.2; 8° Angle-of-Attack; Symbols are Measured Data and Solid Line is Prediction; θmeasured = 104° and θpredicted = 110°; Front Rotor BPF; Data Source is Reference 16; Increase/Decrease of Noise Due to Angle-of-Attack.
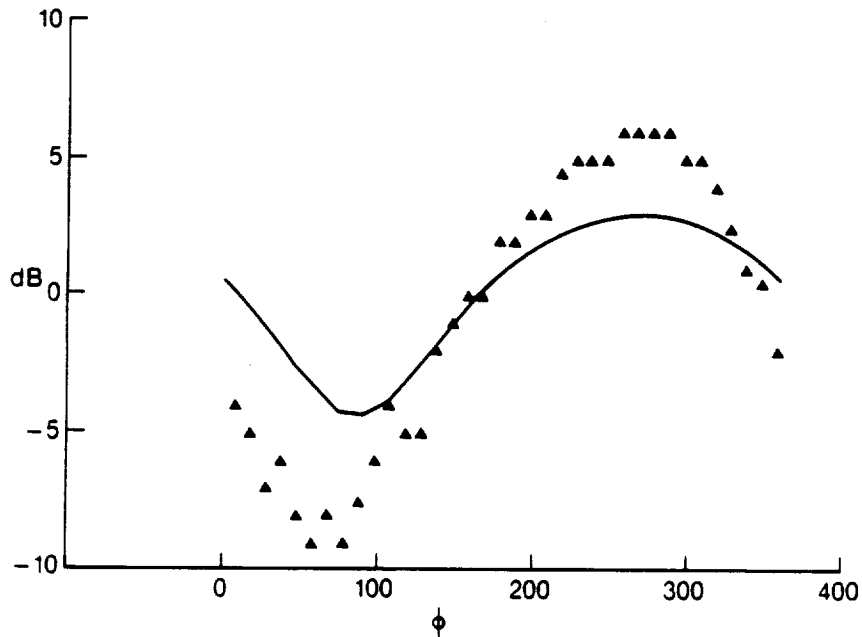
Figure 63. 11 x 9 Bladed 2-Foot-Diameter CRP; 75% Radius Pitch Angles 36.4°/36.5°; rpm 7633/7695; Axial Flow Mach Number 0.2; 8° Angle-of-Attack; Symbols are Measured Data and Solid Line is Prediction; θmeasured = θpredicted = 90°; Rear Rotor BPF; Data Source is Reference 16; Increase/Decrease of Noise Due to Angle-of-Attack.
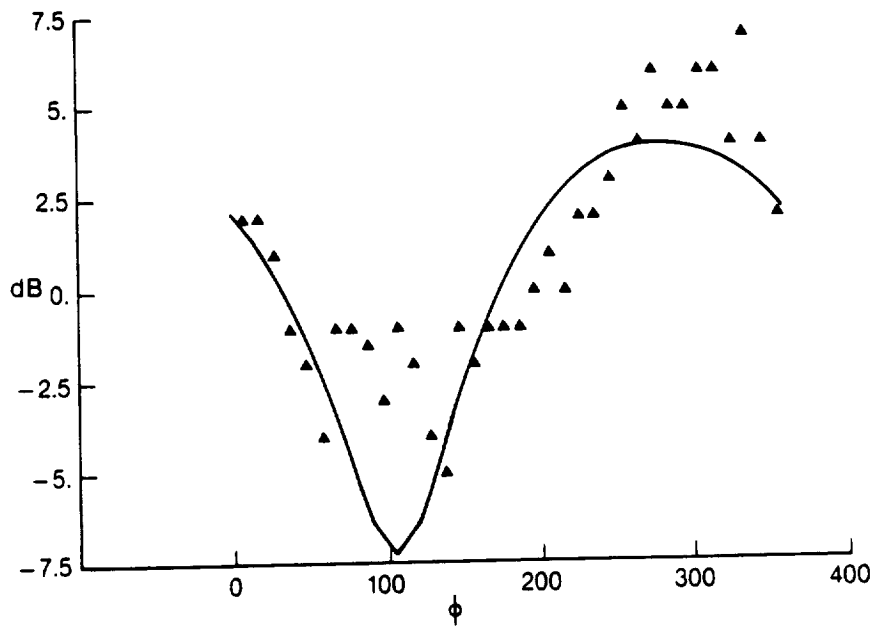
Figure 64. 11 x 9 Bladed 2-Foot-Diameter CRP; 75% Radius Pitch Angles 36.4°/36.5°; rpm 7633/7695; Axial Flow Mach Number 0.2; 8° Angle-of-Attack; Symbols are Measured Data and Solid Line is Prediction; θmeasured = 67° and θpredicted = 60°; Front Rotor BPF; Data Source is Reference 16; Increase/Decrease of Noise Due to Angle-of-Attack.
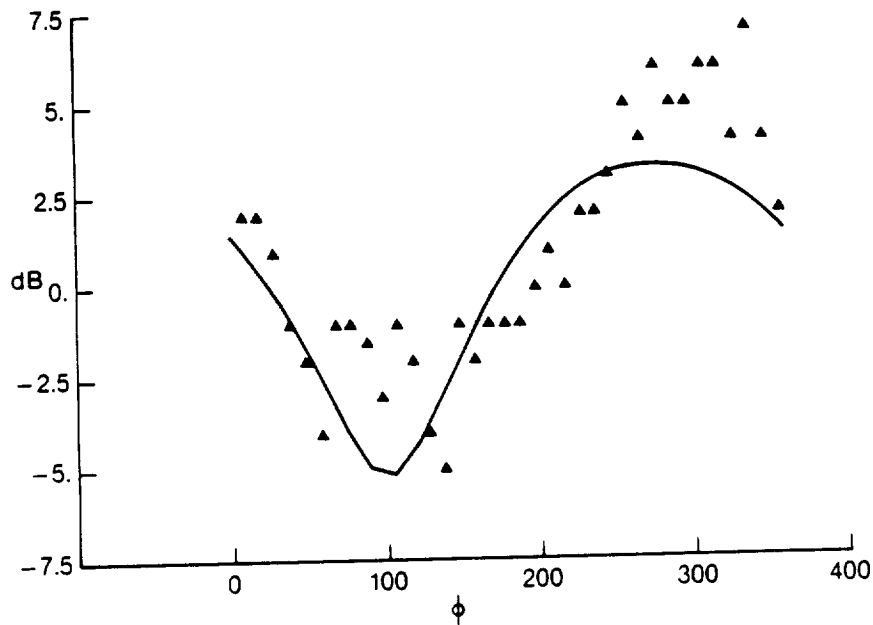
Figure 65. 11 x 9 Bladed 2-Foot-Diameter CRP; 75% Radius Pitch Angles 36.4°/36.5°; rpm 7633/7695; Axial Flow Mach Number 0.2; 8° Angle-of-Attack; Symbols are Measured Data and Solid Line is Prediction; θmeasured = 67° and θpredicted = 70°; Front Rotor BPF; Data Source is Reference 16; Increase/Decrease of Noise Due to Angle-of-Attack.
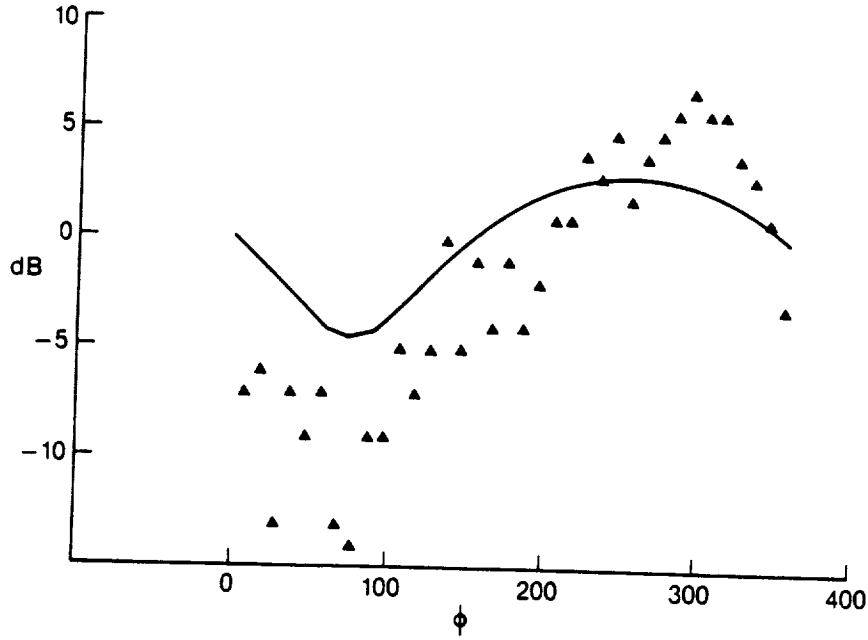
Figure 66. 11 x 9 Bladed 2-Foot-Diameter CRP; 75% Radius Pitch Angles 36.4°/36.5°; rpm 7633/7695; Axial Flow Mach Number 0.2; 8° Angle-of-Attack; Symbols are Measured Data and Solid Line is Prediction; θmeasured = 59° and θpredicted = 60°; Rear Rotor BPF; Data Source is Reference 16; Increase/Decrease of Noise Due to Angle-of-Attack.
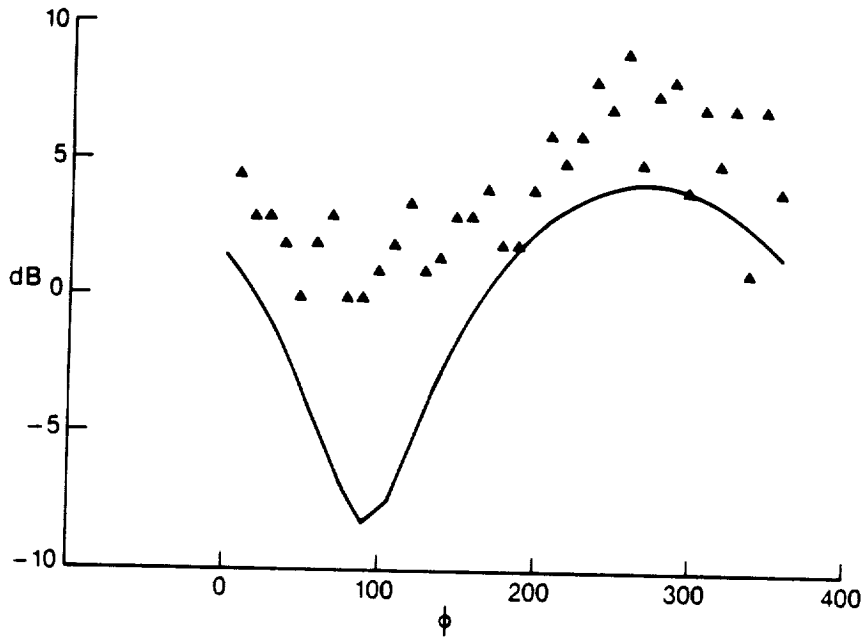

Figure 67. 11 x 9 Bladed 2-Foot-Diameter CRP; 75% Radius Pitch Angles 36.4°/36.5°; rpm 7633/7695; Axial Flow Mach Number 0.2; 8° Angle-of-Attack; Symbols are Measured Data and Solid Line is Prediction; θmeasured = 129° and θpredicted = 130°; Front Rotor BPF; Data Source is Reference 16; Increase/Decrease of Noise Due to Angle-of-Attack.

82
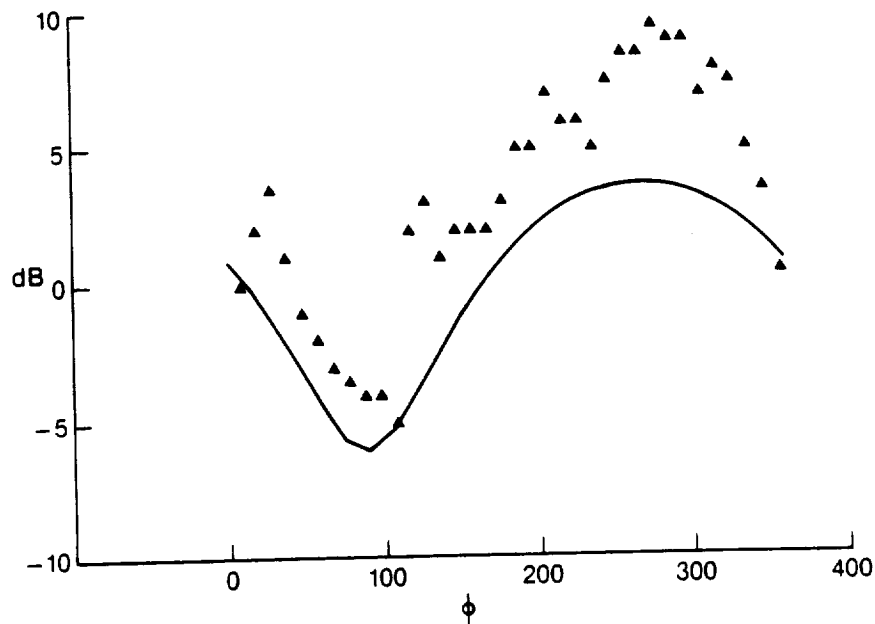
Figure 68. 11 x 9 Bladed 2-Foot-Diameter CRP; 75% Radius Pitch Angles 36.4°/36.5°; rpm 7633/7695; Axial Flow Mach Number 0.2; 8° Angle-of-Attack; Symbols are Measured Data and Solid Line is Prediction; θmeasured = 123° and θpredicted = 120°; Rear Rotor BPF; Data Source is Reference 16; Increase/Decrease of Noise Due to Angle-of-Attack.
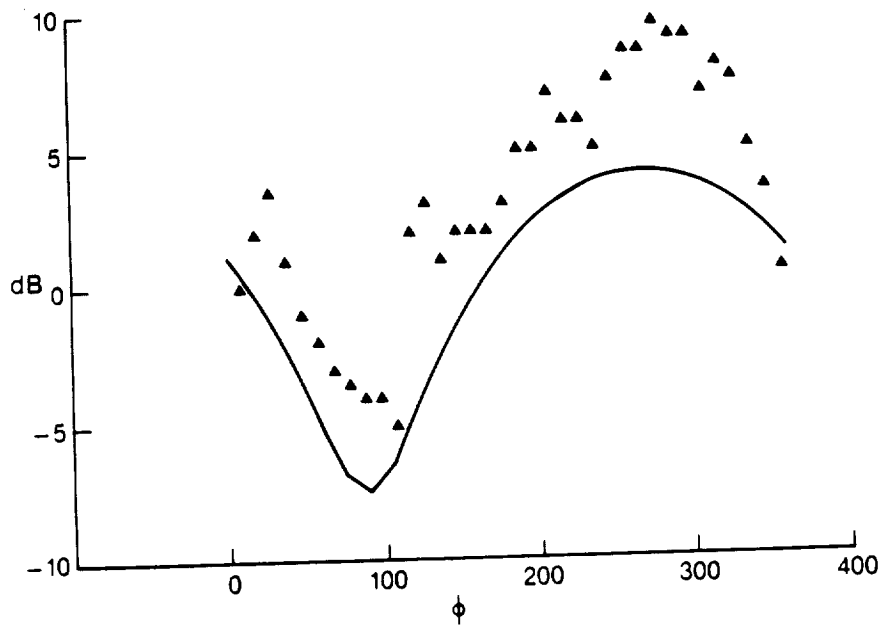

Figure 69. 11 x 9 Bladed 2-Foot-Diameter CRP; 75% Radius Pitch Angles 36.4°/36.5°; rpm 7633/7695; Axial Flow Mach Number 0.2; 8° Angle-of-Attack; Symbols are Measured Data and Solid Line is Prediction; θmeasured = 123° and θpredicted = 130°; Rear Rotor BPF; Data Source is Reference 16; Increase/Decrease of Noise Due to Angle-of-Attack.
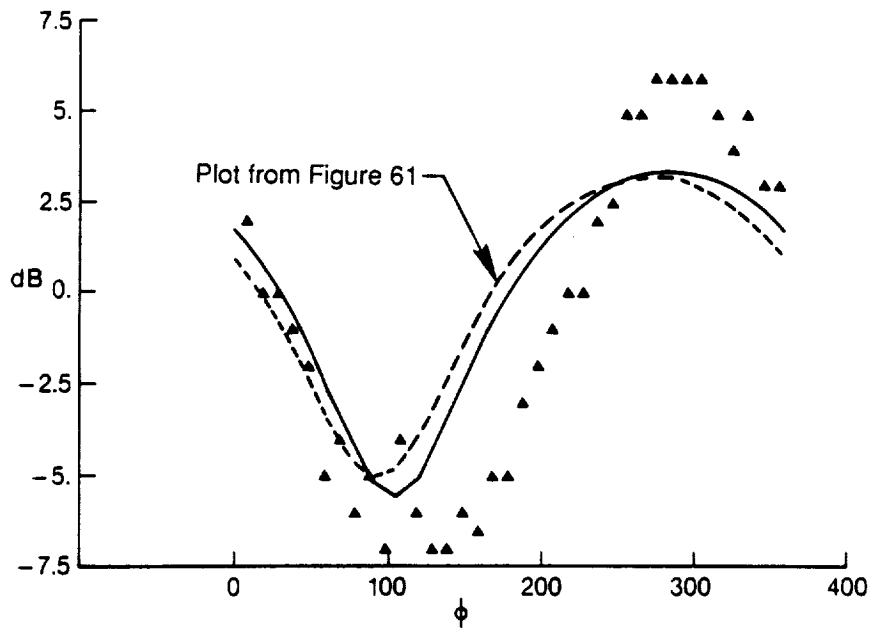
Figure 70. 11 x 9 Bladed 2-Foot-Diameter CRP; 75% Radius Pitch Angles 36.4°/36.5°; rpm 7633/7695; Axial Flow Mach Number 0.2; 8° Angle-of-Attack; Symbols are Measured Data and Solid Line is Prediction; θmeasured = 104° and θpredicted = 100°; Front Rotor BPF; a 10% 1/Rev Axial Velocity Distortion is Assumed; Data Source is Reference 16; Increase/Decrease of Noise Due to Angle-of-Attack.
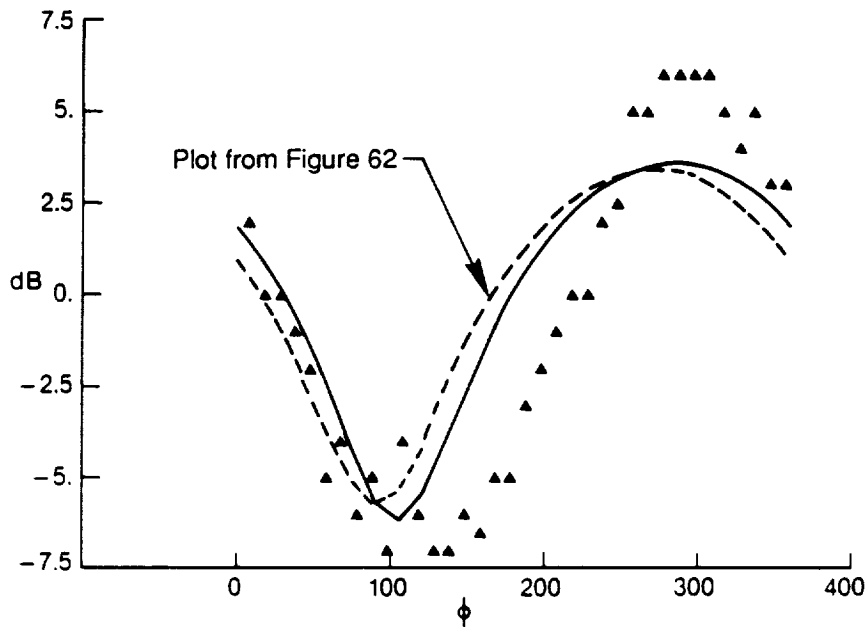

Figure 71. 11 x 9 Bladed 2-Foot-Diameter CRP; 75% Radius Pitch Angles 36.4°/36.5°; rpm 7633/7695; Axial Flow Mach Number 0.2; 8° Angle-of-Attack; Symbols are Measured Data and Solid Line is Prediction; θmeasured = 104° and θpredicted = 110°; Front Rotor BPF; a 10% 1/Rev Axial Velocity Distortion is Assumed; Data Source is Reference 16; Increase/Decrease of Noise Due to Angle-of-Attack.

84

C-2
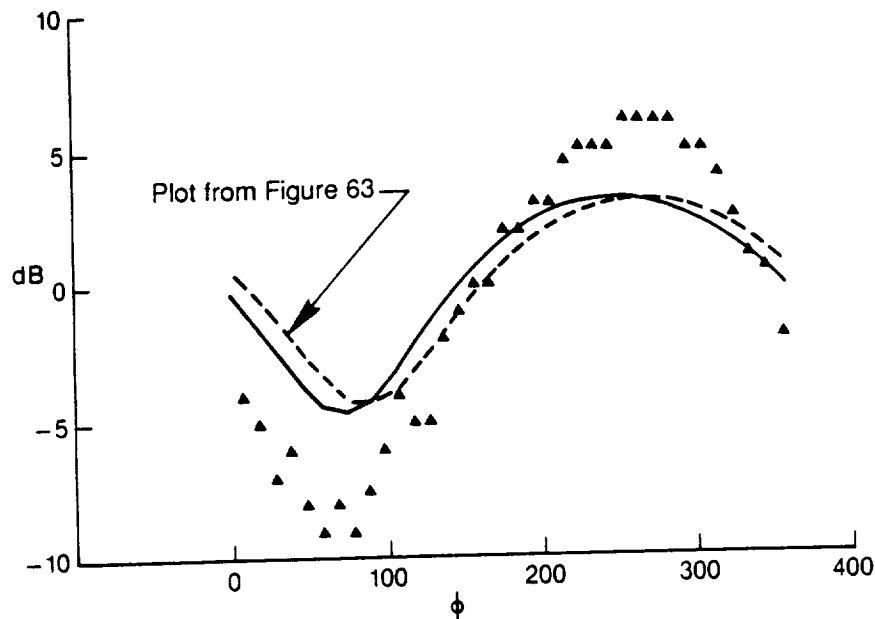
Figure 72. 11 x 9 Bladed 2-Foot-Diameter CRP; 75% Radius Pitch Angles 36.4°/36.5°; rpm 7633/7695; Axial Flow Mach Number 0.2; 8° Angle-of-Attack; Symbols are Measured Data and Solid Line is Prediction; θmeasured = θpredicted = 90°; Front Rotor BPF; a 10% 1/Rev Axial Velocity Distortion is Assumed; Data Source is Reference 16; Increase/Decrease of Noise Due to Angle-of-Attack.

locations. The new effect discussed in Section 2.2.5 scales as "nBM_t" and pertains only to steady loading/thickness noise. Thus it is not surprising that the new effect is not very consequential for a lightly loaded, four-bladed propeller such as the SR-2.

In Figures 58 through 72, we show the theory data comparisons for the CRP data reported in Reference 16. Several comments concerning these theory–data comparisons are noted below.

1. In cases where the measured "θ" is not close to a multiple of 10°, predictions for multiples of 10° bracketing the measured "θ" are both compared with the data. Note the previously stated reservations concerning establishing an exact correspondence between measured and predicted "θ".

2. Figures 58 and 59 may be compared to Figures 44 and 45 (the data shown in these figures are the same). A dramatic improvement is now evident with the revised acoustic theory in terms of the substantial under prediction of the old acoustic theory of the angle of attack effect.

3. Several figures such as 60, 63, and 66 indicate that some aspects of the effects on rear rotor noise are still significantly underpredicted. The rear rotor has fewer blades (9 versus 11) than the front rotor and hence the predicted magnitude of the new effect (recall the "mB_t" scaling law for the new effect) is correspondingly smaller. Also as far as unsteady effects are concerned, the steady and quasi–steady CRP theory developed herein predicts a "smoothing" effect of the front rotor in terms of the

85

rear rotor are also predicted to be smaller than on the front rotor. At any rate the reasons for some of the discrepancies related to the rear rotor are not clear.

4. In some instances, as in Figures 64, 65, 67, 68, and 69, the data are incompatible with the idea of installation effects due to a one per rev distortion as would occur with angle of attack. In the case of Figure 67, all the measured data appear as increases which is difficult to understand although it is possible that, as before, tone data at this frequency was buried in the broadband background over some of the azimuthal traverse. For the rest of these figures, the absolute magnitude of the increases in decibels exceeds that of the decreases which is also hard to rationalize in the context of a once per rev distortion. It may be noted that all the data pertaining to these figures are for angular locations at shallower angles to the propeller axis where as noted previously in the context of the data of Reference 15, the sound pressure levels are low making the assessment of installation effect more difficult in terms of experiments.

5. Finally if we examine Figures 61, 62, and 63 (as a typical case), it would appears that the maxima and minima of the data appear at larger "ϕ" with respect to the theory for the front rotor and vice-versa for the rear rotor. For the CRP used in Reference 6, the front rotor spins in the direction of decreasing "ϕ" (clockwise forward looking aft) and hence this shift is incompatible with the idea of a phase lag in lift response. This was checked by running the computer code including phase lag which only made the shifts in Figures 61 through 63 appear larger. It may be surmised however that when an elongated centerbody such as used in Reference 16 is placed at an angle of attack to the freestream and the rotors are placed aft of the maximum diameter location of the centerbody, the propeller blades could experience a once per rev distortion of incoming axial velocity such that this velocity is diminished on top and increased on the bottom. In Figures 70 through 72, a calculation was carried out assuming the presence of such an axial velocity distortion of magnitude 10% of the freestream velocity. Comparing these results with Figures 61 through 63 (reproduced here), clearly a shift is obtained of the theory which is in the right direction relative to the data. The purpose of this exercise is to indicate that small distortions additional to the tangential velocity distortion created by angle of attack can cause significant shifts of the predictions in the "ϕ" direction even if the magnitudes are not much affected.

2.2.7 Concluding remarks

In this report an approach based on steady and quasi-steady aerodynamics of a CRP was developed to predict both the steady loading/thickness BPF noise and the unsteady loading/ thickness BPF noise. Originally the acoustic theory used was as in Reference 1. Application of this approach to the data of Reference 16 indicated a severe underestimation of the magnitude of the effect of angle of attack on BPF noise from a CRP. A new idea has been developed in this report based on the notion that the small crossflow due to angle of attack (designated as "M_y") actually profoundly alters the steady loading/thickness BPF noise (causing it to be azimuthally non uniform). This effect may be far more important than unsteady loading/thickness noise for heavily loaded, high tip Mach number propellers with a large number of blades. This effect has been calculated only to $O(M_y)$ in this report. Revised theory-data comparisons with data from Reference 16 indicate that

the underestimation problem is substantially resolved especially for BPF noise from the front rotor though significant underestimation of the magnitude of noise decreases due to angle of attack for BPF noise from the rear rotor is still in evidence. Since the $O(M_y)$ effect has itself proved to be large, it is strongly recommended that research is needed to calculate the acoustic impact of the crossflow more fully.

3.0 Installed Counterrotating Turboprop Noise Analysis

3.1 Introduction

The ultimate test of a theoretical model is its ability to predict events that occur in real life – outside the confines of a controlled experimental setup. During late 1986 and early 1987, a full–scale, highly instrumented proof of concept UDF® engine was flight–tested in the Number 3 engine position (right hand side, aft looking forward) of a Boeing 727–100 aircraft (see Figure 73). As a part of the flight test program, noise data were taken under "community noise" conditions using ground plane microphones, while pressure transducers flush mounted on the fuselage were used to acquire data at cruise. Additional data were taken by NASA personnel using a Learjet "chase" airplane. The flight test program has been described by Harris and Cuthbertson in Reference 4, while community noise aspects and comparisons with model data scaled to full size conditions were addressed by Gliebe in Reference 17.

3.2 High Speed (Cruise) Flight Conditions

The computer program delivered under this Contract was used to predict nearfield noise at flight Mach Nos. of 0.6, 0.728 and 0.8. Pressure transducers were mounted on the fuselage in the locations shown in Figure 74, but it should be noted that, as shown in Figure 75, no tones can be identified in the signals seen by the transducers at the two upstream locations due to the level of the background noise resulting from the fuselage boundary layer.

Comparisons of predicted and measured tone levels are shown in Figures 76 and 77. The UDF® demonstrator engine was configured with eight F7 + eight A7 blades, with the rotors running at approximately the same RPM, consequently the predicted levels in Figures 76 and 77 are comprised of the sum of the contributions from the individual rotors. In making the predictions, the code delivered under this Contract was used to obtain a free field level (with installation effects included) along the fuselage. The rotor–alone components were then adjusted by means of the scattering model delivered under the single rotation portion of this Contract (described in Reference 1) in order to allow for the effects of the curvature of the fuselage and the presence of the boundary layer. This model was derived for isolated rotors and only addresses scattering of the blade passing frequency and its harmonics, however the neglect of rotor/rotor interaction tones is not expected to influence the predicted levels in the region of the planes of rotation of the rotors under cruise conditions. Table 1 summarizes the conditions for which the comparisons were made.

The comparisons presented in Figure 76 were made at Fuselage Station 1303, in the plane of rotation of the forward rotor. It can be seen that, at the three flight Mach numbers shown here, the data and prediction are in very close agreement at the fundamental blade passing frequency tone sum. As the harmonic order increases, discrepancies occur between prediction and measurement, with the predicted levels falling off more rapidly than the data. Figure 77, where the comparisons are made close to the plane of rotation of the aft rotor shows, again, the theoretical prediction falling away more rapidly than the data as the BPF harmonic number increases, but also shows that, in this location, the fundamental tone is overpredicted in all cases.To aid in the interpretation of these results and to assist in the identification of possible causes of discrepancies between prediction and measurement, the data of Figures 75(c) and 75(d) were reanalyzed using a sampling rate equivalent to a 1 Hz bandwidth. Given the differential in rotor speeds (approximately 40 rpm) this was sufficient resolution to enable the identification of individual tones in the spectra. These reanalyzed spectra are shown in Figure 78.
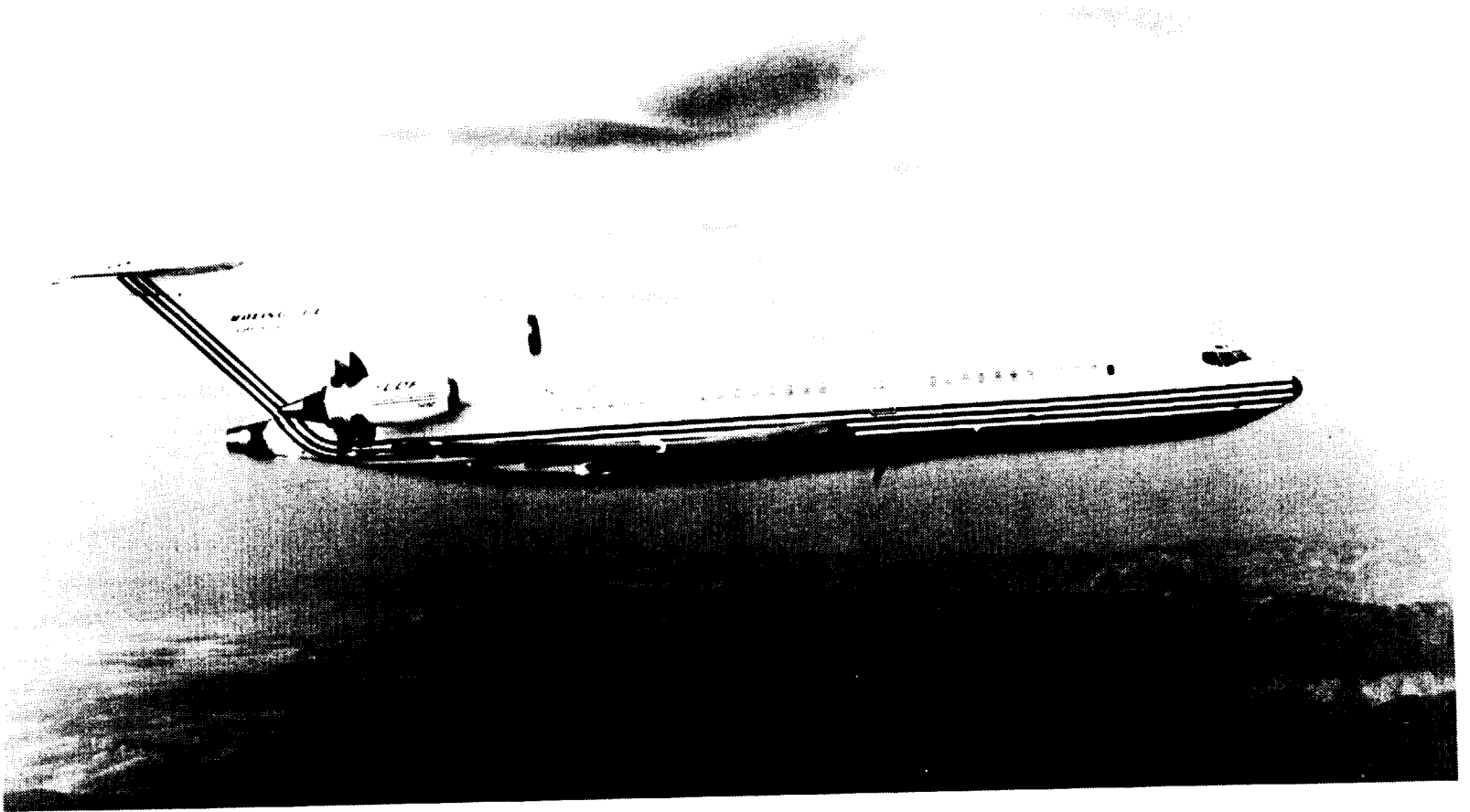
Figure 73. B727/UDF® Engine Demonstrator Airplane.

Engine
Centerline

Sta.
1384

Sta.
1330

Sta.
1303

Sta.
1260

Sta.
1159

Sta.
1091

Fuselage
Centerline

12 ft

17.67 ft

8 inches

● Kulite Locations
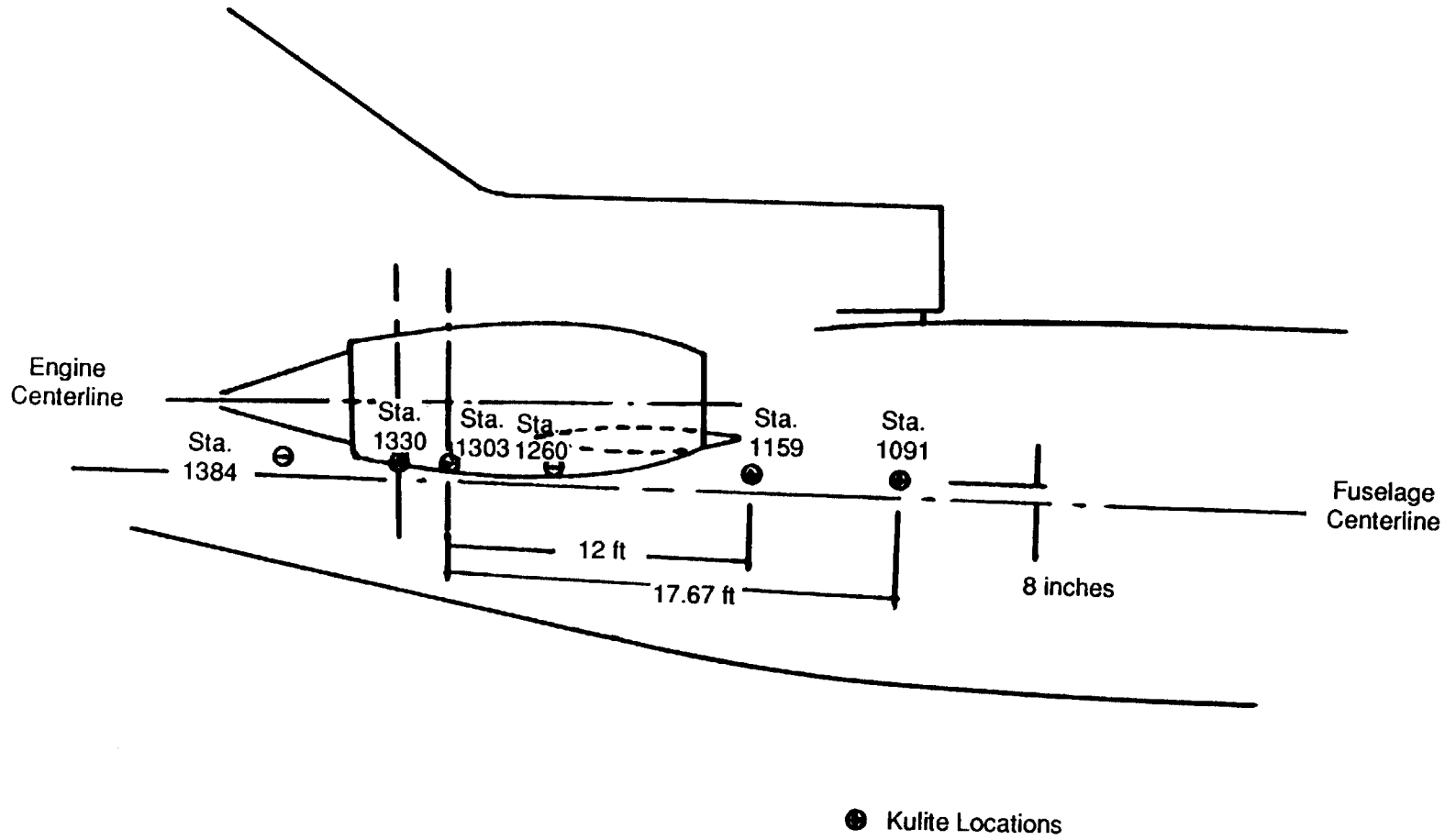
Figure 74. GE Fuselage Transducer Locations.

(a) Station 1091

(b) Station 1159

(c) Station 1303
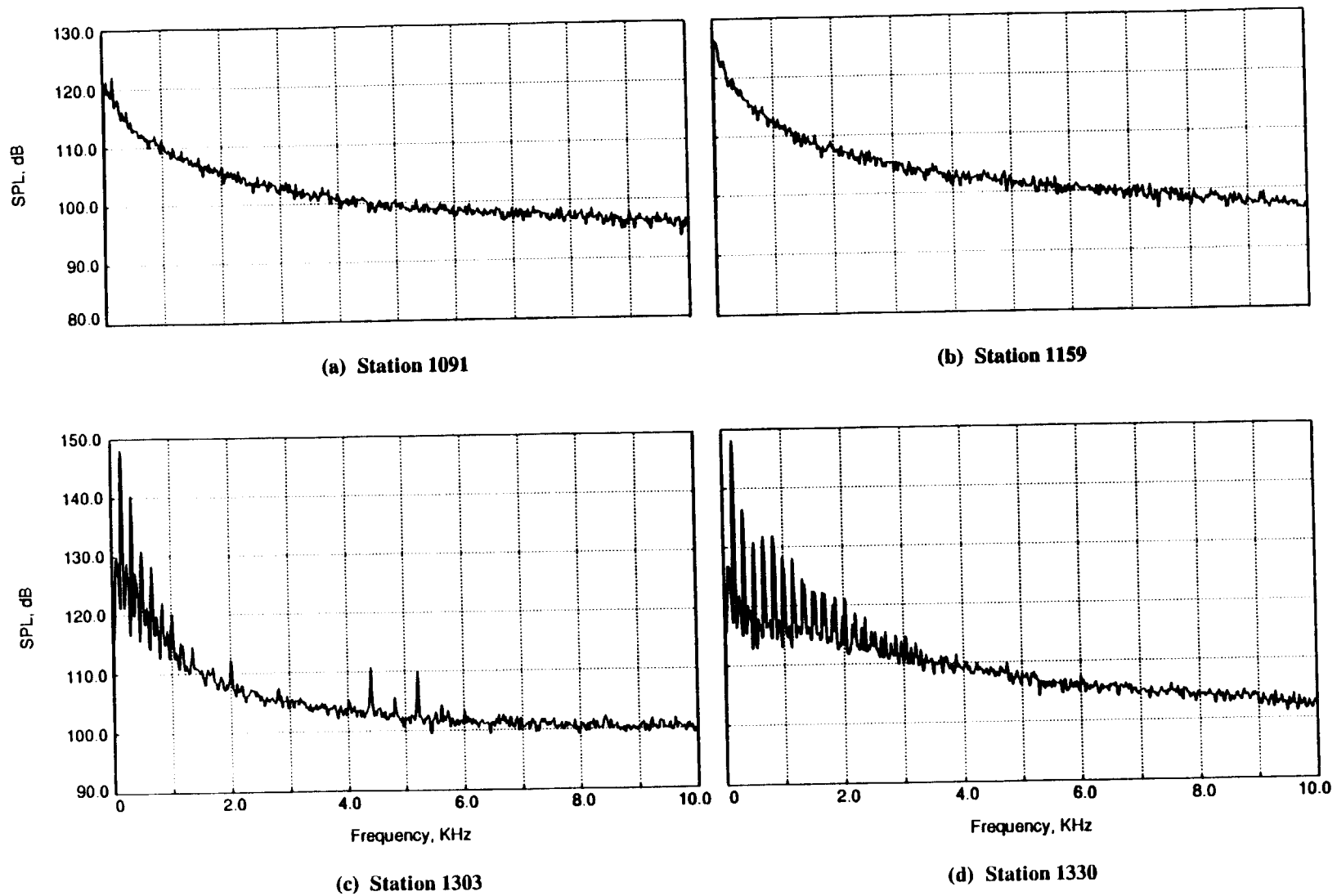
(d) Station 1330

Figure 75. Typical Fuselage Transducer Spectra - 35000 ft, Mach 0.728, EPR = 4.06.
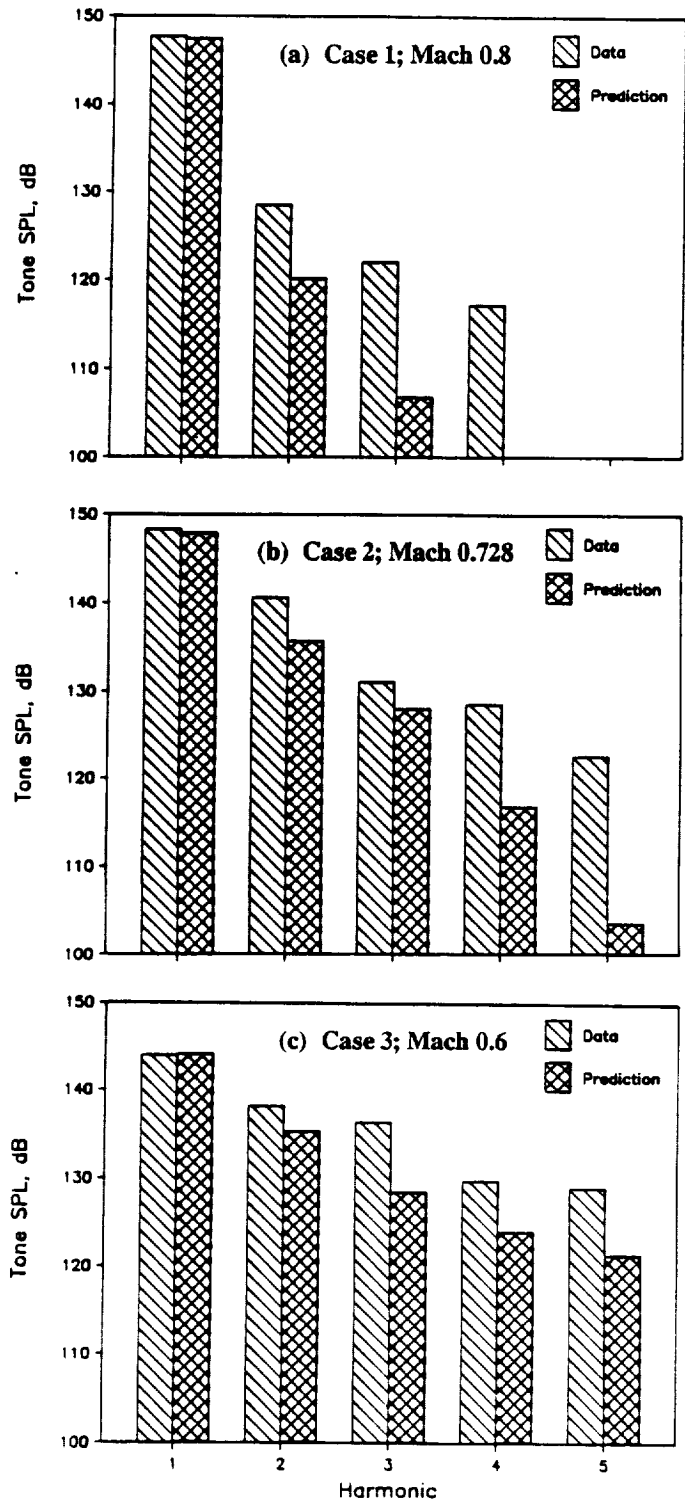
Figure 76. Data/Theory Comparisons at Fuselage Station 1303.

92
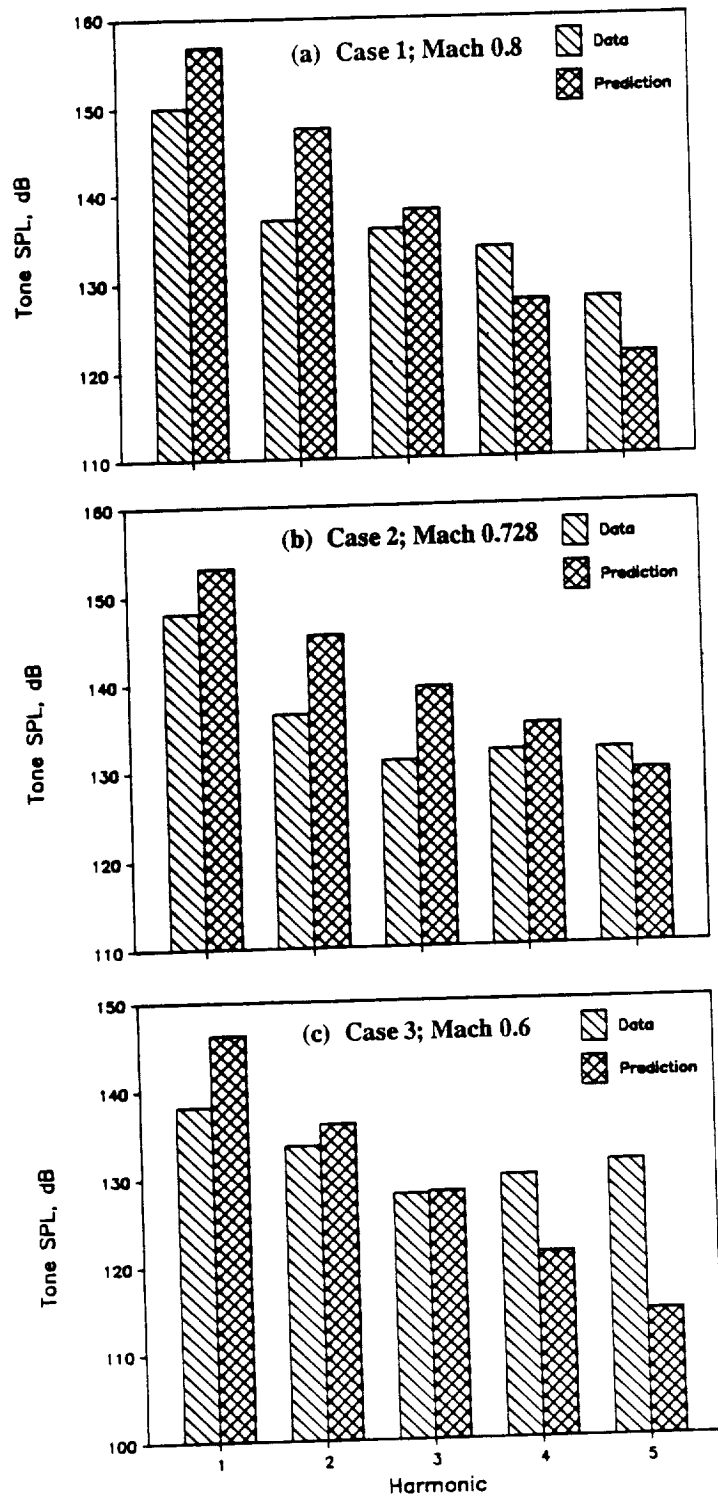
Figure 77. Data/Theory Comparisons at Fuselage Station 1330.

Table 1. B727/UDF® Demonstrator Flight Test Conditions.

Case	Test Condition	Pressure Altitude (ft)	Alttitude AGL (ft)	A/C Mach No	EPR	RPM1	RPM2
1	5.1	35090		0.800	3.97	1280.00	1240.02
2	5.2	35200		0.728	4.07	1270.00	1230.00
3	5.7	35170		0.600	4.07	1250.00	1170.00
4	1.2	4340	1637.12	0.255	3.05	1357.40	1293.10
5	7.2	4371	1669.13	0.251	2.82	1214.90	1211.30
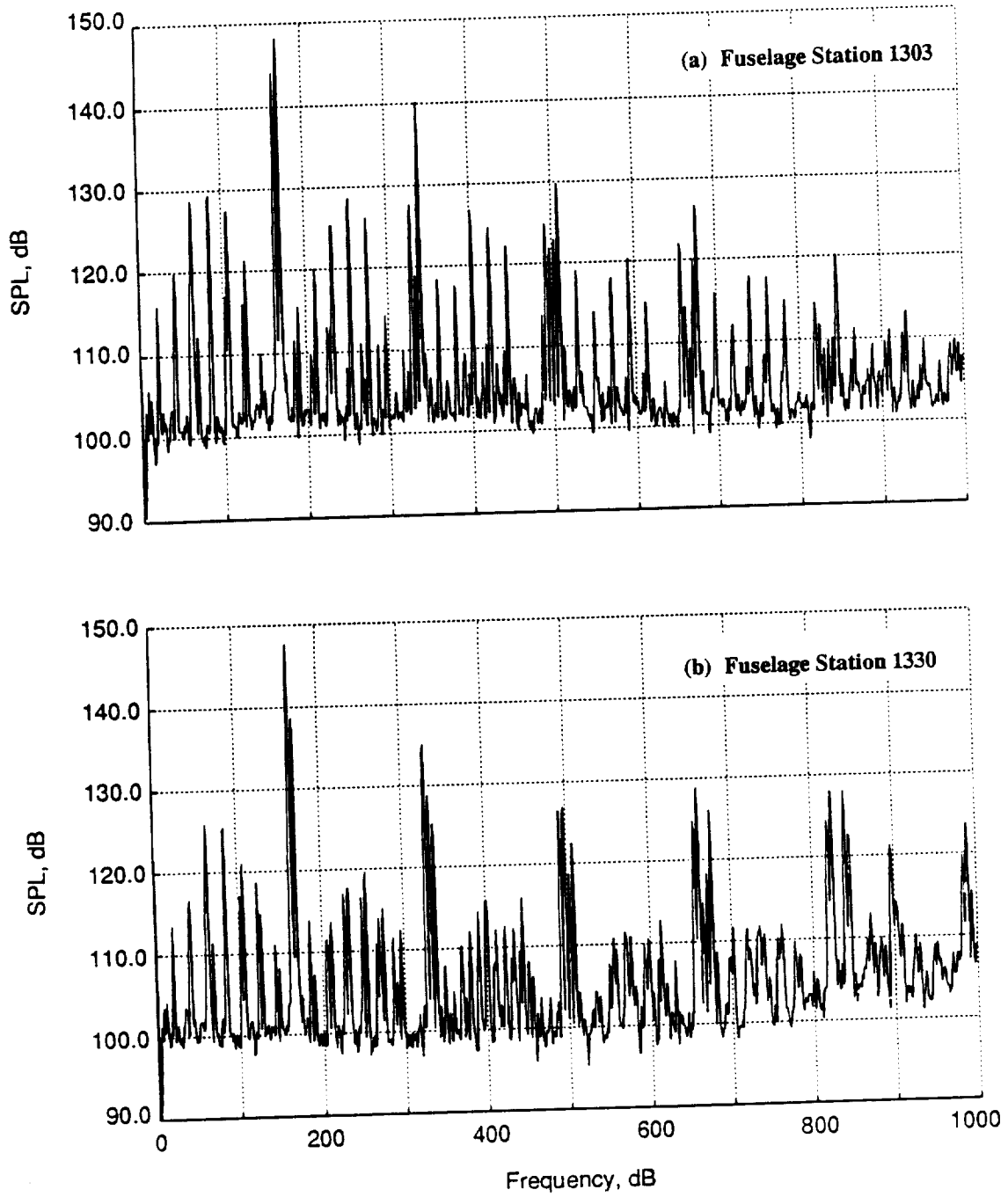
Figure 78. 1 Hz Bandwidth Spectra - Case 2; Mach 0.728.

The predicted levels shown in Figure 76 include the effects of a 1–foot thick boundary layer as calculated by the SRPFS program developed under this Contract (Reference 1). It is not unreasonable to suppose, however, that the presence of the rotors in close proximity to the fuselage would modify the flow over the fuselage in this region, and Figure 79 compares individual tone data with levels predicted with no fuselage scattering effects (free field), and with the predicted effects of 12 inch, 6 inch, and 3 inch thick fuselage boundary layers included. In Reference 1 it was shown that the predicted fuselage (plus boundary layer) scattering effect was a strong function of axial location relative to the plane of rotation, with attenuation occurring upstream and amplification downstream. The fuselage stations at which the data were taken were located (approximately) at the plane of rotation of each rotor; hence, Station 1303 (the forward rotor) is upstream of Rotor 2, and Station 1330 (the aft rotor) is downstream of Rotor 1. The effects of axial location can be seen in the plots of Figure 79 by comparing the "pred" bar with the different "scattered" results. Figures 79(a) and 79(c) compare measurement with prediction at fuselage Station 1303 for forward and aft rotor BPF harmonics respectively. It appears that reasonable agreement between data and prediction for this 0.728 flight Mach No. case is obtained for both rotors if it is assumed that the fuselage boundary layer is 3 inches thick rather than the 12 inches assumed earlier. In the plane of rotation of the aft rotor, Figures 79(b) and 79(d), it appears that, with the exception of the aft rotor BPF tone, the data and prediction are not in very good agreement. For the forward rotor (Figure 79(b)) the "unscattered" level is, by itself, greater than the data, and with the amplification from the scattering analysis the predicted levels increase even more. It is possible that, in addition to the uncertainties introduced by the action of the rotors upon the flow in the region between the blade tips and the fuselage, the fact that the fuselage surface is tapered rather than cylindrical in this region may affect the measured levels. A further cause for discrepancy between measured data and predicted levels may be the boundary layer profile shape assumed by the scattering model. This automatically computes a flat plate ("Blasius") profile for the boundary layer under consideration, which is probably far from the truth in the situation under consideration. No study of the effects of profile shape on the predicted scattering effects has been made. Figure 79 demonstrates that while the computer programs delivered under this Contract predict the noise from model blades measured in a controlled environment with a high degree of accuracy, in the "real airplane" environment there are factors affecting the physics of the problem that are not treated sufficiently rigorously.

One known physical difference between the wind tunnel and flight cases was that the blade coordinates used to generate the predictions reported above were those of the F7A7 model blades, scaled to the appropriate diameter for the full–scale engine. In real life, because of mechanical limitations, the full– scale blades flown on the demonstrator aircraft were not exact replicas of the scaled–up model blades, and it was postulated that some of the differences between Kulite data and prediction discussed above could arise from these differences in hardware. Fortunately, as reported in Reference 18, fuselage Kulite data are not the only source of information on the noise signature of the full–scale UDF® demonstrator engine. Figure 80 (taken from Reference 18) shows the NASA Learjet in formation with the B727 demonstrator aircraft, together with microphone locations at the nose and wingtip of the Learjet. Figure 81 compares data from Reference 18 with predicted levels under conditions that were similar to those of Figure 79. (The authors of Reference 18 question the quality of the nose–mounted microphone data, but they are included here for completeness). It is noticeable that, with the exception of the measurements at 34° observer angle, agreement between prediction and wingtip microphone data is good, thus lending support to the view that discrepancies

96
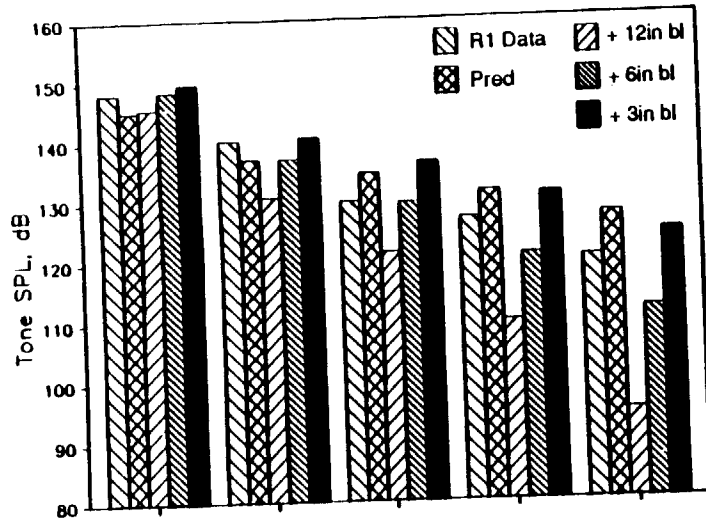
(a) Rotor 1, Fuselage Station 1303
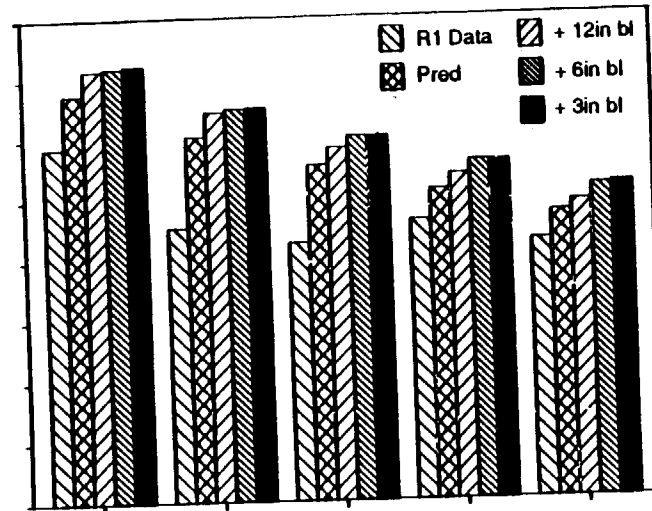
(b) Rotor 1, Fuselage Station 1330
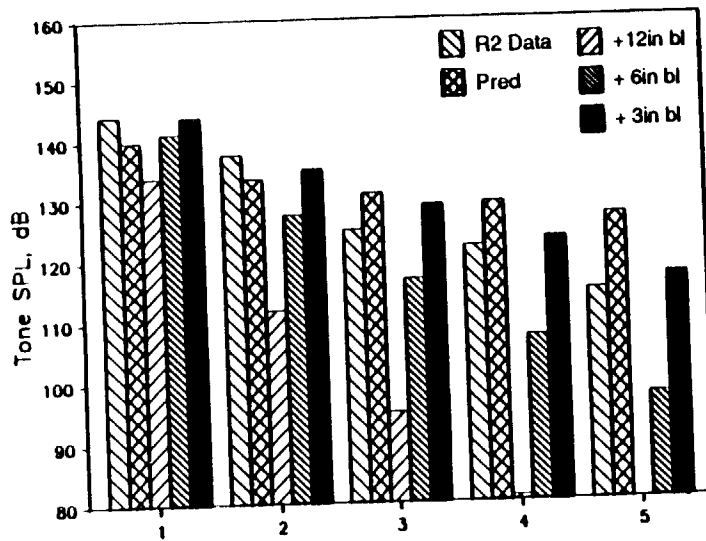
(c) Rotor 2, Fuselage Station 1303
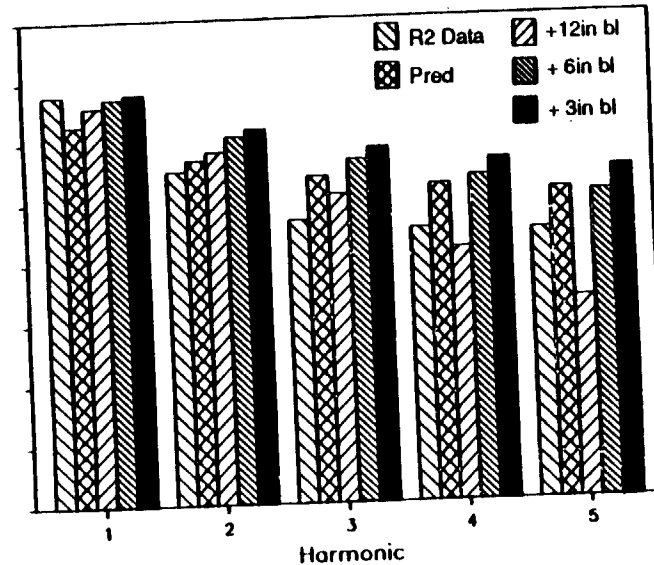
(d) Rotor 2, Fuselage Station 1330

Figure 79. Effect of Assumed Boundary Layer Thickness on Predicted Tone Levels - Case 2; Mach 0.728.
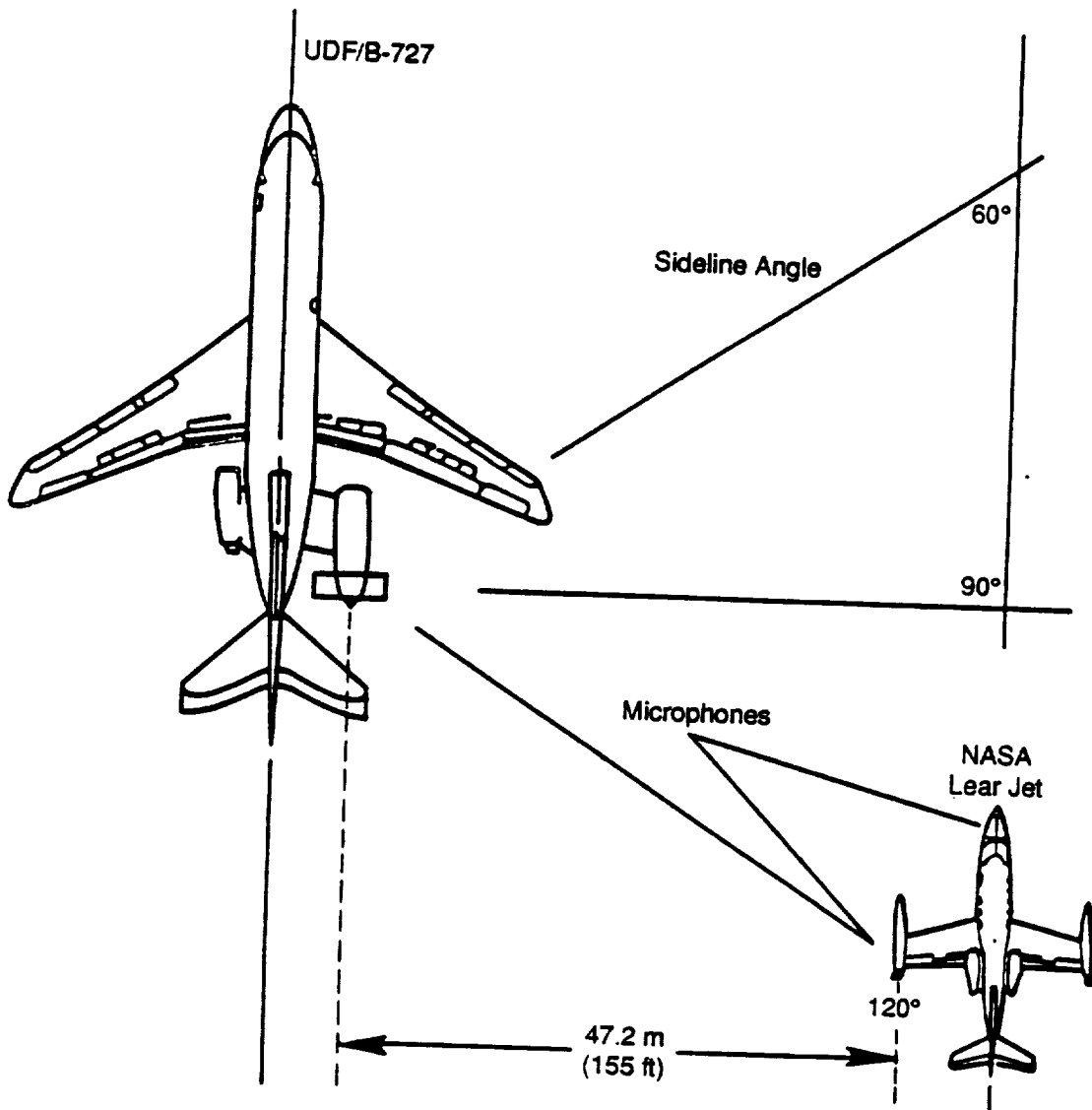
Figure 80. Schematic of NASA Learjet Sideline Positioning for Acoustic Data Acquisition (from Reference 18).
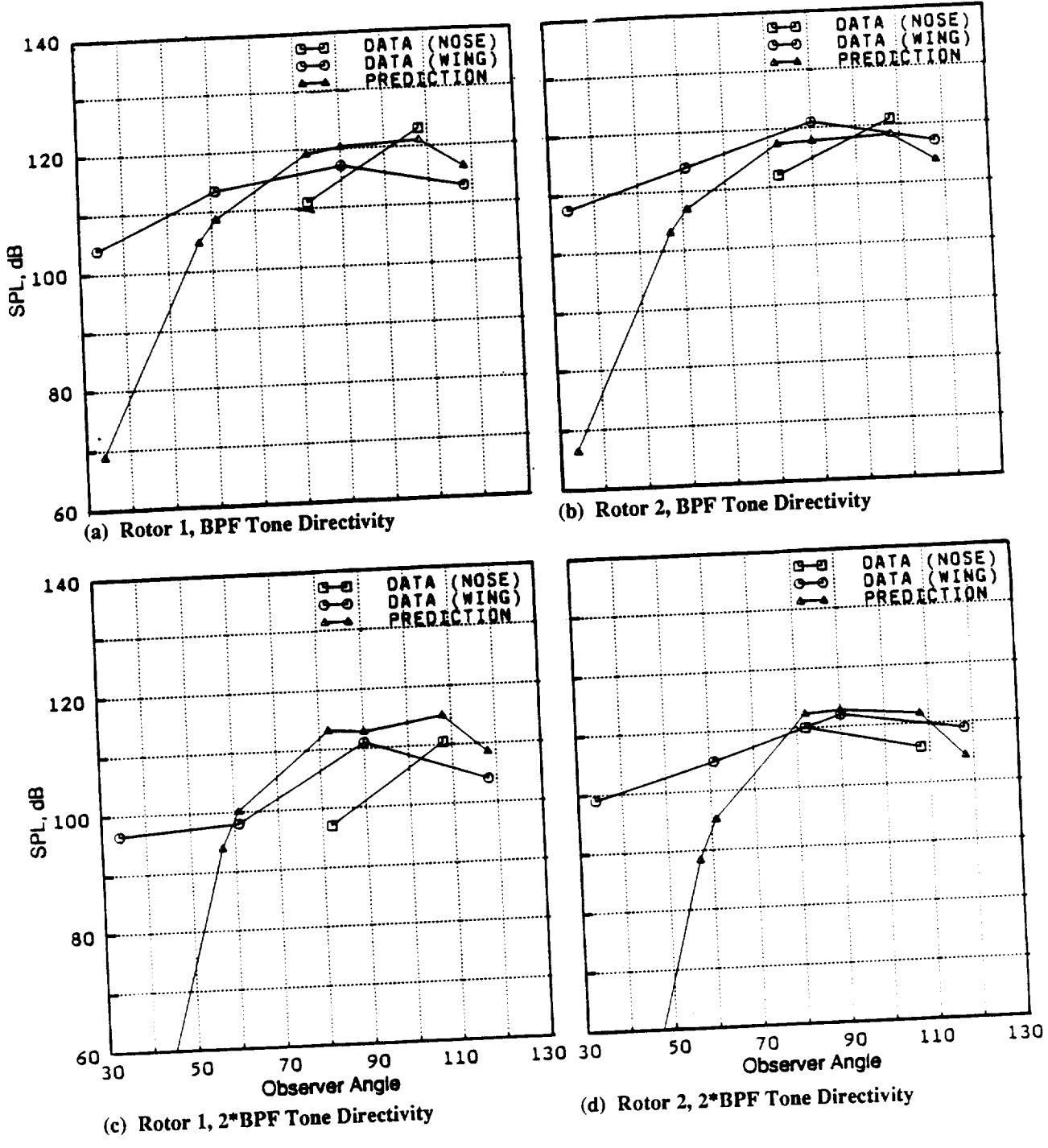
Figure 81. Comparison of Prediction with Data from NASA Learjet Microphones (Reference 18).

99
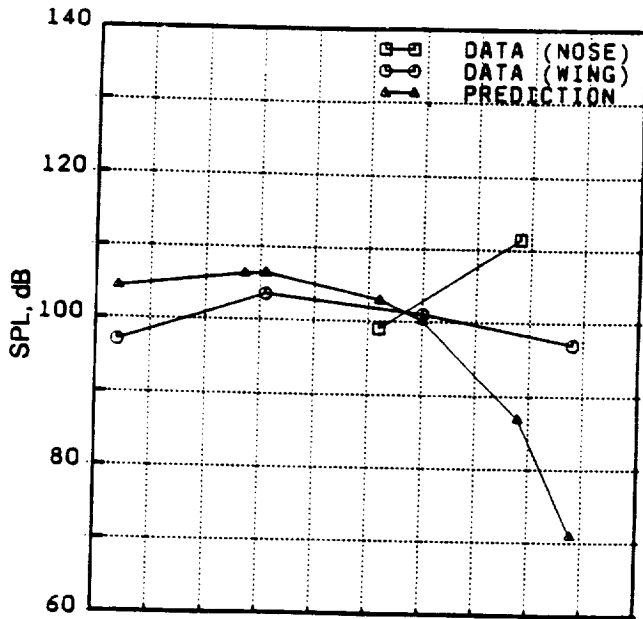
(e) Rotor 1 + Rotor 2 (1st Interaction tone) Directivity
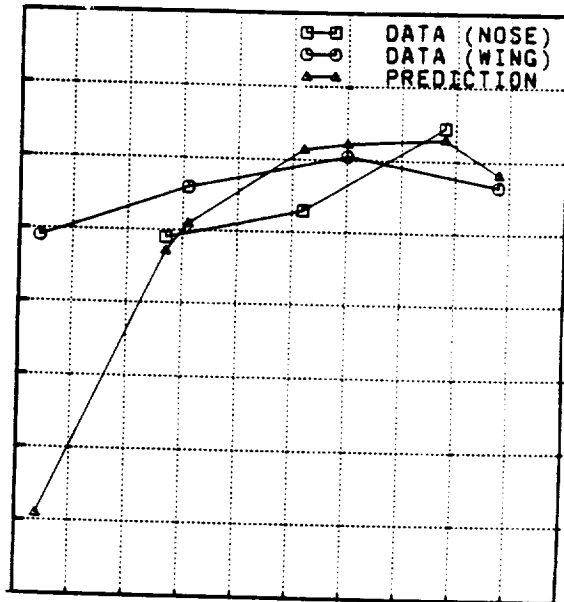
(f) BPF Tone Sum Directivity
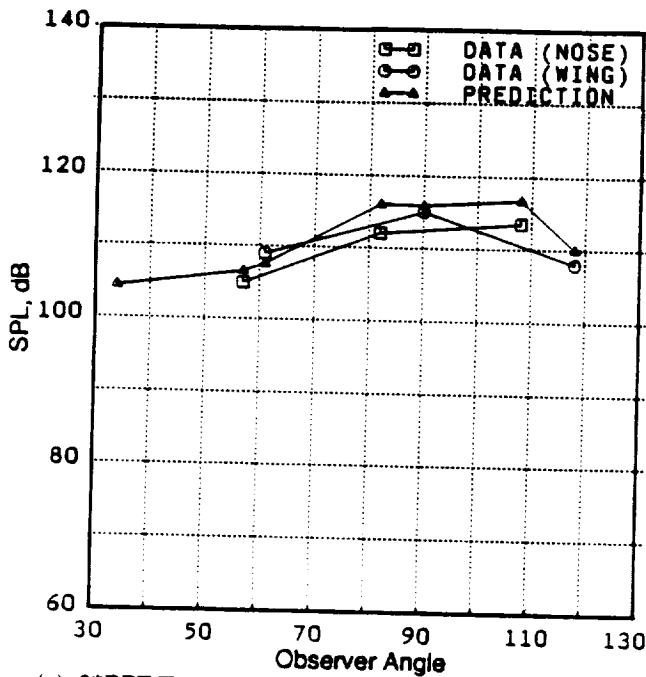
(g) 2*BPF Tone Sum Directivity
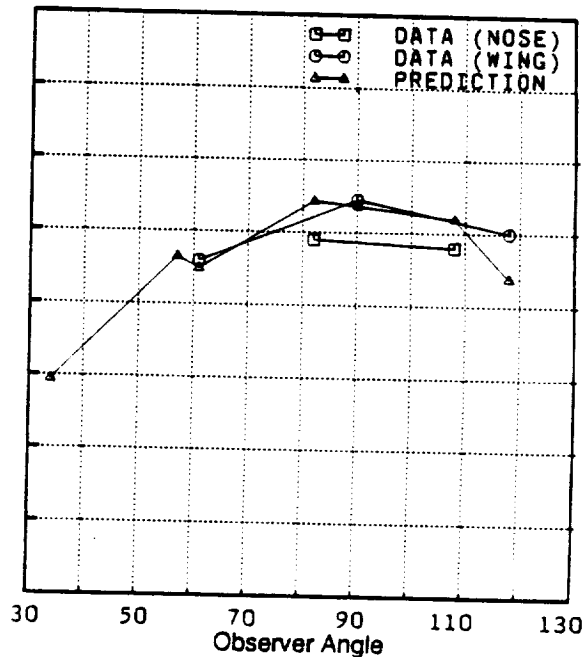
(h) 3*BPF Tone Sum Directivity

Figure 81. Comparison of Prediction with Data from NASA Learjet Microphones (Reference 18) (Concluded).

in the fuselage data/theory comparisons are a function of the fuselage scattering model. It is not known, however, whether the model itself is in error, or if insufficient knowledge with regard to the input required is giving rise to erroneous results. In fact, given the agreement in directives between the tone data measured by the Learjet microphone and the prediction, it has been suggested that the apparent change in source directivity proposed by Hanson and Magliozzi (Reference 19) is in evidence in the fuselage results. Why this should appear under these conditions, but not in the wind tunnel results of Section 2.1.3.1 is, at present, unclear.

Comparisons of results predicted by the code delivered under this Contract with data taken under cruise conditions for a "real" aeroplane/engine combination have demonstrated that differences between prediction and measurement can be related to the fuselage scattering model.

3.3 Low Speed (Community Noise) Flight Conditions

In addition to the high speed flight test program described above, the B727/UDF® demonstrator aircraft was flown under simulated "community noise" conditions in order to investigate the procedures used to scale model data to full size (Reference 17) and to validate the prediction model. The data were taken with a ground plane microphone and are compared with prediction in Figures 82 and 83 at 100% and 80% thrust conditions (cases 4 and 5 of Table 1) respectively. Two predictions are shown in each figure; the first, "uninstalled", represents the output from the isolated counterrotation model; the second, "installed", includes installation effects, but on the BPF harmonics only. It can be seen (Figures 82(a) and 83(a)) that inclusion of the installation effects improves the comparison for the fundamental BPF tones, however, (Figures 82(b), 82(c), 83(b) and 83(c)) for the higher harmonics of BPF the levels are dominated by the unsteady rotor/rotor interaction tones, with the individual rotor BPF harmonics (even with installation effects included) contributing a negligible portion of the tone energy.

Figures 82(a) and 83(a) demonstrate that, even with the installation effects included, the level in the forward arc is underpredicted. In spite of this discrepancy, it is felt that, overall, for these two flight conditions, the agreement between data and prediction is extremely good.
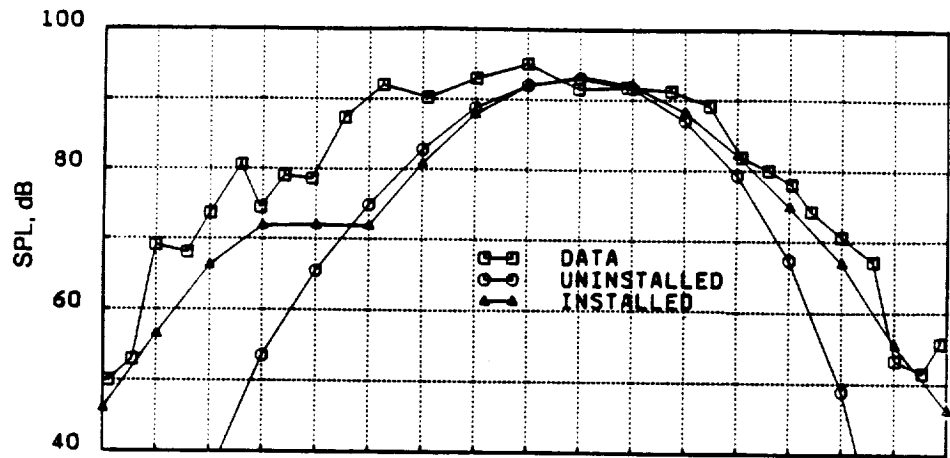
(a) BPF Tone Sum Directivity
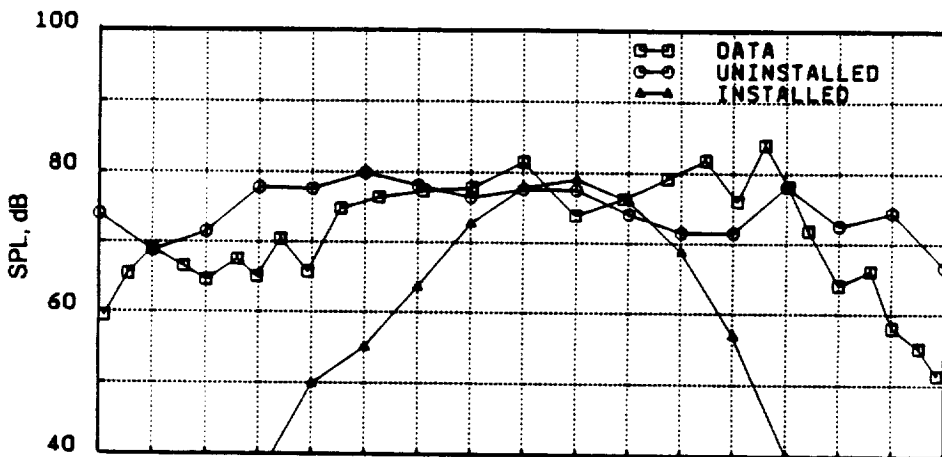
(b) 2*BPF Tone Sum Directivity
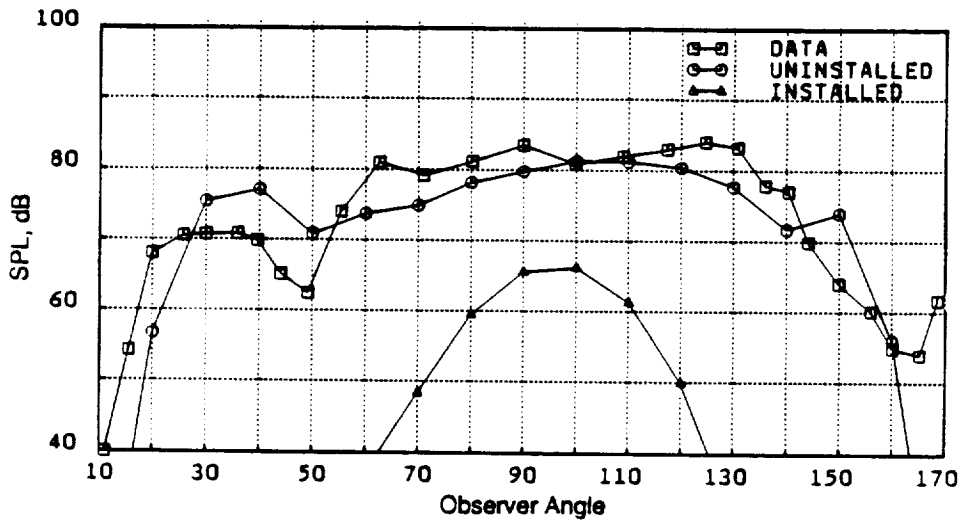
(c) 3*BPF Tone Sum Directivity

Figure 82. Comparison of Prediction with Fly-Over Data from Ground - Plane Microphone: 100% Thrust (Case 4).

(a) BPF Tone Sum Directivity

(b) 2*BPF Tone Sum Directivity

(c) 3*BPF Tone Sum Directivity
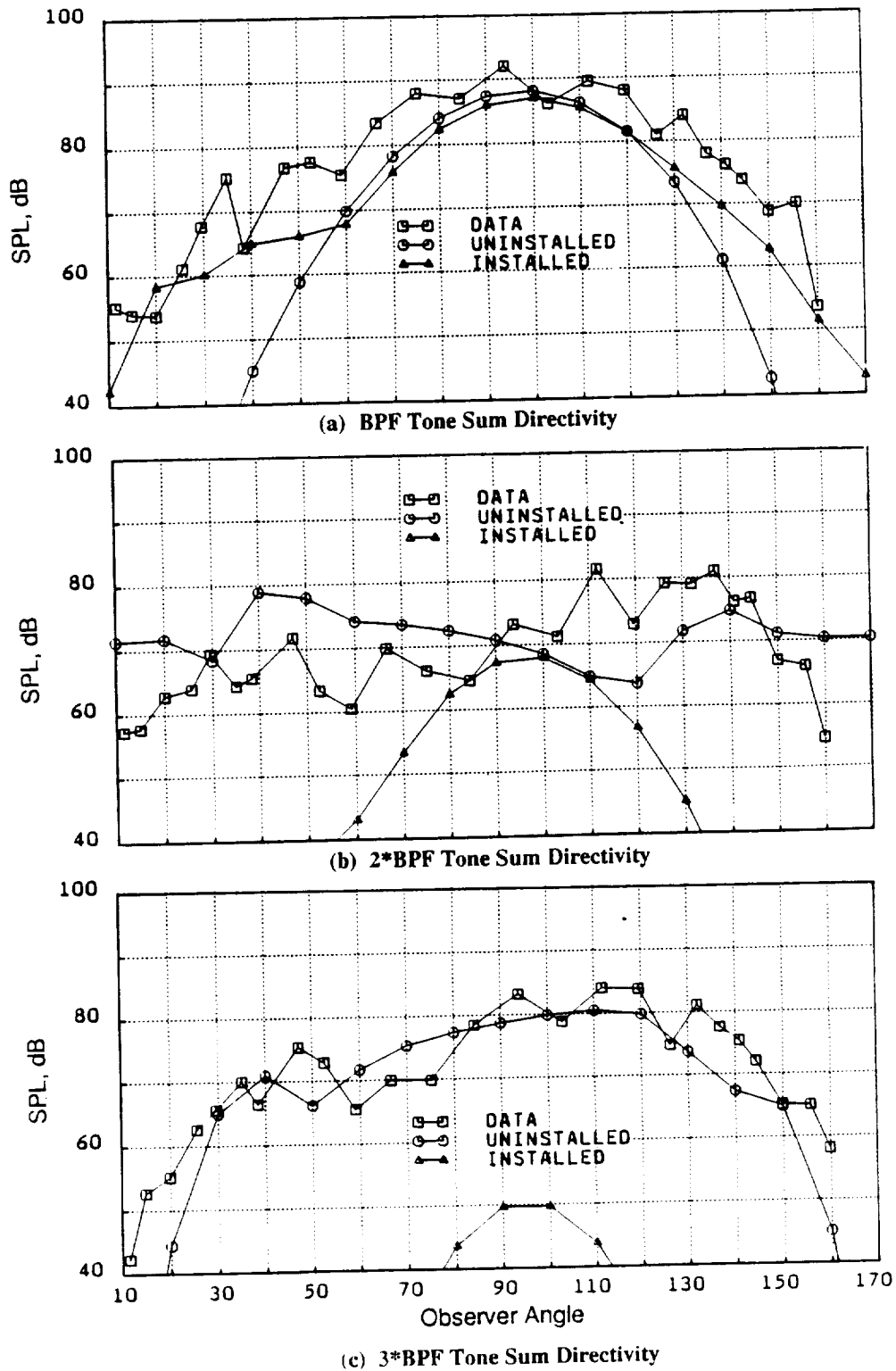
Figure 83. Comparison of Prediction with Fly-Over Data from Ground - Plane Microphone - 80% Thrust.
(Case 5).

4.0 Conclusions

The isolated counterrotating propfan noise prediction program developed at GE Aircraft Engines under internal funding has been compared with data from scale model tests under both low and high simulated flight Mach Number conditions. Comparisons have been made for a total of five blade design combinations and the predicted results show good agreement with the measured data under both low and high speed conditions.

The single rotation installation effects model developed under this Contract has been extended to counterrotation, and the effect of a mounting pylon, upstream of the forward rotor, has been included in the analysis.

A nontraditional mechanism concerning the acoustic radiation from a propeller at angle of attack has been investigated. Predictions made using this approach have been compared with scale model data and show results that are in much closer agreement with the measurements over a range of operating conditions than those obtained via traditional fluctuating force methods.

The isolated rotors and installation effects models have been combined into a single prediction program, results of which have been compared with data from the flight test of the B727/UDF® engine demonstrator aircraft. It has been shown that uncertainties concerning the nature of the flow field in the region between the blade tips and the aircraft fuselage lead to difficulties in the successful prediction of data taken with Kulites mounted in the fuselage, but that data taken with the NASA Learjet under cruise conditions and with ground plane microphones under community noise conditions compare well with predicted levels.

The satisfactory comparisons between prediction and measured data for the demonstrator airplane, together with the identification of a nontraditional radiation mechanism for propellers at angle of attack constitute the major achievements of this Contract.

REFERENCES

1. Whitfield, C.E., Gliebe P.R., Mani, R. and Mungur, P.,"High Speed Turboprop Aeroacoustic Study (Single Rotation) Volume 1: Model Development," NASA CR-182257, May 1989.

2. Hoff, G.E., et.al., "Experimental Performance and Acoustic Investigation of Modern Counter Rotation Concepts," GE Aircraft Engines TM87-528 (1988) also NASA CR-185158, January 1990.

3. Mani, R. "The Radiation of Sound from a Propeller at Angle of Attack," NASA CR-4264, January 1990.

4. Harris, R.W. and Cuthbertson, R.D., "UDF®/727 Flight Test Program," AIAA paper AIAA-87-1733, 1987.

5. Hanson, D.B. "Noise of Counter Rotation Propellers", AIAA Paper AIAA-84-2305, October 1984.

6. Majjigi, R.K. and Gliebe, P.R.,"Development of a Rotor Wake/ Vortex Model, Volume 1," NASA CR-174849, June 1984.

7. Majjigi, R.K., Uenishi, K. and Gliebe, P.R., "An Investigation of Counterrotating Tip Vortex Interaction," NASA CR-185135, October 1989.

8. Dittmar, J.H., "Comparison of Propeller Cruise Noise Data Taken in the NASA Lewis 8-by 6-foot Wind Tunnel with Other Tunnel and Flight Data," NASA TM 101976, also AIAA paper AIAA-89-1059, April 1989

9. Woodward, R.P. and Gordon, E.B., "Noise of a Model Counterrotation Propeller with Reduced Aft Rotor Diameter at Simulated Takeoff/Approach Conditions (F7/A3)," NASA TM 100254, also AIAA paper AIAA-88-0263, January 1988.

10. Dittmar, J.H. and Stang, D.B., "Noise Reduction for Model Counterrotation Propeller at Cruise by Reducing Aft. Propeller Diameter," NASA TM-88936, 1987

11. Janardan, B.A. and Gliebe, P.R., "Acoustic Characteristics of Counterrotating Fans from Model Scale Tests," AIAA paper AIAA-89-11, 1989.

12. Ahuja, K.K., Tester, B.J. and Tanna, H.K., "The Freejet as a Simulator of Forward Velocity Effects on Jet Noise," NASA CR-2056, October 1978.

13. Kemp, N.H. and Sears, W.R., "The Unsteady Forces Due to Viscous Wakes in Turbomachines," J. Aeronautical Sciences 22 (7), 1955, pp. 478-483.

14. Glauert, H., The Elements of Aerofoil and Airscrew Theory (Second Edition), C.U.P, 1959.

15. Block, P.J.W., "The Effects of Installation on Single and Counter Rotation Noise," AIAA paper 84-2263, 1984.

16. Woodward, R.P., "Noise of a Model High Speed Counterrotation Propeller at Simulated Takeoff/Approach Conditions (F7/A7)," AIAA 87-2657, 1987.

17. Gliebe, P.R., "Flight Test vs Model Test UDF® Engine Noise," Proceedings of Royal Aeronautical Society Conference on "Advanced Propellers and their Installation on Aircraft," September 1988.

18. Woodward, R.P., Loeffler, I.J., and Dittmar, J.H., "Measured Far–Field Flight Noise of a Counterrotation Turboprop at Cruise Conditions," NASA TM 101383, January 1989.

19. Hanson, D.B. and Magliozzi, B. "Propagation of Propeller Tone Noise Through a Fuselage Boundary Layer," AIAA Paper AIAA–84–0248, January 1984.

1. Report No. NASA CR–185241	2. Government Accession No.	3. Recipient's Catalog No.
4. Title and Subtitle High Speed Turboprop Aeroacoustic Study (Counterrotation) Volume I – Model Development		5. Report Date July 1990
		6. Performing Organization Code
7. Author(s) C.E. Whitfield, R. Mani, and P.R. Gliebe		8. Performing Organization Report No.
		10. Work Unit No. 535-05-01
9. Performing Organization Name and Address GE Aircraft Engines 1 Neumann Way P.O. Box 156301 Cincinnati, Ohio 45215-3191		11. Contract or Grant No. NAS3–23721
		13. Type of Report and Period Covered Contractor Report (Final)
12. Sponsoring Agency Name and Address National Aeronautics and Space Administration Lewis Research Center Cleveland, Ohio 44135-3191		14. Sponsoring Agency Code

15. Supplementary Notes

Project Manager: Dr. James H. Dittmar, Propulsion Systems Division
NASA Lewis Research Center

16. Abstract

The isolated counterrotating high speed turboprop noise prediction program developed and funded by GE Aircraft Engines has been compared with model data taken in the GE Aircraft Engines Cell 41 anechoic facility, the Boeing Transonic Wind Tunnel, and in NASA Lewis Research Center's 8x6 and 9x15 wind tunnels. The predictions show good agreement with measured data under both low and high speed simulated flight conditions.

The installation effect model developed for single-rotation, high speed turboprops has been extended to include counterrotation. The additional effect of mounting a pylon upstream of the forward rotor has been included in the flow field modeling.

A nontraditional mechanism concerning the acoustic radiation from a propeller at angle of attack has been investigated. Predictions made using this approach show results that are in much closer agreement with measurement over a range of operating conditions than those obtained via traditional fluctuating force methods.

The isolated rotors and installation effects models have been combined into a single prediction program, results of which have been compared with data taken during the flight test of the B727/UDF®* engine demonstrator aircraft.

It is the satisfactory comparisons between prediction and measured data for the demonstrator airplane, together with the identification of a nontraditional radiation mechanism for propellers at angle of attack that constitute the major achievements of this Contract.

*UDF® is a registered trademark of the General Electric Company, U.S.A.

17. Key Words (Suggested by Author(s)) Counterrotation propeller noise, steady loading and thickness noise, installation effects on propeller noise, fuselage effects on propeller noise, aircraft control integration	18. Distribution Statement Publicly Available		
19. Security Classif. (of this report) Unclassified	20. Security Classif. (of this page) Unclassified	21. No. of Pages	22. Price